

**TRANSIENT RHEOLOGY OF STIMULI RESPONSIVE
HYDROGELS: INTEGRATING MICRORHEOLOGY AND
MICROFLUIDICS**

A Dissertation
Presented to
The Academic Faculty

by

Jun Sato

In Partial Fulfillment
of the Requirements for the Degree
Doctor of Philosophy in the
School of Chemical & Biomolecular Engineering

Georgia Institute of Technology
December 2006

COPYRIGHT © 2006 BY JUN SATO

**TRANSIENT RHEOLOGY OF STIMULI RESPONSIVE
HYDROGELS: INTEGRATING MICRORHEOLOGY AND
MICROFLUIDICS**

Approved by:

Dr. Victor Breedveld, Advisor
School of Chemical & Biomolecular
Engineering
Georgia Institute of Technology

Dr. J. Carson Meredith
School of Chemical & Biomolecular
Engineering
Georgia Institute of Technology

Dr. William J. Koros
School of Chemical & Biomolecular
Engineering
Georgia Institute of Technology

Dr. L. Andrew Lyon
School of Chemistry & Biochemistry
Georgia Institute of Technology

Dr. Andreas S. Bommarius
School of Chemical & Biomolecular
Engineering
Georgia Institute of Technology

Date Approved: Sep 25, 2006

dedicated to the memory of

my father

MASARU SATO

(April 22, 1940-March 24, 2005)

and my grand father

YOSHIO OGINO

(January 5, 1917-Oct 30, 2005)

ACKNOWLEDGEMENTS

I would like to thank all the people who have contributed to this work. First, I would like to express my gratitude to my advisor, Dr. Victor Breedveld, for his support, guidance, and encouragement to achieve my goal over the past four years. I learned from his vision, method and excitement. I feel lucky to have had the freedom to pursue topics that excited me, and it was a privilege to be his first graduate student.

I wish to thank my committee members, Dr. William J. Koros, Dr. Andreas S. Bommarius, Dr. J. Carson Meredith, and Dr. L. Andrew Lyon for their valuable advice. I would also like to thank the Complex Fluids Research Group members; Dr. Raymond Tu, Enrique Michel-Sanchez, Ryan Slopek, Jae Kyu Cho, Balamurali Balu, and undergraduate research assistants; Haris McKinley, Luke Byerly, Byron Best, Tori Balcer, Katie Ussery, Tracie Owens, and Ryan Collins for creating an enjoyable environment in everyday laboratory life.

In pursuing my projects, I received valuable assistance from a number of people on/off campus. I am also grateful to Dr. Anthanasios Nenes, Dr. Clifford L. Henderson and Travis Anderson for their help with the design and fabrication of the dialysis cell. I would like to thank Dr. Eric Weeks and Dr. Denis Semwogerere at Emory University for their assistance with confocal microscopy. I am indebted to Dr. Timothy Deming and Dr. Andrew Nowak at UCLA for providing us samples and valuable suggestions.

I would also like to acknowledge Prof. Michael Graham at the University of Wisconsin, Madison, for his encouragement whenever we meet, and Prof. Edwin Lightfoot for cheering me up with his heartfelt letter when I had a hard time.

I cannot imagine my life without my friends I made in Atlanta. I would like to thank all my friends for providing good times and bountiful experiences that made my life in Atlanta unforgettable. I would also like to thank Toshinao, Amy, Justin and David for helping me get settled. Special thanks to go to Mike, Nancy, Anshul, Neil, Gracy, Jason, Ray, Enrique, Eduardo, Charlene, Reginald, Luz, and Sigi for being good friends and reminding me of life beyond research. I also would like to acknowledge former graduate students, Krishna Marla and Joe Sormana, for their precious advice.

Finally, I am deeply grateful to my family for their understanding, support and encouragement. Most importantly, it is impossible to express in words how much I owe to my father and grandfather, who passed away just before this work was completed. They showed me their vision and philosophy through their entire lives. They have been models for my life, and they will be forever.

TABLE OF CONTENTS

	Page
ACKNOWLEDGEMENTS	IV
LIST OF TABLES	X
LIST OF FIGURES	XI
LIST OF SYMBOLS AND ABBREVIATIONS	XIX
SUMMARY	XX
 CHAPTER 1	
INTRODUCTION	1
1.1 BACKGROUND AND MOTIVATION	1
1.2 MICRORHEOLOGY	5
1.3 OBJECTIVES AND OUTLINE	10
 CHAPTER 2	
A NEW DEVICE FOR MEASURING TRANSIENT RHEOLOGY OF SOLVENT-RESPONSIVE COMPLEX FLUIDS	13
2.1 INTRODUCTION	13
2.2 DIALYSIS CELL	15
2.2.1 GENERAL IDEA	15
2.2.2 NUMERICAL CALCULATION	16
2.2.3 MICROFABRICATION	19
2.2.4 FLOW SYSTEM	21
2.3 VIDEO MICROSCOPY AND MICRORHEOLOGY	22
2.4 EXPERIMENTS	26
2.4.1 TRANSPORT VALIDATION WITH FLUORESCCEIN SOLUTION	26

2.4.2	SODIUM ALGINATE GELATION	29
2.4.3	NAPSS POLYELECTROLYTE VISCOSITY	38
2.5	CONCLUSIONS	42
CHAPTER 3		
TRANSIENT PARTICLE TRACKING MICRORHEOLOGY OF HETEROGENEOUS SAMPLES		43
3.1	INTRODUCTION	43
3.2	METHODS AND MATERIALS	46
3.2.1	MICRORHEOLOGY	46
3.2.2	EQUIPMENT	48
3.2.3	SAMPLE PREPARATION	48
3.3	RESULTS AND DISCUSSION	49
3.3.1	HOMOGENEOUS MEDIA	49
3.3.2	HETEROGENEOUS MEDIA	51
3.3.3	TRANSIENT HETEROGENEITY	60
3.3.4	TRANSIENT COMPLEX MODULUS	63
3.4	CONCLUSIONS	67
CHAPTER 4		
MICROSTRUCTURAL EVOLUTION OF SALT-RESPONSIVE HYDROGELS UNDERGOING DIFFUSIVE SOLVENT EXCHANGE		69
4.1	INTRODUCTION	69
4.2	METHODS AND MATERIALS	71
4.2.1	EQUIPMENT AND MICRORHEOLOGY	71
4.2.2	SAMPLE PREPARATION	72
4.2.3	LASER SCANNING CONFOCAL MICROSCOPY	72
4.3	RESULTS AND DISCUSSION	78

4.4 CONCLUSIONS	84
CHAPTER 5	
SYSTEMATIC INVESTIGATION OF MORPHOLOGY AND RHEOLOGY OF BLOCK COPOLYPEPTIDE HYDROGELS	85
5.1 INTRODUCTION	85
5.2 METHODS AND MATERIALS	86
5.2.1 SAMPLE PREPARATION	86
5.2.2 DIALYSIS CELL AND SOLVENT MANIPULATION	87
5.2.3 LSCM	88
5.2.4 TRANSIENT MICRORHEOLOGY	88
5.3 RESULTS	90
5.3.1 THE EFFECT OF GEL CONCENTRATION	91
5.3.1.1. K ₁₆₀ L ₄₀	91
5.3.1.2. K ₁₈₀ L ₂₀	92
5.3.2 THE EFFECT OF MOLECULAR STRUCTURE	96
5.3.3 HETEROGENEITY	99
5.3.4 SPATIAL VARIATIONS ACROSS THE DIALYSIS CELL	102
5.4 DISCUSSION	106
5.4.1 THE EFFECT OF TRACER SIZE	106
5.4.2 REPETITIVE DIALYSIS AND RECOVERY AFTER BREAK-DOWN	110
5.4.3 LAG TIME ANALYSIS	112
5.5 CONCLUSIONS	114
CHAPTER 6	
CONCLUDING REMARKS	115
6.1 CONCLUSIONS	115

6.1.1	DIALYSIS CELL AND TRANSIENT $PT_{\mu R}$	116
6.1.2	APPLICATIONS OF DIALSYS CELL AND TRANSIENT $PT_{\mu R}$	117
6.2	RECOMMENDATIONS	118
6.2.1.	GEL FORMATION AND BREAK-UP KINETICS OF SODIUM ALGINATE	118
6.2.2.	HIGH THROUGHPUT SCREENING	123
6.2.2.1.	Current limitations	123
6.2.2.2.	Concept	125
6.2.3.	TRANSPARENT DIALYSIS CELL	128
 APPENDIX A		
IDL CODE FOR TRANSIENT ANALYSIS OF HETEROGENEOUS MEDIA		130
A.1	TRANSIENT HETEROGENEITY	130
A.2	NON-GAUSSIAN PARAMETER	132
 REFERENCES		146
LIST OF PUBLICATIONS		161
VITA		163

LIST OF TABLES

	Page
Table 1.1: Characteristic diffusion time for Na ⁺ ions in DI water through samples of different thicknesses based on simple one-dimensional diffusion ($D=1.33\times 10^{-9}\text{m}^2\cdot\text{s}^{-1}$).	4
Table 2.1: Composition of the reservoir flow during validation experiments with fluorescein solutions. Fluorescein concentrations were varied.	28
Table 2.2: Composition of the reservoir flow during sodium alginate experiment. CaCl ₂ concentration was varied.	31
Table 2.3: Composition of the reservoir flow during NaPSS experiments.	39

LIST OF FIGURES

	Page
Figure 1.1:	Mean-squared displacement as a function of lag time for tracer particle in various complex fluids. For viscous samples (\blacktriangle), the slope in the double logarithmic plot is 1, while for highly elastic gels (\bullet) it equals 0 (plateau); viscoelastic samples (\blacktriangledown) exhibit slope values between 0 and 1. 7
Figure 2.1:	Schematic representation of the dialysis cell. 16
Figure 2.2:	(a) Three-dimensional geometry of the dialysis cell (only one half shown for clarity): $H_r=200\text{ }\mu\text{m}$, $H_m=60\text{ }\mu\text{m}$, $H_s=120\text{ }\mu\text{m}$, $L_r=1\text{ cm}$, $L_s=5\text{ mm}$, $W_r=3\text{ mm}$, $W_m=1.5\text{ mm}$. A sketch of the velocity profiles in the reservoir is also included. (b) Time-dependent concentration profiles of Ca^{2+} ions, calculated with a Finite Volume Method at: reservoir centerline (\times), halfway between reservoir centerline and bottom (\square), reservoir bottom (\diamond), membrane center (\triangle), sample top (∇), sample center (\triangleright), and sample bottom (\triangleleft) (see inset). Pressure gradient is $-3810\text{ Pa}\cdot\text{m}^{-1}$ and viscosity is 1 mPa . $D_0=7.92\cdot 10^{-10}\text{ m}^2\cdot\text{s}^{-1}$, $G=0.15$, $H=0.88$, and $x_{\text{test}}=5000\text{ }\mu\text{m}$. 17
Figure 2.3:	Flow system and measuring system. 22
Figure 2.4:	Diagram of microrheology system. 24
Figure 2.5:	(a) Transient brightness for two different fluorescein concentrations, (b) Normalized concentration curves and results of numerical calculations with $D_0=5.2\cdot 10^{-10}\text{ m}^2\cdot\text{s}^{-1}$, $G=0.15$, and $H=0.82$. Calibration curve for fluorescein is depicted in the inset. 28
Figure 2.6:	MSD vs. τ . (\circ) before gel formation and (\bullet) after gel formation for 0.25 wt% alginate solution in 150 mM NaCl and 0.111 wt% CaCl_2 . 31
Figure 2.7:	(a) The transient MSD: $\tau=(+)$ 33ms, (\bullet)67ms, and (\circ)100ms, solvents: (\square)NaCl, (\blacksquare) CaCl_2 , and (\blacksquare)sodium citrate. The steady state MSD curves are depicted in the inset and the dotted lines represent $\tau=33$, 67, and 100 ms. (b) The transient slope ($\log(\text{MSD})$ vs. $\log(\tau)$) . (c) Numerical calculations of normalized solvent composition. 34
Figure 2.8:	(a) The transient slope at two different CaCl_2 concentrations: (\circ) 0.0278wt% and (\triangle) 0.111wt%. Solvents: (\square)NaCl, (\blacksquare) CaCl_2 , and (\blacksquare)sodium citrate. (b) Histograms of ($\log(\text{MSD})$ vs. $\log(\tau)$) slopes of individual particles at the three times marked in (a) for the 0.0278wt% sample. 36

- Figure 2.9: (a) Transient MSD of NaPSS at different NaCl concentrations. $\tau = (\blacktriangle)33$ ms, $(\triangle)67$ ms, $(\times)100$ ms, $(\bullet)133$ ms, and $(\circ)167$ ms. Solvents: (\square) 0.1M NaCl and (\blacksquare) 1M NaCl. (b) Transient viscosity (c) Numerical calculations of solvent composition. 41
- Figure 3.1: Transient MSD ($\tau = 0.167$ s) for alginate gelation, analyzed with different averaging intervals Δt ; the dashed line indicates the time ($t = 60$ s) at which the solvent was switched from 150mM NaCl to 0.11 wt% CaCl_2 . 51
- Figure 3.2: a) MSD vs. τ curves for individual tracers after 9 min dialysis against 50mM NaCl, averaged over time interval $\Delta t = 15$ s. Histograms of b) MSD values and c) slopes of $\log(\text{MSD})$ vs $\log(\tau)$ for heterogeneous BCP hydrogel in 50mM NaCl solution (solid line; data from a) and for homogeneous sodium alginate after dialysis against CaCl_2 (dotted line; data from Fig. 1 at $t = 120$ s). Contour plots of transient distribution of d) MSD values ($\tau = 0.167$ s) and e) slope ($t = 0.10 - 0.20$ s) for BCP sample during dialysis experiments; solvent is switched from DI water to 50mM NaCl at $t = 60$ s and back to DI water at $t = 660$ s. 55
- Figure 3.3: Transient average MSD and slope values ($\tau = 0.167$ s) as calculated with three different averaging methods: all particle analysis (thin solid), individual particle analysis (dotted), and weighted individual analysis (thick solid). a) average MSD values and b) slope for homogeneous sodium alginate sample, c) average MSD values and d) slope for heterogeneous BCP sample (0.15wt% $\text{K}_{160}\text{L}_{40}$), e) the normalized MSD difference between all particle analysis, (MSD_a), and weighted individual particle analysis (MSD_{wi}) for the heterogeneous BCP sample (data from c). 58, 59
- Figure 3.4: The effect of choice of Δt on a) the average MSD value ($\tau = 0.167$ s) for heterogeneous BCP sample (0.15wt% $\text{K}_{160}\text{L}_{40}$) and b) the number of particle trajectories that constitute the average. c) Transient non-Gaussian parameter, $\alpha(0.33$ s), of heterogeneous hydrogels with different Δt s and d) the number of displacements used to generate the Van Hove diagrams. The solvent was switched from DI-water to 50mM NaCl at 60s, and 50mM NaCl to DI-water at 660s. 62
- Figure 3.5: Transient dynamic moduli, a) G' (solid) and b) G'' (open), of 0.15wt. % $\text{K}_{160}\text{L}_{40}$ hydrogels analyzed with three different methods: all particle analysis (thin solid), individual particle analysis (dotted), and weighted individual particle analysis (thick solid). Solvent manipulation scheme during the experiment: DI-water (60s) \rightarrow 50mM NaCl (600s) \rightarrow DI-water (540s). 66

- Figure 4.1: LSCM and PT μ R. a) in DI-water before dialysis, b) in 50mM NaCl after 10min dialysis, c) in DI-water after salt removal, and d) in 50mM NaCl with macroscopic mixing. Viewing area of LSCM is 200 x 200 μ m, while PT μ R images with trajectory overlays are 40 x 40 μ m. e) steady state mean-squared displacements for a)-d); solid line represents MSD of particles in DI-water and the shaded region marks the lag times that were used for transient PT μ R in Fig. 4.2. 74, 75
- Figure 4.2: Snapshots of a transient confocal experiment; solvent is switched from DI water to 50mM NaCl at $t = 1$ min and back to DI water at $t = 11$ min. K₁₆₀L₄₀ 0.25wt.% with 50mM NaCl. Viewing area is 55 μ m x 55 μ m. 76, 77
- Figure 4.3: Transient PT μ R. Transient MSD distribution at $\tau = 0.1$ sec and sample heterogeneity α (insets) for a) 0.25wt.% K₁₆₀L₄₀ and 50mM NaCl, and b) 2.5wt.% K₁₈₀L₂₀ and 100mM NaCl. The dotted lines represent solvent switching. 79
- Figure 4.4: Rheology of 0.25wt.% K₁₆₀L₄₀ hydrogel at different NaCl concentrations. Non-Gaussian parameter α ($\tau = 0.33$), storage modulus G' (solid symbols), and loss modulus G'' (open symbols), after 10min dialysis (red circles) and with convective macromixing (black diamonds). Blue squares represent rheology of macromixed sample (100mM) after salt removal in the dialysis cell. 81
- Figure 4.5: Rheology of K₁₆₀L₄₀ hydrogels at different concentrations. Storage and loss moduli, G' and G'' in dialysis cell. Red circles: in DI-water before salt addition, blue squares: in 100mM NaCl after 10min dialysis, and green triangles: in DI-water after salt removal; arrows mark the critical gelation concentrations. 83
- Figure 5.1: Contour plots of transient histograms of slope and MSD values ($\tau = 0.167$ s) for K₁₆₀L₄₀ hydrogels at a) 0.1wt.%, b) 0.15wt.%, and c) 0.2wt.% with 0.37 μ m particles, 35 μ m from the bottom of the dialysis cell. Solvent manipulation sequence: DI-water (60s) \rightarrow 100mM NaCl (600s) \rightarrow DI-water (600s), solvent switches indicated by vertical lines. The dashed white curve represents the weighted average values for slope and MSD values. 94
- Figure 5.2: Contour plots of transient histograms of slope and MSD values ($\tau = 0.167$ s) for K₁₈₀L₂₀ hydrogels at a) 2.0wt.%, b) 2.5wt.%, and c) 3.5wt.% with 0.37 μ m particles, 35 μ m from the bottom of the dialysis cell. Solvent manipulation sequence: DI-water (60s) \rightarrow 100mM NaCl (600s) \rightarrow DI-water (600s), solvent switches indicated by vertical lines. The dashed white curve represents the weighted average values for slope and MSD values. 95

- Figure 5.3: The dynamic moduli, G' (solid symbols) and G'' (open), for a) $K_{160}L_{40}$ and b) $K_{180}L_{20}$ hydrogels as a function of BCP concentration at three stages of the dialysis cycle: in DI water (red circles), after addition of 100mM NaCl (blue squares), after removal of NaCl (green triangles); the gelation concentrations are identified by arrows. 98
- Figure 5.4: a) Transient non-Gaussian parameter α for two concentrations of $K_{160}L_{40}$ (0.15 and 0.25 wt.%) during a dialysis cycle, b) The effect of NaCl concentration on the sample heterogeneity for the same samples, and c) The effect of particle size on α at various concentrations of $K_{160}L_{40}$. 101
- Figure 5.5: Depth dependent a) dynamic moduli, G' (solid symbols) and G'' (open symbols), and b) non-Gaussian parameter α ($\tau=0.33s$) for 0.25wt. % $K_{160}L_{40}$ hydrogels at three stages of the dialysis cycle: in DI water (\bullet , \circ), after 10min dialysis against 100mM NaCl (\blacksquare , \square), and after 10min of salt removal with DI water (\blacktriangle , \triangle). The distance is measured from the bottom of the sample chamber as shown in the inset of b). 104
- Figure 5.6: LSCM images of 0.25 wt.% $K_{160}L_{40}$ hydrogel with evolving crack a) in DI water before addition of salt, b) in DI water after the addition and subsequent removal of 100mM NaCl; scale bar 10 μ m. 105
- Figure 5.7: a) Gelation behavior with 0.37mm particles, and b) the effect of particle size on MSDs, at different concentrations. 109
- Figure 5.8: Contour plots of transient histograms of MSDs during a) a repeatability test with 0.15wt. % $K_{160}L_{40}$ Hydrogels, b) a recovery test with 0.15wt. % $K_{160}L_{40}$ Hydrogels, c) a recovery test with 0.25wt. % $K_{160}L_{40}$ Hydrogels 111
- Figure 5.9: Lag time analysis. a) Example of a sigmoidal fitting curve for transition from salt-solution to DI water; the logarithmic half time was used to define the lag time. b) the effect of BCP concentration on the lag time for 100mM NaCl solutions. 113
- Figure 6.1: Step response curves of MSD ($\tau=0.033s$) for solutions of 0.25wt.% sodium alginate after changing solvent from 150mM NaCl solution to various $CaCl_2$ concentrations; solvent composition was changed at $t = 60s$. 122
- Figure 6.2: Time lag for alginate gel (0.25wt.%) formation and gel break-up function of $CaCl_2$ concentration; sodium citrate concentration during break-up was kept constant at 75mM. 122
- Figure 6.3: Schematic illustration of High-Throughput Characterization Device of solvent responsive complex fluids. 126

Figure 6.4: Examples of concentration array: a) two dimensional and c) three dimensional libraries. 127

Figure 6.5: An image of the dialysis cell with a silicon wafer. 129

LIST OF SYMBOLS

A	initial MSD
a	particle radius
α	non-Gaussian parameter
B	stepsize of MSD change
B_0	initial concentration for the fast gelation step
β	local logarithmic derivative of $\langle \Delta r^2(\tau) \rangle$
C	concentration of metal ion
d	sample thickness
d	dimensionality
d_s	solute diameter
d_p	pore diameter
D	diffusion coefficient
D_0	diffusion coefficient at infinite dilution
$D_{\text{membrane}}, D_{\text{eff}}$	effective diffusivity
ε	membrane porosity
G	($=\varepsilon/\tau$) geometrical factor
G'	storage modulus
G''	loss modulus
G^*	complex shear modulus
H	hindrance factor
H_r	reservoir height
H_s	sample chamber height

H_m	membrane thickness
η	solvent viscosity
i	particle ID
k	rate constant
k_B	Boltzmann's constant
L	shell thickness
L_{max}	maximum shell thickness
L_r	reservoir length
L_s	sample chamber length
n	rate constant
n	length of trajectory
P_0	initial concentration for the slow gelation step
r	inter-particle separation
r	particle displacement
R_f	first-order rate constant for the fast gelation step
R_s	first-order rate constant for the slow gelation step
s	Laplace frequency
t	clock time
t_l	lag time
t_D	characteristic diffusion time
T	temperature
τ	membrane tortuosity
τ	lag time
τ_l	characteristic timescale of the MSD response
τ_{max}	maximum lag time

v_x	the velocity in the x -direction
W_r	reservoir width
W_s	sample chamber width
W_m	membrane width
K	Lysine
L	Leucine

LIST OF ABBREVIATIONS

DWS	Diffusing wave spectroscopy
AFM	Atomic force microscopy
PT μ R	Particle tracking microrheology
GSE	Generalized Stokes-Einstein
Pe	Peclet number
FVM	Finite Volume Method
MSD	mean squared displacement
CSLM, LSCM	confocal scanning laser microscopy
NaPSS	Sodium polystyrene sulfonate
PEG	polyethylene glycol
BCPs	block copolypeptides
THF	Tetrahydrofuran
PDMS	Poly dimethyl siloxane
NTSC	National Television System Committee

SUMMARY

Stimuli-responsive hydrogels have diverse potential applications in the field of drug delivery, tissue engineering, agriculture, cosmetics, gene therapy, and as sensors and actuators due to their unique responsiveness to external signals, such as pH, temperature, and ionic strength. Understanding the responsiveness of hydrogel structure and rheology to these stimuli is essential for designing materials with desirable performance. However, no instrumentation and well-defined methodology are available to characterize the structural and rheological responses to rapid solvent changes. In this thesis, a new microrheology set-up is described, which allows us to quantitatively measure the transient rheological properties and microstructure of a variety of solvent-responsive complex fluids. The device was constructed by integrating particle tracking microrheology and microfluidics and offers unique experimental capabilities for performing solvent-response measurements on soft fragile materials without applying external shear forces. Transient analysis methods to quantitatively obtain rheological properties were also constructed, and guidelines for the trade-off between statistical validity and temporal resolution were developed to accurately capture physical transitions. Employing the new device and methodology, we successfully quantified the transient rheological and microstructural responses during gel formation and break-up, and viscosity changes of solvent-responsive complex fluids. The analysis method was expanded for heterogeneous samples, incorporating methods to quantify the microrheology of samples with broad distributions of individual particle dynamics. Transient microrheology measurements of fragile, heterogeneous, self-assembled block copolypeptide hydrogels revealed that solvent exchange via convective mixing and dialysis can lead to significantly different gel properties and that commonly applied sample preparation protocols for the characterization of soft biomaterials could lead to

erroneous conclusions about microstructural dynamics. Systematic investigations by varying key parameters, like molecular structure, gel concentration, salt concentration, and tracer particle size for microrheology, revealed that subtle variations in molecular architecture can cause major changes in response dynamics. Moreover, the results showed that the method can be applied for studying gel formation and breakup kinetics. The research in this thesis facilitates the design of solvent-responsive soft materials with appropriate microstructural dynamics for *in vivo* applications like tissue engineering and drug delivery, and can also be applied to study the effect of solvents on self-assembly mechanisms in other responsive soft materials, such as polymer solutions and colloidal dispersions.

CHAPTER 1

INTRODUCTION

1.1 BACKGROUND AND MOTIVATION

Complex fluids are ubiquitous in nature, everyday life, and industry: foods, biological fluids, personal care products, electronic and optical materials, polymer melts and solutions [1]. Many of these materials contain solvent-sensitive components, for example polyelectrolytes and surfactants that are used as viscosity modifiers to enable control over the microstructure and flow properties of complex fluids. Another example are stimuli-responsive hydrogels, which have attracted a lot of attention due to their unique responses to external stimuli like pH and solvent composition. Such hydrogels have potential applications in the fields of drug delivery, tissue engineering, agriculture, cosmetics, gene therapy, and as sensors and actuators [2-9].

For use as drug delivery vehicles, the microstructure of hydrogels needs to be controlled accurately, and rheological and volumetric changes of the gels need to be tuned carefully in order to trigger release of drug molecules under the appropriate physiological environmental conditions [10], *e.g.* pH, temperature, and ionic strength. Understanding the kinetics of the changes in microstructure and rheology that lead to drug release is crucial for targeted drug in specific locations of the gastrointestinal tract. When solvent responsive hydrogels are used as microfluidic valves for flow control applications, the mechanical strength and volume change must be optimized to achieve a rapid response of the valve and provide sufficient strength to close off the pressurized channel [10, 11]. Again, in this case, it is essential, that the response of the material is synchronized with the external solvent-based triggers.

Although characterization of bulk mechanical properties like swelling rate and stiffness is important, most biomedical applications require a detailed understanding of microstructure, heterogeneity and local mechanical properties. For drug delivery and tissue engineering applications, microstructural parameters like porosity, pore size distribution, tortuosity, and heterogeneity, are key quantities that control the molecular diffusion of many relevant species: drugs, nutrients, metabolites, and waste products. Controlling the transport of these molecules is critical for achieving controlled drug release and for maintaining viability of cells in a tissue construct [9, 10, 12, 13]. In addition to the microstructure, the local mechanical strength of tissue scaffolds needs to be controlled carefully to enable adequate support for growth and cell proliferation, while at the same time preventing damage to the cells when they are mixed and seeded into the gel [12]. Thus, in particular for biomaterial applications, understanding the responsiveness of hydrogel structure and rheology to environmental changes is essential for the design of materials with desirable performance on macroscopic and microscopic length scales. The test conditions should be similar to the physiological environment in which materials will ultimately be used, so that observed structural changes, such as gel formation and break-up, are representative for ultimate applications.

In order to optimize the mechanical properties of solvent-responsive complex fluids, it is necessary to have the experimental ability to monitor rheological quantities during solvent changes. For traditional mechanical rheometry [14], a sample must be mixed homogeneously, loaded into a rheometer, and rested before a measurement can be performed. As a result, only samples with slow dynamics can be investigated: the rheological properties must essentially remain unchanged during sample preparation and loading. It is challenging to manipulate the pH or salt concentration in a sample after loading, and therefore it is virtually impossible to measure the rheological response to controlled changes in solvent composition in a rheometer. For example, Goeden-Wood *et al.* recently attached a dialysis membrane around a cone-and-plate geometry to induce

pH-buffer exchange [15] during the preparation of solvent-sensitive peptide solutions. The authors waited for 12 hours to achieve equilibrium; the long waiting time was due to the large distance over which diffusive transport had to occur (12.5 mm, the cone radius) and thus it was impossible to resolve transient rheological changes in the sample. As a result of such experimental limitations, solvent composition has not been treated as a control parameter for the rheology of complex fluids as extensively as other environmental conditions like mechanical stress, temperature, UV-light, and electromagnetic fields.

Instead of measuring the full mechanical properties, the volumetric response (swelling) of thin polymer gel films (0.1~1 mm) to external stimuli has been researched extensively by reducing the diffusion length [16-20]. Experiments are typically carried out by immersing a sample directly into solvent and monitoring its volume or weight; this method can only be applied to highly cross-linked gels. In other work, photolithography has been used to create samples with a short diffusion path (200-400 nm) inside microfluidic devices (thickness ~50 μm) to investigate the time-dependent expansion of hydrogels [11, 21]. This approach is limited to photo-polymerizable polymers and shape changes are measured rather than mechanical properties. Similar perfusion chambers are common in cell physiology, tissue engineering and biochemistry: solvent is flown past tissue slices or cells and their response is monitored. Because the samples experience external shear stress in perfusion chambers, cells typically must be tethered inside the sample chamber [22].

For complex fluids with mobile macromolecular components, perfusion cells are unsuitable: it is necessary to seal off the sample from convective solvent flow in order to prevent sample components from being swept away. Dialysis membranes are used in many applications to achieve exchange of solvent and/or small solute molecules, while trapping macromolecular components. Although the dimensions of dialysis bags are generally too large to achieve rapid equilibration, diffusion through a thin, selective

membrane is an attractive mechanism for solvent exchange in small microfluidic devices. If we assume that the dimensions of a sample chamber are chosen so that diffusive transport can be considered one-dimensional, the characteristic diffusion time t_D is a function of the characteristic sample thickness d , and diffusion coefficient, D , of the diffusing agent: $t_D = d^2/2D$. The characteristic diffusion time increases quadratically as a function of sample thickness. In Table 1.1, diffusion times are plotted for Na^+ ions in DI water for sample chambers of varying thickness. While a sample of thickness 1cm requires more than ten hours of diffusion time, the characteristic time decreases to a few seconds for 100 μm thickness. This simple scaling argument shows that constructing a system with small sample dimensions would reduce the time scale for solvent exchange significantly.

Table 1.1 Characteristic diffusion time for Na^+ ions in DI water through samples of different thicknesses based on simple one-dimensional diffusion ($D=1.33 \times 10^{-9} \text{m}^2 \cdot \text{s}^{-1}$).

d	5cm	1cm	1mm	100 μm
t_D	10.8days	10.4hours	6.2minutes	3.7seconds

The challenge of using samples with small dimensions is that the sample volume also becomes extremely small (1 μl for sample with dimensions 10 x 1 x 0.1mm). Measuring mechanical properties and microstructure within such a small sample volume is not possible with conventional rheological techniques. Instead, recently developed microrheological techniques must be used.

1.2 MICRORHEOLOGY

Various microrheological techniques have been developed over the past decade to measure the viscoelastic properties of small samples and on micrometer length scales, including particle tracking microrheology (PT μ R), diffusing wave spectroscopy (DWS), optical tweezers, atomic force microscopy (AFM), and magnetic tweezers (reviewed in [23, 24]). All of these techniques have in common that they use microscopic probes to measure the mechanical properties of the medium and they can be classified into passive and active methods. Active methods (AFM, magnetic tweezers) generate an external force on the probes to drive their motion and measure the mechanical response due to the viscoelasticity of the medium. Passive methods, on the other hand, take advantage of the fact that microscopic probes exhibit detectable Brownian motion due to thermal fluctuations. By observing the motion of tracer particles due to this known stochastic thermal force, either via microscopy (PT μ R) or light scattering (DWS), the mechanical properties of the medium around the tracer particles can be extracted. Optical tweezers can be used to actively move tracer particles or to provide a well-defined potential well in which the particles can move around stochastically due to Brownian motion.

The active microrheological methods have the disadvantage that they are more invasive and could destroy the structure of fragile soft materials upon exerting an external force, which could irreversibly alter the mechanical properties of such materials. Even if the sample structure is reversible, active methods can be harmful. Once the microstructure is broken, a long waiting time can be required to achieve complete recovery of the sample strength and structure. In contrast, passive methods are suitable for fragile soft materials because the thermal nature of the particle motions ensure that the rheological properties are by definition obtained in the linear viscoelastic regime, in which the viscoelastic properties and microstructure do not change. This is advantageous, even in comparison with a rheometer, because it is unnecessary to

determine the critical strain through a strain sweep measurement before performing rheology measurements in a frequency domain. Even when performed carefully, strain sweeps bear the risk of destroying the initial sample structure. For viscous fluids, the measured viscosity with the passive microrheological methods corresponds to the zero-shear viscosity as measured with a rheometer. Rheological properties that are measured via passive microrheology are particularly relevant for materials that are used in environments where external shear stress is limited, *e.g.* drug delivery, tissue engineering, and concentrated colloidal suspensions. In this study, we employed video particle tracking microrheology (video-PT μ R) to monitor the structure and rheology of fragile, stimuli-responsive materials.

In PT μ R, the local dynamic moduli, G' and G'' , can be calculated from the mean-squared displacement (MSD) of tracer particles embedded in the sample [25, 26]. The relation between tracer motion and sample rheology is intuitive for the diffusive motion of spherical particles in purely viscous fluids. In liquid environments, the MSD of tracers grows linearly with time at a rate (see Fig. 1.1), the particle diffusivity, which is inversely proportional to the medium viscosity: in highly viscous samples particles move less than in low viscosity liquids. This well-known phenomenon is quantitatively described by the Stokes-Einstein relation that relates the diffusivity coefficient of a sphere to its radius and the viscosity of the medium: $D = k_B T / (6\pi\eta a)$. Similarly, the motion of particles in purely elastic gels is restricted to maximum displacements that are determined by sample elasticity. Because of the fixed thermal energy ($k_B T$), tracer particles will be able to move away from its equilibrium position until the elastic energy of the medium is equal to the thermal energy. As a result, MSD is limited to a maximum value (see Fig. 1.1) that is inversely proportional to the elastic modulus of the medium: small displacements in stiffer media.

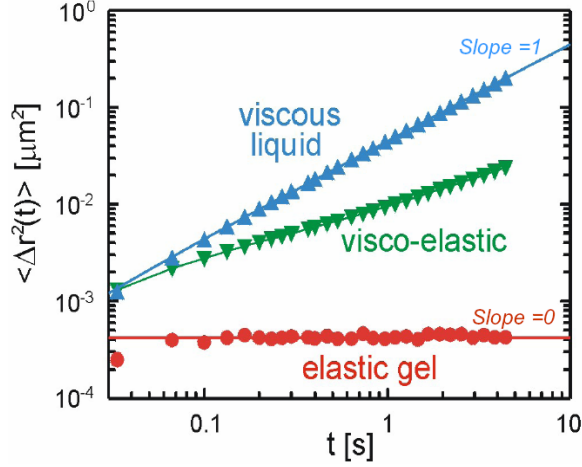


Figure 1.1 Mean-squared displacement as a function of lag time for tracer particle in various complex fluids. For viscous samples (\blacktriangle), the slope in the double logarithmic plot is 1, while for highly elastic gels (\bullet) it equals 0 (plateau); viscoelastic samples (\blacktriangledown) exhibit slope values between 0 and 1.

Recently, it has been shown that this concept can be extended to viscoelastic materials with complex rheological properties, via a frequency-dependent generalized Stokes-Einstein (GSE) equation [25, 26]. This GSE equation, which will be discussed in more detail in subsequent chapters is somewhat empirical and has limitations; it has been shown to be valid when 1) the inertial effects of particles and fluid are negligible, 2) no-slip condition holds at the particle-fluid interface, 3) compressibility of the medium is negligible, 4) the tracer particles are inert and do not alter the local rheology of the media, (for example, no polymer absorption on the particle surface and no depletion layer near the particle surface), 5) the particles do not interact with each other, 6) the medium is homogeneous and continuum models for viscoelasticity can be used [23, 27]. With these assumptions, microrheological properties represent the bulk rheological properties.

In particular the homogeneity requirement is a relevant limitation, since heterogeneity on the micrometer length scale (the typical tracer size) is common for many biomaterials and colloidal suspensions [28]. For such heterogeneous materials, various approaches have been proposed to provide a link between microrheology and

bulk rheology. The most successful one to date is so-called “two-point microrheology” [29, 30]. Instead of using the displacements of individual tracers, this method studies the hydrodynamic coupling between particles. In an incompressible medium, particles interact hydrodynamically so that their displacements are correlated. This correlation has a characteristic $1/r$ decay and the strength of the coupling depends on the mechanical properties of the medium, where r is a distance between particles [31]. As a result, the cross-correlation of particle displacements can be used to measure the rheological properties of the medium between particles. While the auto-correlation method of traditional PT μ R probes the direct environment around a particle ($\sim 1\mu\text{m}$), the two-particle technique probes the rheology over larger distances, the inter-particle separation ($\sim 1\text{-}10\mu\text{m}$). As a result, it has been a powerful tool [29] in bridging the gap between microrheology and macrorheological experiments with a rheometer. A number of studies have been performed in which rheometer data, two-point microrheology and one-point microrheology are compared to investigate samples with heterogeneous microstructures. The ultimate application has been referred to as “rheological microscopy” [32, 33] and would involve spatial maps of rheological properties in heterogeneous materials. In practice, when microrheology represents bulk rheology, it can be used as a direct alternative for macrorheology and enables advanced experimental techniques, such as high-throughput screening [24] of the rheology of a large number of samples with small sample volumes to construct phase diagrams. The high-throughput application showcased the strong potential of PT μ R for measurements with high temporal resolution in a small sample volume.

Since video-PT μ R requires relatively low capital investment, it has become easily accessible to many rheologists [23]. However, video microscopy has technical limits with regards to frequency range and spatial resolution that originate from camera design and fundamental optical limits [24]. The highest attainable frequency corresponds to the video frame rate. A standard NTSC video camera provides a frame rate of 30Hz, which

can be stretched to 60Hz by separating the even and odd fields of an image. Extension of the frequency range requires significantly more expensive high speed cameras, which often have low light sensitivity. The minimum frequency in PT μ R is determined by statistical validity and storage capacity of PCs. Because the mean-squared displacement of tracer particles generally grows with time, at very high frequencies, particle displacements can drop below the combined spatial resolution of the optical microscope, camera and image analysis methods. This sets limits to the highest frequency that can be used and restricts the range of measurable viscosity or elasticity [24]. One parameter that can be used to extend the range is particle size, because the mean-squared displacement is inversely proportional to the particle radius. Smaller particles have larger, and thus more easily detected, displacements. However, the particle size must be sufficiently large to be visible under an optical microscope (ca. 200nm), so that the range of useful particle sizes is limited. Consequently, because of spatial resolution and mechanical limitations, it is difficult to study viscoelastic behaviors of extremely stiff samples in high frequency regime. The upper limit of measurable viscoelastic modulus with video PT μ R is ~ 10 Pa [24]. In contrast, DWS allows a high spatial resolution and a high frequency, which leads a higher limit: $\sim 10^3$ Pa and $\sim 10^6$ Hz [23]. However, with DWS, no information can be obtained about local sample heterogeneity since the scattering technique determines an ensemble average over all particles in the scattering volume [34]. Therefore, video-PT μ R is preferable for heterogeneous samples, since one can track the motion of individual particles, from which local heterogeneity can be evaluated with a high spatial resolution.

Besides the limitations in mechanical settings and spatial resolution, statistical validity must be taken into account for obtaining accurate rheological properties from mean-squared displacements that are the result of stochastic thermal fluctuations. The number of independent contribution to the average must be sufficiently large. In principle, statistics improve with an increasing number of particles and/or number of

images (movie length). However, the tracer particle concentration cannot be too high because of detrimental particle-particle interactions and potential structural changes of the sample. Similarly, the movie length cannot be too long because of limited processing speed and storage capacity of available PCs. As a benchmark, the number of independent auto-correlation at a particular lag time is proposed to be at least 500 [24].

The limitations for typical “steady-state PT μ R” have been described above. When we attempt to monitor dynamically changing systems, steady-state PT μ R must be replaced with “transient PT μ R”. In this case, we need to consider another experimental limitation, temporal resolution, in order to understand the dynamics of the rheological and microstructural changes of responsive materials. However, the ideal methodology for transient PT μ R has not been determined in spite of rapidly growing need in many important rheological applications, such as gelation processes, phase transitions, and biochemical processes [23, 35-38].

1.3 OBJECTIVES AND OUTLINE

The summary of limitations of currently available technologies provided above clarifies the key issues in analyzing the transient microrheology and microrheology of heterogeneous, soft, solvent-responsive materials (*e.g.* polymer solutions, biological assemblies, and colloidal suspensions):

- i) unavailability of an experimental tool for rapidly manipulating solvent composition in soft materials without applying external shear stress
- ii) lack of well-defined methodology to quantitatively monitor microstructure and mechanical strength of responsive soft materials with high temporal resolution.

The first goal of this study is to construct a novel instrument which allows us to rapidly change the solvent composition in a complex fluid sample, while

microrheological measurements can be performed simultaneously to monitor the structural and rheological changes. The second goal is to construct a proper analysis framework to accurately monitor physical transitions and quantify rheological properties and heterogeneity. With the constructed instrument and methodology, the aim is to study various solvent-responsive materials with transient PT μ R during liquid-gel transitions, viscosity changes, and microstructural evolutions to validate the new technique and systematically investigate the effects of experimental conditions on the rheology and microstructure.

The outline of the thesis is as follows. Chapter 2 describes the design and construction of a new microdialysis cell which allows us to quantitatively measure the transient rheological properties of solvent-responsive complex fluids. The device integrates particle tracking microrheology with microfluidics and consists of a reservoir, porous dialysis membrane, and sample chamber. Solvent molecules can freely diffuse between the reservoir and the sample chamber while macromolecular components are trapped in the sample chamber with a rigid semi-permeable dialysis membrane. The design enables manipulation of the solvent composition in the sample chamber by simply switching the fluid composition in the reservoir. The details of the concept, manufacturing, and quantitative validation of solvent transport are presented and the applicability of the device for microrheological measurements of solvent-responsive complex fluids is demonstrated.

Chapter 3 is dedicated to the analysis of transient microrheological data that can be acquired with a dialysis cell. PT μ R employs statistical methods to quantify the mobility of colloidal tracer particles in a medium and translate this information into local mechanical properties. Although the methodology for homogeneous samples under steady-state conditions is well-established, challenges arise when applying PT μ R to samples with dynamically changing, heterogeneous microstructures. Since such samples are the primary target of the microdialysis cell, there is a need to formulate a

methodology before the dialysis cell is applied to such materials. The chapter focuses on the trade-off between statistical validity and temporal resolution in transient PT μ R experiments and the averaging methods that are used to determine an ensemble-averaged mean-squared displacement. Also, methods are proposed for the calculation of transient dynamic moduli and transient heterogeneity.

A challenge in designing hydrogels with well-defined responsiveness to external environmental stimuli is to quantify their microstructure under conditions that mimic *in vivo* environments, in which mass transport of solvent components is dominated by diffusion. Unlike most *in vitro* characterization methods that generally require convective mixing during sample preparation, the dialysis cell provides the opportunity to study materials under diffusive solvent transport conditions. In Chapter 4, the microstructural evolution of self-assembled block copolypeptide hydrogels was studied via microrheology and confocal microscopy in the dialysis cell and compared to results for convectively mixed samples.

Chapter 5 finally describes an in-depth study on the effect of molecular architecture on the transient microstructural and rheological response of the block copolypeptide gels. In order to provide quantitative guidance for the design of these responsive biomaterials, we systematically investigated the effects of hydrogel concentration, molecular structure, salt concentration, location in a dialysis cell, and tracer particle size. Complex solvent exchange schemes, including reversible and repetitive solvent exchanges, were applied to investigate the salt-responsive behavior of these materials.

CHAPTER 2

A NEW DEVICE FOR MEASURING TRANSIENT RHEOLOGY OF SOLVENT-RESPONSIVE COMPLEX FLUIDS ¹

2.1 INTRODUCTION

In the previous chapter, an overview was presented of studies that give valuable background information for the design of a system to measure time-dependent mechanical properties of complex fluids in response to changes in solvent composition. One of the conclusions was that diffusion through a dialysis membrane would be an excellent method for solvent manipulation in macromolecular fluids without applying shear stress, but that samples must be thin to reach acceptable response times. Moreover, the membrane must be selective: permeable to solvent molecules, but not to the macromolecular components of interest. To minimize the hydrodynamic stress that cells experience in a perfusion chamber, McGrath et al. constructed a diffusion chamber for an optical microscope to study the osmotic response of cells to solvent exchange, [39]. Cells were entrapped inside a thin cell compartment ($\sim 100\ \mu\text{m}$), which was sealed off with a thin dialysis membrane ($\sim 16\ \mu\text{m}$). Rapid exchange could be achieved through diffusion from the external flow side of the chamber to the cell compartment. Transient concentration histories in the cell compartment were measured with electro-conductivity [40], and controlled with a computer, although a detailed description has not been published [41]. The authors successfully monitored the dynamic osmotic response of

¹ The contents of this chapter has been published:

Sato, J. and Breedveld, V., "Transient rheology of solvent-responsive complex fluids by integrating microfluidics and microrheology", *Journal of Rheology* 50 (1), 1-19 (2006).

individual cells with microscopy, but did not measure mechanical properties during the solvent changes. Several experimental problems were reported [42]: fragility of the membrane, introduction of air bubbles, and mobility of cells inside the cell compartment.

With a similar device, Hou *et al.* studied the transient co-polymerization process of F-actin and filamin [43]. In addition to direct visualization of the growing actin network, the Brownian motion of premixed tracer particles was used to qualitatively monitor structural changes of the polymer network. However, in these experiments the time scales of the diffusion process were not precisely determined, and significant lag times were observed, most likely due to Taylor dispersion in the inlet tubing. Quantitative rheological characterization of the polymerization process was not performed.

For measuring rheology in small sample volumes, particle-tracking microrheology has become a well-established non-invasive method [25, 26]. Microrheology requires only a small sample size ($\sim\mu\text{l}$) for rheological measurements, much less than conventional mechanical rheometers, which require at least hundreds of μl . Microfluidic techniques enable the construction of small-scale sample geometries in which particle-tracking microrheology can be performed [44]. The goal of our work was to construct a novel microrheology set-up for measuring the transient rheological properties of complex fluids in response to solvent change by combining particle tracking microrheology and microfluidics in a dialysis cell for microrheology.

2.2 DIALYSIS CELL

2.2.1 GENERAL IDEA

Conceptually, the dialysis cell is based on a three-layer geometry: a reservoir channel that is connected to an external flow loop, a rigid porous membrane, and a sample chamber of constant volume. The entire system must be configured so that it can be mounted on an inverted microscope to enable particle tracking microrheology as shown in Fig. 1.1. The solvent composition in the reservoir can then simply be controlled by manipulating the fluid flow. Solvent molecules in the reservoir can diffuse freely in and out of the sample through the porous membrane. Large molecules within the sample chamber cannot diffuse out, provided that the membrane has the appropriate size-selectivity.

Based on the simple one-dimensional scaling argument demonstrated in the introduction (see Table 1.1), the characteristic diffusion time of several hours that was observed for a 25mm diameter cone-and-plate geometry [15] should decrease to a few seconds for a sample thickness of 0.10mm.

Rapid and reversible changes of sample solvent composition can be achieved by switching the external flow through a supply system of syringe pumps, tubing and valves, provided that transport limitations in the flow loop (*e.g.* Taylor dispersion) are eliminated. Fluorescent tracer particles can be premixed with the sample to enable rheological measurements throughout a solvent-exchange experiment via particle tracking microrheology. The transient rheological response of a sample can thus be measured with high temporal resolution.

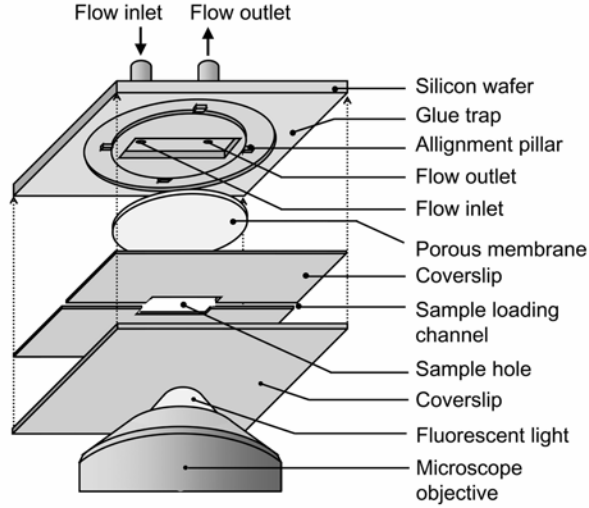


Figure 2.1 Schematic representation of the dialysis cell.

2.2.2 NUMERICAL CALCULATION

The transient concentration profiles in the dialysis cell were calculated numerically to characterize the mass transport, and to determine dimensions and flow conditions that would lead to the desired responsiveness of the dialysis cell. For a similar device, McGrath obtained numerical results that indicated that membrane diffusion was the rate-limiting process, but detailed results have not been published.

The three-dimensional geometry of the dialysis cell is shown in Fig. 2.2a which depicts only half of the cell for clarity. The cross-sectional aspect ratio, W_r/H_r , in the reservoir is 15. As illustrated in the sketch, the velocity profile in the y -direction is plug-like while the profile in the z -direction is parabolic [45]. The sample chamber is narrower than the reservoir and aligned with the center of the reservoir, so that the velocity profile is nearly independent of y in the contact area with the sample. As a result, one can ignore velocity gradients in the y -direction at high Peclet number conditions ($Pe = W_r \cdot v_x / D$, v_x being the velocity in the x -direction) and assume two-dimensional mass transport.

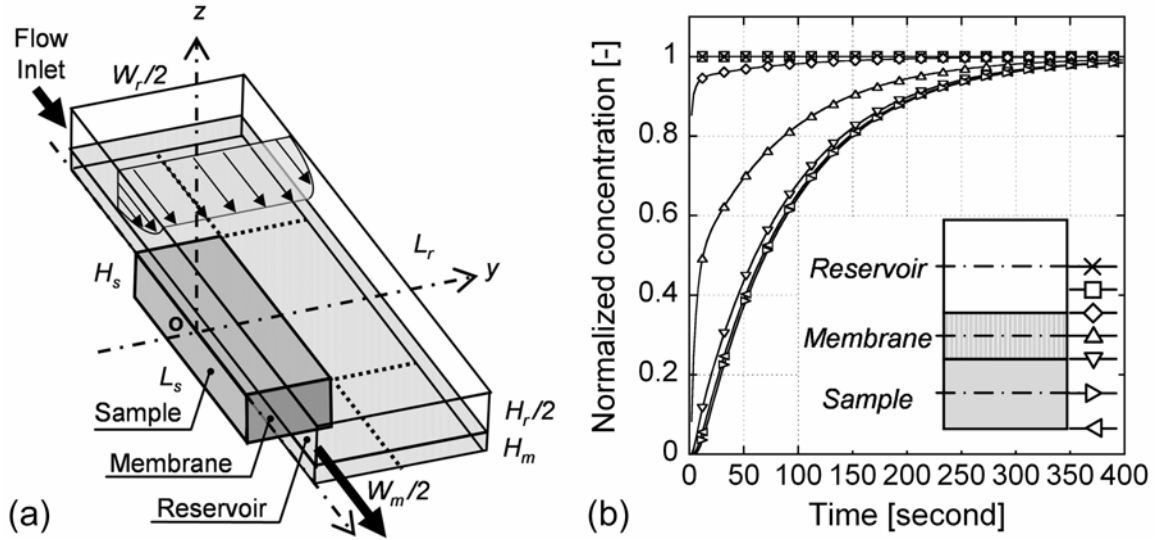


Figure 2.2 (a) Three-dimensional geometry of the dialysis cell (only one half shown for clarity): $H_r=200\ \mu\text{m}$, $H_m=60\ \mu\text{m}$, $H_s=120\ \mu\text{m}$, $L_r=1\ \text{cm}$, $L_s=5\ \text{mm}$, $W_r=3\ \text{mm}$, $W_m=1.5\ \text{mm}$. A sketch of the velocity profiles in the reservoir is also included. (b) Time-dependent concentration profiles of Ca^{2+} ions, calculated with a Finite Volume Method at: reservoir centerline (×), halfway between reservoir centerline and bottom (□), reservoir bottom (◇), membrane center (△), sample top (▽), sample center (▷), and sample bottom (◁) (see inset). Pressure gradient is $-3810\ \text{Pa}\cdot\text{m}^{-1}$ and viscosity is $1\ \text{mPa}$. $D_0=7.92\cdot 10^{-10}\ \text{m}^2\cdot\text{s}^{-1}$, $G=0.15$, $H=0.88$, and $x_{\text{test}}=5000\ \mu\text{m}$. The membrane is AnodiscTM (20 nm nominal pore diameter, 25~30% porosity).d

Since transport in the device involves both diffusion and convection, a Finite Volume Method (FVM) was used to eliminate numerical diffusion in solving the convection-diffusion equation by using a finite volume discretization formulation. [46]. Key assumptions used for the calculation are: 1) transport is two-dimensional and no diffusion occurs in the y -direction, and 2) homogeneous concentration changes occur at the reservoir inlet immediately after switching the solvent composition, thereby neglecting the effect of Taylor dispersion in the tubing between switching valve and reservoir inlet. Appropriate mesh sizes and timesteps were chosen for the calculation. Flow conditions were set to achieve a realistic average velocity in the reservoir of $1.25 \cdot 10^{-2}$ m/s [45]. The diffusion coefficient used in the calculations was $7.92 \cdot 10^{-10}$ m²·s⁻¹, the literature value for Ca²⁺ at infinite dilution [47]. The average velocity is $1.26 \cdot 10^{-2}$ m·s⁻¹.

For hindered diffusion of solute through liquid-filled pores, the effective diffusion coefficient in the membrane can be written as [48, 49],

$$D_{\text{membrane}} = H \frac{\varepsilon}{\tau} D_0 \equiv H \cdot G \cdot D_0. \quad (2.1)$$

D_{membrane} and D_0 are the effective diffusivity and the diffusivity of solute at infinite dilution. ε , τ , and H are respectively the membrane porosity, tortuosity, and hindrance factor due to the finite pore sizes. H is a function of the ratio of solute diameter, d_s , to pore diameter, d_p : $\lambda = d_s/d_p$; H becomes 1 when $\lambda = 0$. ε and τ are geometrical factors, so that $G (= \varepsilon/\tau)$ should be determined only by the membrane structure and be constant for specific membrane. For the calculations presented in this section, we used $G = 0.15$ (see section 2.4.1 for the origin of this value) which is equivalent to an effective diffusion coefficient of $1.1 \cdot 10^{-10}$ m²·s⁻¹ for calcium ions. In this study, our samples consist of polymer solutions in deionized water at less than one weight percent of polymer. Therefore, the D_0 in the sample layer is assumed to be the same as D_0 in deionized water. For alginate gels, this assumption was confirmed by Tanaka *et al.* [50].

Time-dependent concentration profiles at $x = 2.5$ mm (the middle of the sample chamber) are shown in Fig. 2.2b for 7 different z -locations: the centerline of the reservoir; the midpoint between the centerline of the reservoir and the membrane; the bottom of the reservoir; the middle of the membrane; and the top, middle and bottom of the sample layer (see legend). After the concentration at the reservoir inlet was changed in a stepwise manner, the concentrations across the reservoir responded rapidly: the final concentration at the centerline of the reservoir is reached within a few seconds. A noticeable delay was observed at the top surface of the membrane, which results from slow convective transport in the proximity of the membrane. The concentration response on the sample side of the membrane is much slower. There is not a significant difference between the concentration curves at different locations in the sample chamber, which proves that transport through the membrane is the rate-limiting process, in agreement with literature [39]. The concentrations in the sample chamber reach about 50% of the inlet concentration after one minute, 90% after a few minutes, and asymptotically approach the inlet concentration.

2.2.3 MICROFABRICATION

Photolithographical techniques were employed to construct the dialysis cell. The dialysis cell was constructed from three elements: a top part, the membrane and a bottom part (Fig. 2.1). The top part has four distinct features: a rectangular reservoir channel, circular membrane insert, a trench for application of adhesives, and holes for flow inlet/outlet. The bottom part consists of a glass coverslip with a rectangular hole to serve as sample chamber, and a second coverslip that seals the sample and enables optical access on an inverted microscope.

The top structure was etched in silicon wafer (475-575 μm thick, NOVA Electronic Materials, Ltd). Chrome photomasks were manufactured on borofloat substrate (1.1 mm thick, TELIC Co., Ltd). A positive photoresist (4620, Clariant Co.)

was spin-coated (~15 μm thick) on the silicon wafer and softbaked on a hotplate (CEE 100CB, Brewerscience, Inc.). The wafer was then exposed to UV-light (2000 mW/cm^2 , OAI Mask Alignment and UV Exposure System, Optical Associates, Inc) and immersed in AZ400K developer 1:4 (Clariant Co.) for several minutes to finish patterning. Features were then fabricated with plasma etching (Dual ICP SLR Mn F. Model, Plasma Therm Inc.) and the dry etching was completed by rinsing the photoresist. The fabrication process was repeated with different masks in the following order: 1) the trench for application of adhesives, 2) the circular membrane insert, 3) the reservoir channel, and 4) the inlet/outlet holes. As a dialysis membrane, Anodisc™ aluminum oxide membranes were selected because of their small thickness and high rigidity (13 mm diameter, 60 μm thick, 20 nm nominal pore diameter, 25~30% porosity; Whatman International Ltd).

Fig. 2.1 illustrates how the dialysis cell was assembled. The circular membrane fits in the insert and is aligned with four pillars. A diamond cutter was used to cut the rectangular hole for the sample chamber (5 x 1.5 mm) in a No. 0 cover slip, which was then split into half. The two pieces were placed onto the silicon wafer and membrane with a small separation, thus forming a narrow channel for sample loading. Capillary forces are responsible for filling all cracks with UV-glue (B-690-0, Bohle), which was then cured through exposure to UV light. Subsequently, the second cover slip (No.1.5) was placed onto the assembly and fixed with UV glue as well. Thermally curable adhesive (N-100-01, Upchurch Scientific) was used to attach connectors (N-333, Upchurch Scientific) to the flow inlet/outlet ports of the dialysis cell.

Before sample loading, the inlet and outlet ports of the reservoir were connected to flexible tubing filled with solvent. By adjusting the relative vertical position of the membrane and the tubing, the effects of hydrostatic pressure were minimized to eliminate pressure-driven transport between sample and reservoir and facilitate sample loading. The sample chamber has a volume of approximately 0.9 μl and can be filled with a

pipette. Even highly viscous or viscoelastic samples can be loaded into the device by placing the sample at one end of the channel and creating underpressure at the other end to suck the sample into the chamber. After loading the sample, quick-dry nail polish was used to seal both ends of the channel. In some cases (*i.e.* polyelectrolyte solutions with high osmotic pressure), polymer adhesive melts were used to reinforcing the seal. The dialysis cell makes it possible to load a sample quickly and confine it to the sample chamber of constant volume without leakage.

2.2.4 FLOW SYSTEM

An aluminum foundation was designed to mount the dialysis cell and tubing on a Leica DM-IRB inverted microscope, which is placed on an air table to dampen external vibrations. The flow system is shown in Fig. 2.3. Two syringes were connected to a syringe pump (KDS210C, KD Scientific Inc.) and a four-port switching valve (V-101D, Upchurch Scientific) was placed in the tubing upstream of the dialysis cell. Both syringes were connected to the inlet ports of the valve. One of the outlet ports led to the reservoir channel and then emptied into a drain tank, while the other outlet led directly to the drain tank. This set-up enables rapid switching between two source fluids during continuous operation of the syringe pump. In order to minimize the dead volume between valve and dialysis cell, and thus the response time of the system, fine tubing (0.25mm diameter, PEEKTM, Upchurch Scientific) was used to connect the valve and dialysis cell. Larger tubing (1mm diameter, PEEKTM, Upchurch Scientific) was used between reservoir outlet and drain tank to minimize pressure drops. The flow rate can readily be measured by monitoring the weight of the drain tank with an analytical balance.

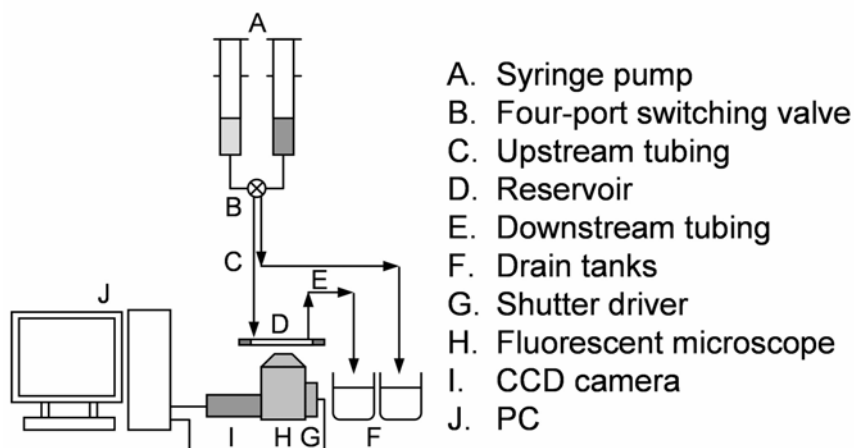


Figure 2.3 Flow system and measuring system.

2.3 VIDEO MICROSCOPY AND MICRORHEOLOGY

The microscope was equipped with an analog 640 x 480 pixel CCD camera (30Hz frame rate, COHU 4920, Poway, CA), which was connected to a PC. Images were transferred to the PC and recorded real-time with a precision frame grabber (PXC-200, Cyber Optics) and specialized image acquisition software (OpenBox) [51]. A high-speed shutter (Uniblitz® VMM-D1, Vincent Associates Inc.) was inserted in the microscope fluorescent light path, so that illumination could be controlled via a LabView interface. The resolution with 63x and 100x objectives was 0.157 μm per pixel and 0.099 μm per pixel, respectively. Fluorescent probe particles were selected so that their surface chemistry was compatible with sample properties: negatively charged carboxylate-modified or positively charged amine-modified polystyrene particles of various sizes (0.37~2 μm diameter, Molecular Probes Co.). The probe particles were premixed in the samples ($\sim 5.8 \cdot 10^6$ particles/ μl sample) so that rheological properties could be measured by carrying out particle tracking microrheology [24-26] according to the scheme outlined in Fig. 2.4.

Particle tracking microrheology takes advantage of a generalized Stokes-Einstein

relation:

$$\langle \Delta \tilde{r}^2(s) \rangle = \frac{d k_B T}{3\pi a s \tilde{G}(s)}, \quad (2.2)$$

where $\langle \Delta \tilde{r}^2(s) \rangle$ is the Laplace transform of the mean-squared-displacement (MSD) $\langle \Delta r^2(\tau) \rangle$, τ is the lag time, s is the Laplace frequency, a is the radius of the tracer particles, k_B is Boltzmann's constant, T is the absolute temperature, and d is the dimensionality of the displacement vector Δr . In our experiments, particle positions and trajectories were detected through image analysis with the software package IDL (Research Systems Inc.), using algorithms developed by Crocker and co-workers [52]. The MSD was calculated based on these trajectories. Equation (2.2) can then be used to find $\tilde{G}(s)$ and the complex shear modulus: $G^*(\omega) = G'(\omega) + iG''(\omega)$ by substituting $i\omega$ for the Laplace frequency s [53]. For viscous liquids, the slope of MSD vs. τ in a double-logarithmic plot is 1, while for elastic gels, MSD reaches a plateau with increasing lag time.

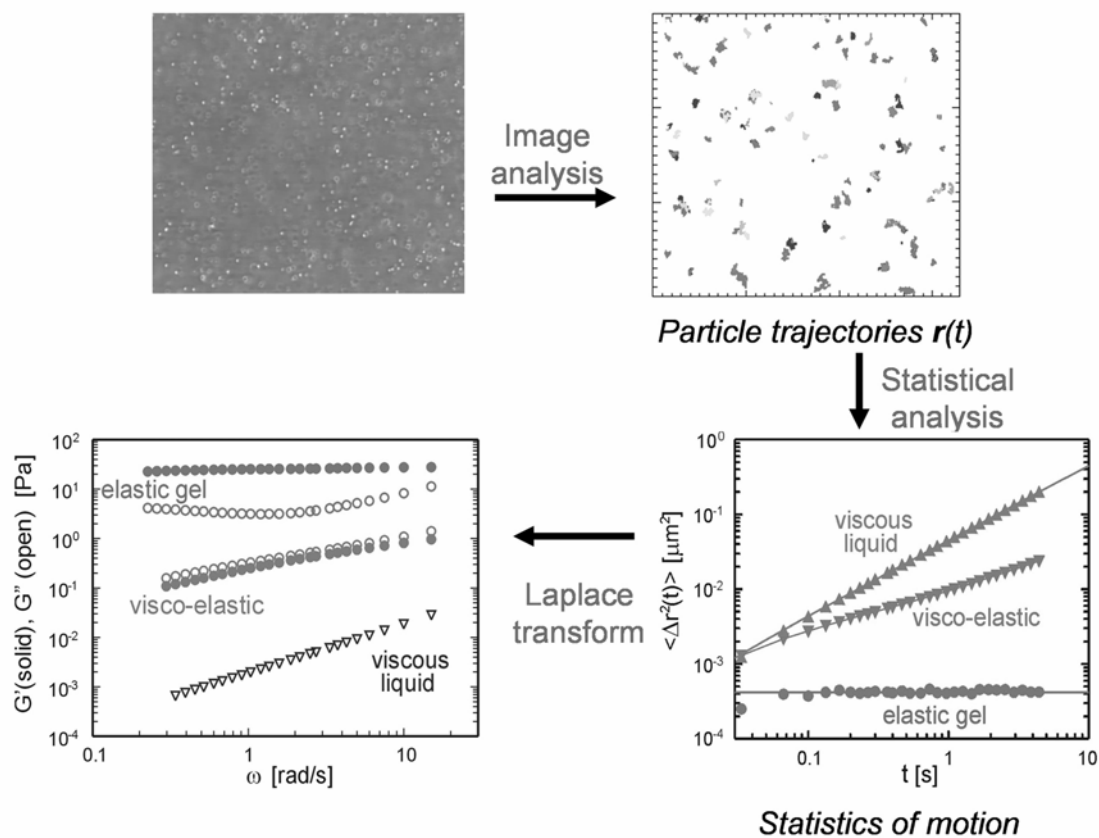


Figure 2.4 Diagram of microrheology system.

In standard microrheology experiments, it is generally assumed that the rheological properties do not change during the image acquisition and the MSD is averaged over the entire length of the movie. In transient experiments with the dialysis cell, however, the MSD must be determined as a function of both the lag time τ and the clock time, t . This is achieved by cutting the initial trajectories into segments of duration Δt and calculating MSD as the average over the time interval from $t - \frac{1}{2}\Delta t$ to $t + \frac{1}{2}\Delta t$:

$$\langle \Delta r^2(\tau, t, \Delta t) \rangle = \langle \Delta r^2(\tau) \rangle_{(t-\frac{1}{2}\Delta t, t+\frac{1}{2}\Delta t)} \quad (2.3)$$

By following this strategy, we can monitor the rheological response of a sample to solvent composition changes. The interval length Δt must be chosen with two primary concerns in mind: statistical validity and temporal resolution. To minimize statistical errors, Eq. (2.3) must satisfy the condition: $\Delta t \gg \tau_{\max}$, where τ_{\max} is the maximum lag time at which the MSD is to be determined. If Δt is of the same magnitude as τ_{\max} , $\langle \Delta r^2(\tau_{\max}) \rangle$ involves significant statistical errors because of averaging over a small number of independent data points Δr within the interval Δt . On the other hand, a large value of Δt leads to poor temporal resolution and reduces the experimental ability to accurately capture physical transitions in a sample. To balance these requirements, we generally limit the range of our lag times by choosing relatively small values of τ_{\max} . To ensure statistical validity, all MSD values were calculated by taking the ensemble average of at least 1000 independent contributions [24]. For highly viscous or elastic samples, MSD values at short lag times τ can be very small, and sometimes be close to the spatial detection limit. In preliminary investigations (not reported here), the spatial resolution of the experimental set-up used in this study was measured by embedding particles in highly elastic gels: the minimum attainable MSD was $\sim 2 \cdot 10^{-5} \mu\text{m}^2$, which corresponds to tracer displacements of 4-5 nm. In the current study Δt was varied from

1.3~2.6 second (40~80 video frames), which is small enough to accurately capture the physical transitions in our samples (see Figs. 2.7, 2.8 and 2.9).

2.4 EXPERIMENTS

2.4.1 TRANSPORT VALIDATION WITH FLUORESCEIN SOLUTION

After fabrication, the performance of the dialysis cell was validated by comparing experimental transient concentration curves to the results obtained from numerical calculations (section IIB). In these validation experiments, we used fluorescein (F-6377 Sigma) which has a molecular size that is small enough to diffuse freely through the membrane pores, and a known diffusion coefficient of $5.2 \cdot 10^{-10} \text{ m}^2 \cdot \text{s}^{-1}$ [54]. Also, the concentration of aqueous fluorescein solutions can be measured with digital video-microscopy by constructing a calibration curve between image brightness and fluorescein concentration. With our 8-bit CCD camera, image brightness is quantified digitally in the range between 0 and 255 and in order to obtain good experimental resolution, the brightness needs to cover a wide dynamic range. Taking this into account, the concentrations of the fluorescein samples for the calibration curve were chosen between 0.01mM and 0.075mM. A 100x oil immersion objective was used to minimize the depth of focus and background fluorescence. Any remaining background signal due to fluorescein in the reservoir could clearly be identified and subtracted from the measured transient brightness.

To minimize the effect of photobleaching on the transient concentration curves, experiments were performed using brief (70 ms) exposures of the sample to fluorescent light, followed by longer dark intervals. For the 0.075 mM fluorescein solution, experiments were carried out with dark interval lengths of 2, 6, 10, and 14 seconds. The excellent agreement between all curves (not shown here) proved that experimental

parameters sufficiently eliminated photobleaching effects. To further validate our results, we used confocal scanning laser microscopy (CSLM) (VT-eye, VisiTech International) for a single control experiment. CSLM has been widely used for measuring the local diffusion coefficient of fluorescent dyes [54] and has the distinct advantage that background brightness is minimized due to an extremely small depth of focus. The CSLM results agreed very well with fluorescence microscopy experiments, providing final proof that fluorescence microscopy can be used for quantitative measurements of fluorescein concentrations. To maximize temporal resolution, we then used 70 msec exposure intervals and 2 second dark intervals for subsequent validation experiments.

The equilibrium brightness at different fluorescein concentrations was measured 16 minutes after switching the reservoir flow from DI-water to fluorescein solution and used to construct the calibration curve between concentration and brightness (inset of Fig. 2.5b). The calibration curve was linear over the entire range of concentrations, so that brightness data could easily be converted to concentrations and normalized by the known inlet concentration.

Next, the fluorescein concentration was changed in a stepwise fashion from low concentration to high concentration as listed in Table 2.1. This approach was chosen to eliminate potential effects of adsorption of fluorescein molecules on the membrane surface. The membrane pretreatment was performed for 15 min before the image acquisition was started. The reservoir flow was switched to higher fluorescein concentrations after 1 minute and back to the initial concentration after 16 minutes. The experiments were repeated with different initial concentrations (0.04 mM and 0.06 mM) and a fixed final concentration (0.075 mM). Brightness was measured throughout the experiments (Fig. 2.5a) and converted to normalized concentration curves following the method described above (Fig. 2.5b).

Table 2.1 Composition of the reservoir flow during validation experiments with fluorescein solutions. Fluorescein concentrations were varied.

Switching time	Interval [minutes]	Reservoir flow
0	15	Surface pretreatment
1	1	Low fluorescein concentration
16	15	High fluorescein concentration
31	15	Low fluorescein concentration

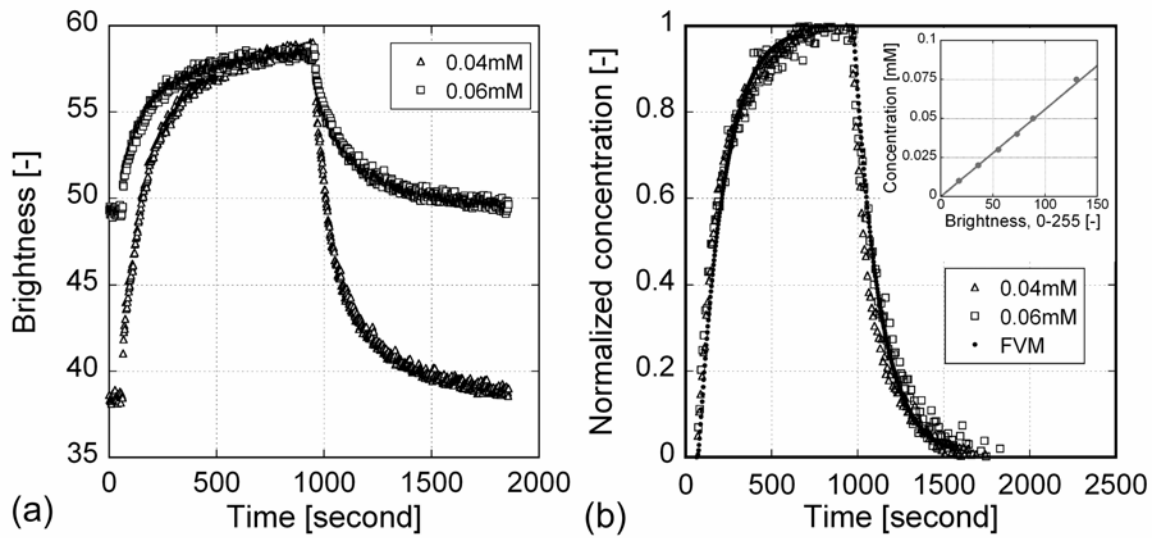


Figure 2.5 (a) Transient brightness for two different fluorescein concentrations, (b) Normalized concentration curves and results of numerical calculations with $D_0=5.2 \cdot 10^{-10} \text{ m}^2 \cdot \text{s}^{-1}$, $G=0.15$, and $H=0.82$. Calibration curve for fluorescein is depicted in the inset.

If the porosity and tortuosity of the membrane are precisely known and the membrane structure is simple, one can calculate G directly from these geometry parameters (Eq. (2.1)). However, Anopore membranes have a complicated tree-like structure which contains a number of branches, curves and tapers with a wide pore size distribution [55-58] and the reported porosity values depend on experimental method [59]. Therefore, we used G as a fitting parameter to match experimental and numerical results. The calculations were iterated with different values of D_{eff} until the results fitted the experimental data (Fig. 2.5b). The hindrance factor H was calculated as 0.83, based on the hydrodynamic radius of fluorescein $\sim 0.45\text{nm}$ [60] and nominal pore size of 200 \AA . With the obtained D_{eff} , G was then calculated to be 0.15 (Eq. (2.1)). This geometrical factor is a material constant for the membrane. In the subsequent experiments, $G = 0.15$ was used to estimate effective diffusion coefficients D_{eff} for other solutes, such as Ca^{2+} and Na^+ .

2.4.2 SODIUM ALGINATE GELATION

After design and construction of the dialysis cell and validation of its transport properties, the device was applied to study two materials with interesting rheological behavior: aqueous solutions of sodium alginate and sodium polystyrene sulfonate (NaPSS). The rheological properties of both materials can be changed dramatically by manipulating the solvent composition: liquid-to-gel-to-liquid transitions for sodium alginate and viscosity changes for NaPSS. The goal was to monitor the transient microrheology during solvent exchanges and demonstrate the applicability of the dialysis cell for different systems.

Sodium alginate is a polysaccharide that consists of 2 different monomers: 1,4-linked β -D-mannuronic and α -L-guluronic acid. In solution, it can form a gel by crosslinking with divalent cations like Ca^{2+} [61, 62] through the formation of a so-called “egg box” structure [63, 64]. The gel breaks up upon addition of chelating agents, *e.g.*

sodium citrate, which form complexes with multivalent cations and thus extract Ca^{2+} from the gel [65, 66].

For sample preparation, 1 g stock solution of 1.0 wt% sodium alginate in 150 mM NaCl (Keltone LVCR®, ICP) was prepared, mixed on a vortex mixer, and left over night. Subsequently, 25 mg of this stock solution was mixed with 150 mM NaCl solution and carboxylate modified fluorescent particles (F8819, 1.0 μm diameter, Molecular Probes). The tracer particles were dispersed homogeneously throughout the sample and the final alginate concentration was adjusted to be 0.25 wt%.

The solvent composition in the sodium alginate sample was changed according to the program listed in Table 2.2. The reservoir flow started with 150 mM NaCl. After one minute, the reservoir flow was switched to a CaCl_2 solution, after which Ca^{2+} ions could freely diffuse into the sample chamber filled with the aqueous sodium alginate solution. Then, the reservoir fluid was changed to a solution of chelating agent, 75 mM sodium citrate, which can diffuse through the membrane pores as well. Finally, the CaCl_2 solution was applied again. The experiment was performed with different CaCl_2 concentrations ranging from 0.028 wt% to 1.11 wt%.

In order to benchmark the microrheological measurements, the particle mean-squared displacement was first determined in the dialysis cell at steady state before and after gel formation; the MSD vs. τ curves are shown in Fig. 2.6. Note that τ can be large for these steady state experiments, since there are no temporal resolution limitations (Eq. (2.3)). The slope in the double-logarithmic plot of the MSD curve before gel formation was 0.962, which indicates that tracer particles exhibited free diffusion and the sample behaved like a Newtonian liquid. The corresponding viscosity was calculated to be 2.94 mPa·s. After exposure to Ca^{2+} , the slope of the MSD curve decreased dramatically and became 0.031, the signature of a highly elastic gel.

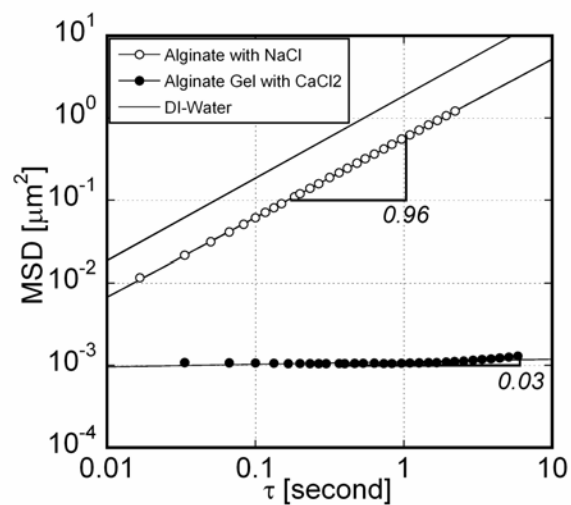


Figure 2.6 MSD vs. τ . (\circ) before gel formation and (\bullet) after gel formation for 0.25 wt% alginate solution in 150 mM NaCl and 0.111 wt% CaCl_2 .

Table 2.2 Composition of the reservoir flow during sodium alginate experiment. CaCl_2 concentration was varied.

Switching time	Interval [minutes]	Reservoir flow
0		
1	1	150mM NaCl
6	5	CaCl_2
11	5	75mM sodium citrate
16	5	CaCl_2

To confirm the accuracy of microrheological experiments, a direct comparison with macrorheology was made. A stock solution (1.0 wt% sodium alginate, 600 mM NaCl) was prepared in a vial and mixed on a vortex mixer. After leaving the sample for 48 hours, the stock solution was diluted with DI-water and fluorescent probe particles were added, so that a 0.25 wt% Alginate solution in 150 mM NaCl was obtained. Samples were loaded between a microscope slide and a coverslip, using paraffin film as spacer and tightly sealing the sample holder with vacuum grease. The viscosity for the sample was 2.47 mPa·s. For the same sample, viscosity measurements were also performed on a controlled stress rheometer (MCR300, Anton Paar) with a cone-and-plate geometry (50 mm diameter, 1° angle). The measured viscosity was 2.57 mPa·s, which is in good agreement with the microrheology results for the sample. The deviation from the transient microrheology results in the dialysis cell listed above must originate from differences in sample preparation history. In the dialysis cell, samples are dialyzed continuously, while the experiments in a closed sample cell do not enable ion-exchange processes. From the direct comparison with rheometer measurements, we conclude that microrheology quantitatively measures the bulk rheological properties of alginate solutions.

In transient experiments, the slope of MSD vs. τ must be determined for short lag times τ , much shorter than the time scale of physical property changes (Fig. 2.7a). The three curves in Fig. 2.7a represents the transient behavior of MSD at lag times $\tau = 0.033$, 0.067, and 0.1 seconds, which correspond to the dotted lines in the inset. The results in Fig. 2.7a show excellent recovery of viscous properties after inducing gel break-up with sodium citrate. If alginate molecules had diffused out from the sample chamber during the measurement, the alginate concentration and viscosity would have decreased and thus the MSD would have increased. The absence of such effects proves the selectivity of the dialysis membrane for the alginate solution. Upon gel formation and breakup, non-diffusive convective motion of the tracer particles was observed. This is the result of

macroscopic gel shrinkage and swelling, which is commonly observed during formation of polymer gels. The effect of the convective motion on the calculated MSDs was eliminated by subtracting the average motion from the individual particle trajectories.

By applying a linear curve fit to the double-logarithmic plot of MSD vs. τ , the slope of the double-logarithmic plot was obtained as a function of time (Fig. 2.7b). Initially, the slope was equal to 1 in the presence of NaCl and decreased to 0 after the addition of CaCl_2 . By adding sodium citrate, the slope increased again and recovered its initial value of 1. After switching to CaCl_2 for a second time, the slope decreased once again to 0. This can directly be interpreted as a sequence of liquid \rightarrow gel \rightarrow liquid \rightarrow gel transitions. Qualitative observations of particle motion coincide with these slope changes. Excellent reversibility was observed in response to the reservoir fluid changes and the experiments underline that mass transport through the membrane was fast as a result of the small sample dimensions. The slope and MSDs reached a saturated value after each stepwise solvent change, indicating that the time intervals in Table 2.2 were appropriate to capture the full rheological transition.

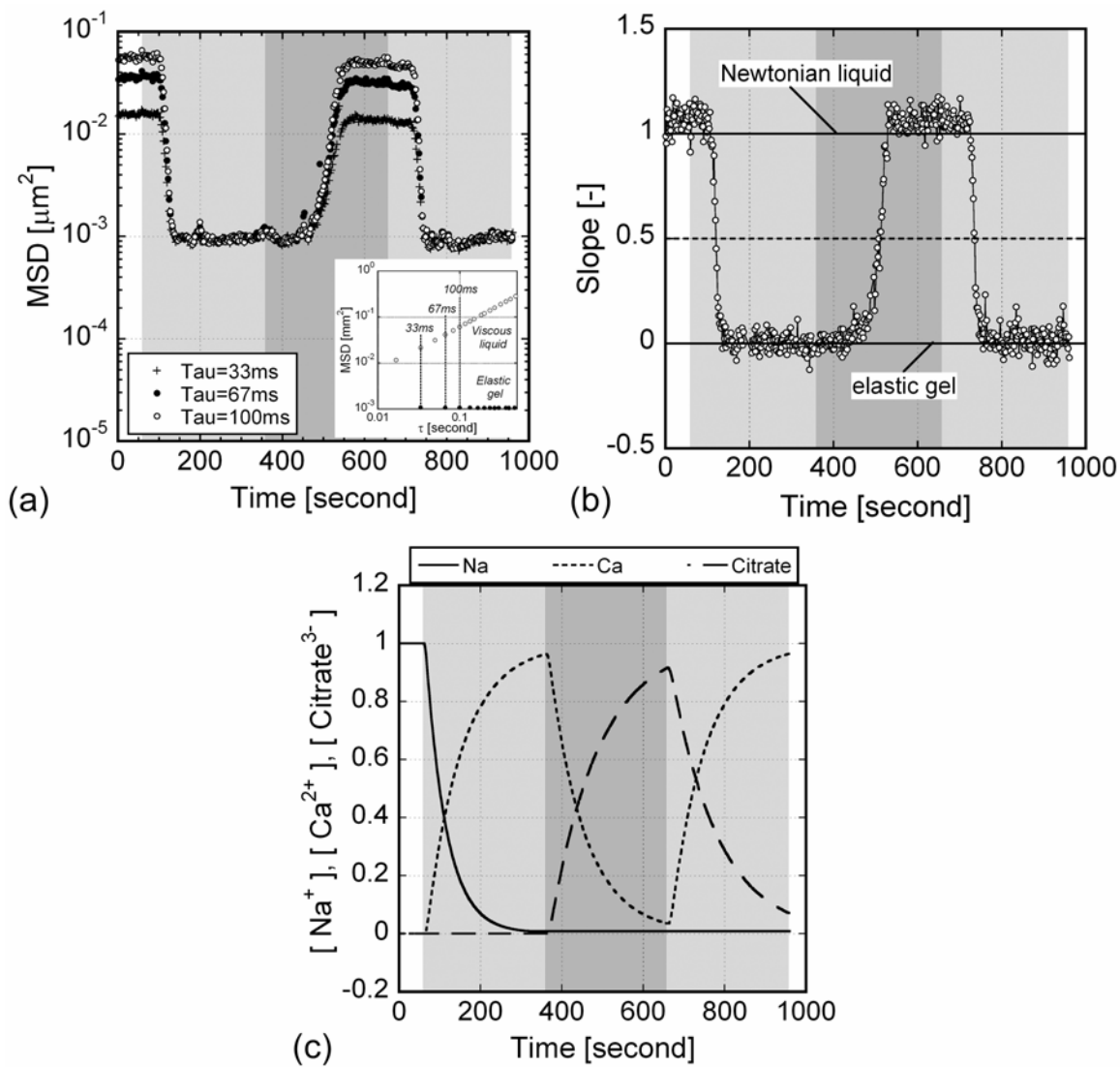


Figure 2.7 (a) The transient MSD: $\tau = (+)33\text{ms}$, $(\bullet)67\text{ms}$, and $(\circ)100\text{ms}$, solvents: $(\square)\text{NaCl}$, $(\blacksquare)\text{CaCl}_2$, and $(\blacksquare)\text{sodium citrate}$. The steady state MSD curves are depicted in the inset and the dotted lines represent $\tau = 33, 67$, and 100ms . (b) The transient slope ($\log(\text{MSD})$ vs. $\log(\tau)$). (c) Numerical calculations of normalized solvent composition.

The concentration profiles of all three solutes (NaCl, CaCl₂ and sodium citrate) were also determined through numerical calculations and are presented in Fig. 2.7c. Comparison between Figs. 2.7a, 2.7b and 2.7c shows that there are subtleties in the relation between rheological transitions and solute concentrations. These details are related to the kinetics of gel formation and can be emphasized by performing experiments at different solute concentrations. Fig. 2.8a shows the response curves for two experiments with different CaCl₂ concentrations. As the CaCl₂ concentration in the reservoir flow increases, the liquid-to-gel transition occurs more rapidly: the more calcium is supplied to the sample, the faster the alginate gel is expected to form. Gel break-up, on the other hand, is delayed by increasing the CaCl₂ concentration: at higher CaCl₂ concentrations more Ca²⁺ ions must be chelated by incoming citrate to achieve gel break-up. Citrate ions are initially consumed by free Ca²⁺ ions in solution, before reaction with calcium ions in the gel can occur. It is clear that the response curves are very sensitive to the balance between reactants.

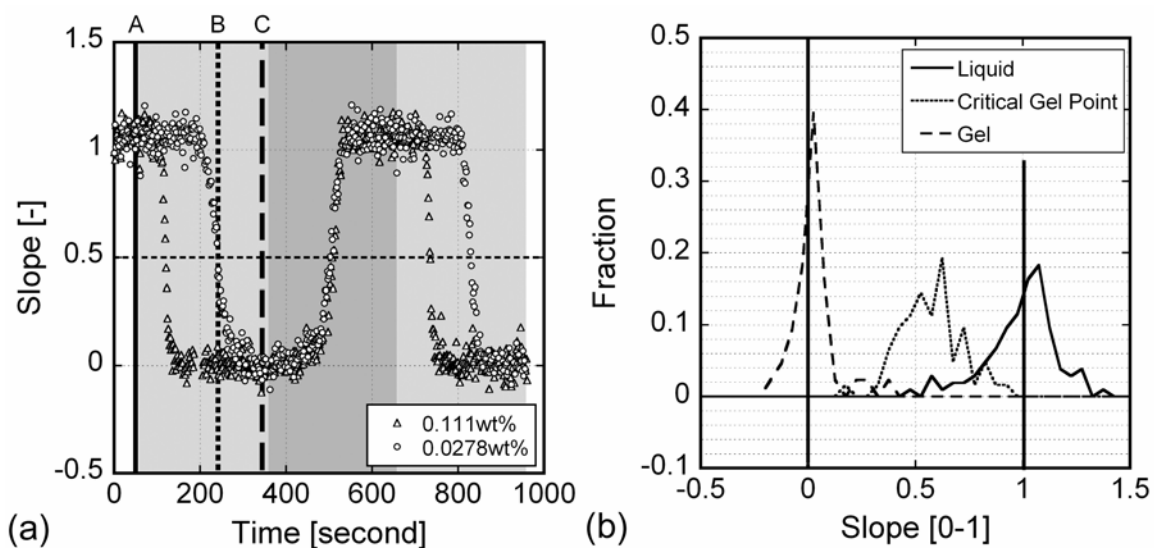


Figure 2.8 (a) The transient slope at two different CaCl_2 concentrations: (\circ) 0.0278wt% and (\triangle) 0.111wt%. Solvents: (\square) NaCl, (\blacksquare) CaCl_2 , and (\blacksquare) sodium citrate. (b) Histograms of $(\log(\text{MSD}) \text{ vs. } \log(\tau))$ slopes of individual particles at the three times marked in (a) for the 0.0278wt% sample.

The dotted-lines in the Fig. 2.7b and Fig. 2.8a denote the occurrence of slope = 0.5 in the MSD- τ -plot, which we chose to represent the gel point. A widely accepted definition of the critical gel point is a concentration at which $G' \sim G'' \sim \omega^{0.5}$, G' and G'' being the storage modulus and loss modulus and ω the angular frequency [67]. The relation $G' \sim G'' \sim \omega^{0.5}$ reduces to $\langle \Delta r^2(\tau) \rangle \sim \tau^{0.5}$ for microrheological measurements, which in turn corresponds to slope = 0.5 in a double-logarithmic plot of MSD versus τ (Fig. 2.7b and Fig. 2.8a).

The gelation experiments were repeated at different locations in the sample chamber between the membrane and the bottom of the chamber. The gelation times after switching the fluid flow were determined at each location (not shown here) and found to increase for larger distances to the membrane. The lag time at the top of the sample chamber was approximately 10 seconds longer than at the bottom, which is in good agreement with the predictions from numerical calculations (Fig. 2.2b). The dialysis cell enables tracking of the gelation front by varying the location of the focal plane of the microscope.

To investigate the homogeneity of the sample during gelation, the MSDs of individual particles were determined for three time intervals of 15 seconds (Fig. 2.8a): in the liquid state, around the ensemble averaged gel point, and in the gel state. For each particle, a linear fit in a double-logarithmic plot of MSD vs. τ was used to extract the slope and Fig. 2.8b shows the histograms of the slope distributions during the three intervals. In the liquid and gel state, clear peaks were observed around 0 and 1, the expected values for liquid-like and gel-like samples (see also Fig. 2.6). For homogeneous samples, one would expect to find narrow peaks. However, the finite width of the peaks in Fig. 2.8b should not be attributed to heterogeneity, but is the result of insufficient statistical information to accurately determine the slope for individual particles. This conclusion is supported by the occurrence of unphysical negative slope values in the gel

state. The most significant result in Fig. 2.8b is the slope distribution at the gelation point. If gelation would have occurred heterogeneously, one would expect to see a very broad distribution of slopes, some particles being in a liquid environment (slope 1) and others embedded in an elastic gel (slope 0). Instead, the middle peak in Fig. 2.8b has a width that is similar to the distribution in the liquid state. Therefore, it can be concluded that no significant heterogeneity occurred within the field of view during gelation.

The transient experiments and trajectory analysis on the alginate samples illustrate that the dialysis cell with particle tracking microrheology is a powerful tool for monitoring sample rheology in response to solvent changes. The device enables accurate and quantitative measurements of liquid-to-gel transitions, tracking the progression of the gel front, and detecting (in)homogeneity of the sample. The determination of transient rheological properties makes it possible to investigate the dynamics of complex fluids in ways that would be impossible with macrorheological measurements on a rheometer.

2.4.3 NAPSS POLYELECTROLYTE VISCOSITY

Sodium polystyrene sulfonate is a polyelectrolyte, which in aqueous solution is highly salt-sensitive, because Coulombic repulsion between charged monomers plays a major role in the polymer conformation. The viscosity of aqueous solutions dramatically drops upon the addition of salt, *e.g.* KBr and NaCl [68, 69], due to the screening of intra- and intermolecular electrostatic interactions. The steady shear viscosity of NaPSS has been reported in literature; at low shear rates, NaPSS solutions were found to exhibit Newtonian behavior both before and after the addition of salt [68]. We chose this polyelectrolyte for further exploration of the capabilities of the dialysis cell.

A stock solution of 10 wt% NaPSS (Mw1,200,000, #628, Scientific Polymer Product Inc) was prepared in a vial and mixed well with DI-water on a vortex mixer. After leaving the sample for 48 hours, the stock solution was diluted with DI-water and fluorescent probe particles were added, so that a 5 wt% NaPSS solution was obtained.

The surface of carboxylate modified fluorescent polystyrene particles (F8819, 1 μm diameter, IDC) was modified with polyethylene glycol (PEG) [70] in order to prevent particle aggregation due to interactions between the particles and NaPSS polymer chains. The particle size of the functionalized particles was calibrated in DI-water and the average particle diameter was 1.03 μm .

Analogous to the sodium alginate experiments, we performed reversibility experiments. Table 2.3 lists a typical program of solvent manipulation. The reservoir flow started with 0.1 M NaCl, was switched to 1 M NaCl, and then switched back to 0.1 M NaCl.

Table 2.3 Composition of the reservoir flow during NaPSS experiments

Switching time	Interval [minutes]	Reservoir flow
0	}	0.1 M NaCl
1		
3		
6	}	1 M NaCl
	}	0.1 M NaCl

Transient response curves for five different τ values with interval length $\Delta t = 3$ sec are shown in Fig. 2.9a. The MSD increased with the addition of salt and decreased when the sample was dialyzed at low salt concentration. The observed reversibility again proves the selectivity of the membrane as discussed in section 2.4.2 for alginate. The time intervals of the solvent exchange were chosen so that the MSD reached a plateau region in each interval. The MSD increased with τ in all solvents, which indicates that the samples exhibited liquid-like behavior at all NaCl concentrations. For liquid-like samples, the viscosity can be obtained from the Stokes-Einstein equation: $\langle \Delta \tilde{r}^2(\tau) \rangle = 2dD\tau$, where $D = k_B T / 6\pi\eta a$, d is the dimensionality of the displacement vector Δr , a is the tracer particle radius and η is the solvent viscosity. The resulting transient viscosity curve is shown in Fig. 2.9b. A rapid response of viscosity to

solvent change was observed. The inset in Fig. 2.9b shows the slope of the MSD- τ -plot as a function of time and confirms that the sample behaved like a Newtonian fluid at all times.

To confirm that the viscosity response yields quantitatively correct values, steady state microrheology experiments were performed (see section 2.5.1 for details). Stock solutions of 10 wt% NaPSS in 0.2 M and 2 M NaCl were prepared and mixed in different vials. After leaving them for 48 hours, the stock solutions were diluted with DI-water and fluorescent probe particles, so that 5 wt% NaPSS solutions in respectively 0.1 M and 1 M NaCl were obtained. The microrheological viscosities of the sample were found to be 37.5 mPa·s for 0.1 M NaCl solution and 14.1 mPa·s for 1 M NaCl solution. As mentioned previously, the deviation from the viscosity found in transient experiments originates from the difference in sample treatment: in the dialysis cell, the sample is in continuous contact with a solvent stream of constant composition. Viscosity measurements were also performed on a controlled stress rheometer (see section 2.5.1). The rheometer data showed Newtonian behavior for both samples in the low shear region, and zero-shear viscosities of respectively 37.1 mPa·s and 13.5 mPa·s, in excellent agreement with steady state microrheology. These results prove that microrheology yields bulk rheological properties for NaPSS solutions and that transient microrheology can be used to quantitatively capture the changes of sample rheology.

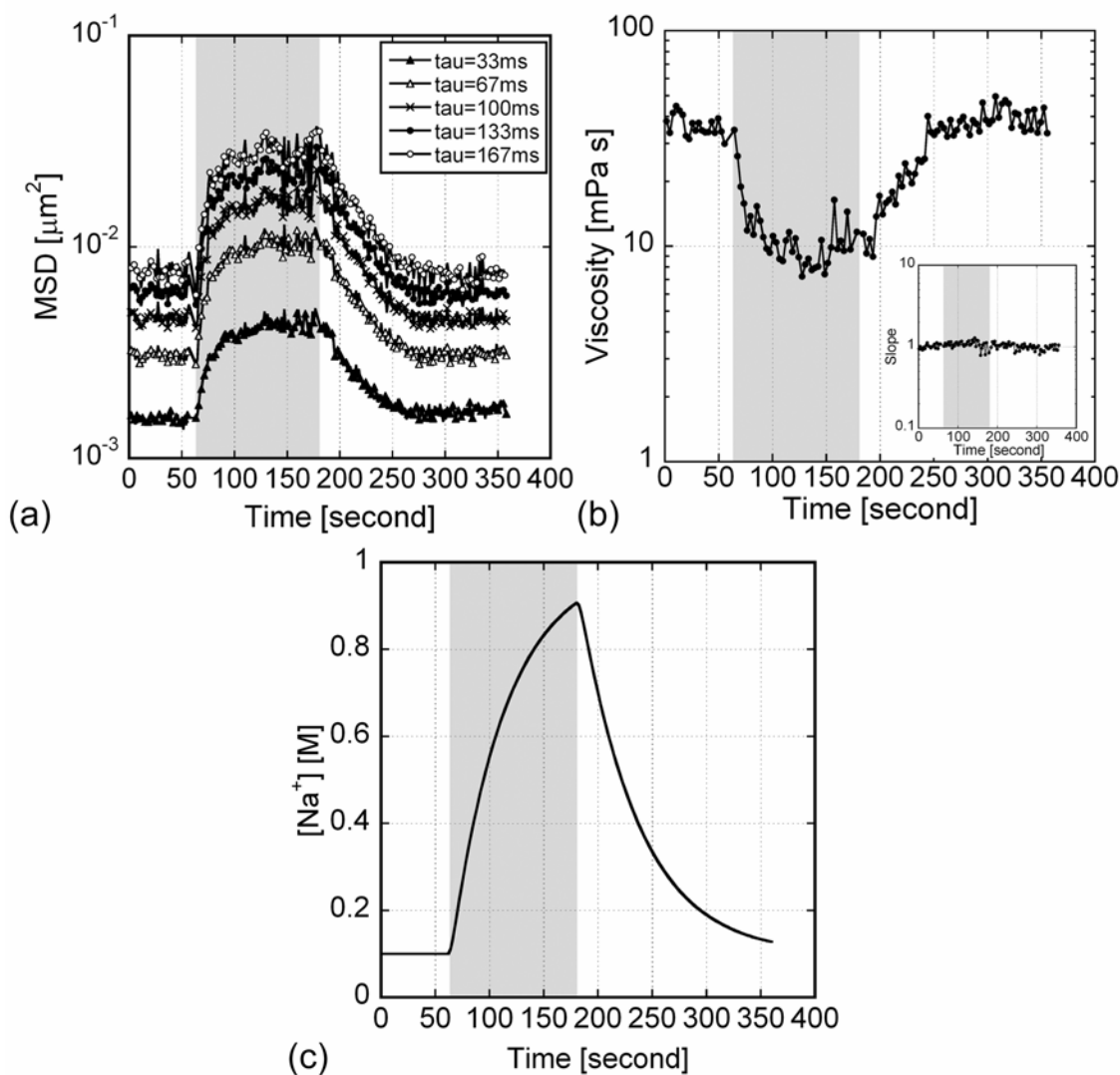


Figure 2.9 (a) Transient MSD of NaPSS at different NaCl concentrations. $\tau = (\blacktriangle) 33$ ms, $(\triangle) 67$ ms, $(\times) 100$ ms, $(\bullet) 133$ ms, and $(\circ) 167$ ms. Solvents: (\square) 0.1M NaCl and (\blacksquare) 1M NaCl. (b) Transient viscosity (c) Numerical calculations of solvent composition.

2.6 CONCLUSION

A new dialysis cell for microrheology was constructed by integrating particle tracking microrheology and microfluidics. The device enables quantitative measurements of the transient rheological response of complex fluids to changes in solvent composition. Such experiments are not possible in a traditional mechanical rheometer. We characterized the diffusion process in the dialysis cell both experimentally and numerically, and were able to manipulate solvent composition in a controlled and predictable fashion with a characteristic response time of a few minutes. In future designs, we plan to shorten the diffusive timescale even further by using shorter diffusion paths. As an example of applications for this new device, we successfully quantified the transient rheological responses of the liquid-gel transition of sodium alginate hydrogels in the presence of multivalent cations and the changes in viscosity of NaPSS solutions as a result of variations in ionic strength. This study introduces a new paradigm for microrheological studies that is applicable to a wide variety of solvent-responsive complex fluids.

CHAPTER 3

TRANSIENT PARTICLE TRACKING MICRORHEOLOGY OF HETEROGENEOUS SAMPLES²

3.1 INTRODUCTION

In recent years, particle tracking microrheology (PT μ R) has proven to be a powerful method to study the local linear viscoelastic properties of complex fluids [23, 28, 71, 72]. In passive PT μ R, thermal fluctuations of tracer particles embedded in a sample probe the microenvironment surrounding the particles, and rheological properties can be calculated from the particle displacement statistics [25, 26, 53, 73]. Microrheological properties typically are in good agreement with the bulk rheology for homogeneous samples in which the probe particles are much larger than the characteristic length scale or mesh size of the microstructure as shown in Chapter 2 [74]. Since all tracer particles represent the same local microenvironment in such samples, taking an ensemble average over all particle displacements is suitable for characterizing the local rheology. On the other hand, when the size of tracer particles is similar to or smaller than the characteristic microstructural length scale of the samples, individual tracers typically experience different mechanical environments and consequently the connection between microrheology and bulk rheology becomes more complicated. Examples of such samples reported in the literature are actin solutions [29, 32, 74-81], human lamin networks [82],

² The contents of this chapter have been submitted for publication:
Sato, J. and Breedveld, V., "Transient particle tracking microrheology of heterogeneous samples".

semidilute DNA solutions [33, 83, 84], keratin [85], agarose [78], amphiphilic block copolymer solution [27], Carbopol [86], aqueous poly(vinyl alcohol) solutions [87], poly acrylamide solution [88], guar, living cells [38, 89-91], human cystic fibrotic sputum [92], and wheat gliadin suspensions [80]. Because of the heterogeneity of these materials, it is not appropriate to simply calculate the ensemble average of all tracer particle displacements in these samples. Instead, it is necessary to analyze the distribution of individual particle displacements [78, 93], which is possible with video-PT μ R but not with scattering techniques like diffusing wave spectroscopy (DWS) that inherently provide ensemble-averaged displacements [34]. Several researchers, notably Wirtz and co-workers,[37, 38, 82, 84, 89, 92, 94, 95] have proposed histogram-based methods to measure the heterogeneity of soft materials with PT μ R. In their approach, the mean-squared displacement (MSD) is calculated for individual particles. The variability of MSD (and thus viscosity [84]) across the tracer population is then quantified and visualized in histograms. The width and shape of the distribution in these histograms (rank-order, median, standard deviation, and “skewness” [37, 82, 84, 89, 93-95]) have been used as measures of heterogeneity. The statistical challenge of this approach is that generating accurate histograms requires more independent data points for each particle than calculating the ensemble-averaged MSD. An alternative approach to address heterogeneity in PT μ R experiments is the two-particle method developed by Crocker *et al.* [29, 30]. This technique uses the correlated motion between two tracer particles to extract information about the average rheology of the medium in between the tracers. The main advantage is that microstructural heterogeneity on the particle length scale, for example due to interactions between particle surface and medium, has little impact on the measurements. However, the method requires many particle displacements and a high tracer density in order to obtain accurate data, and the ensemble-averaging obstructs detailed studies of sample heterogeneity.

Statistical limitations of PT μ R become even more pronounced when the technique is applied to complex fluids with a dynamically changing microstructure, for example in case of gelation, melting or aging. For such materials, it is of interest to monitor the microstructural evolution with the appropriate temporal resolution [23]. The aim would be to capture changes in microrheology and heterogeneity in order to obtain full understanding of sample dynamics. As mentioned above, DWS-based microrheology is not suitable to track spatially heterogeneous samples with high spatial resolution, although the high data acquisition rate enables transient measurements with excellent temporal resolution. DWS has been used to evaluate sol-gel transitions in concentrated colloidal suspensions [35, 36, 96] and to capture the gelation process of starch [97]. However, in these experiments no significant insight was obtained about the sample spatial heterogeneity.

Video-PT μ R, on the other hand, offers excellent spatial resolution due to the inherent knowledge about each tracer's location, but the data acquisition rate is typically 30 frames per second for standard video cameras. As a result, a trade-off exists between statistical validity and temporal resolution when monitoring rapid microrheological transitions with PT μ R [23, 80, 98]. For example, PT μ R was applied to measure temporal variations of the mechanical strength of lamellae in living cells with fairly high temporal resolution (15s per data point) [38]. However, details of the analysis method were not provided, and sample heterogeneity was not quantified. The same research group also studied the evolution of *f*-actin network compliance and focused on sample heterogeneity by evaluating the MSD values of individual particles [37]. The temporal resolution was rather poor (8min per data point) and although the evolution of heterogeneity was captured qualitatively, it was not well quantified. In our own research group, we recently employed transient PT μ R for monitoring rapid rheological changes of sodium alginate and sodium polystyrene sulfonate solutions in response to changes in solvent composition with high temporal resolution (12~15s); both of these samples were homogeneous [98].

The above summary of the transient microrheology literature exposes an area that has not been explored systematically: transient video-PT μ R of heterogeneous complex fluids. In this paper, we aim to explore the statistical limitations of such experiments and to provide insight into the optimization of analysis parameters in order to combine high temporal resolution with statistical validity. We present a framework for data analysis that combines the analysis of individual particle trajectories with a quantitative definition of heterogeneity. We also propose a method to translate transient mean-squared displacement data for heterogeneous samples into standard rheological quantities, the storage and loss moduli.

3.2 METHODS AND MATERIALS

3.2.1 MICRORHEOLOGY

Particle tracking microrheology determines the rheological properties of a sample by tracking the motion of Brownian tracer particles and takes advantage of the generalized Stokes-Einstein relation (GSE) [25, 26, 53]:

$$\langle \Delta \tilde{r}^2(s) \rangle = \frac{dk_B T}{3\pi a s \tilde{G}(s)}, \quad (2.2)$$

where $\langle \Delta \tilde{r}^2(s) \rangle$ is the Laplace transform of the mean-squared displacement (MSD) of the tracer particles, $\langle \Delta r^2(\tau) \rangle$, τ is the lag time, s is the Laplace frequency, a is the particle radius, k_B is Boltzmann's constant, T is the absolute temperature, and d is the dimensionality of the displacement vector Δr (usually $d = 2$ for video-microscopy).

In our experiments, particle positions were identified via image analysis and trajectories reconstructed with the software package IDL (Research Systems Inc.), using algorithms

developed by Crocker and co-workers [52]. The MSD was then calculated based on these trajectories, for individual particles and for the entire ensemble of tracers. Eq. 2.2 can be used to find $\tilde{G}(s)$ and calculate the complex shear modulus: $G^*(\omega) = G'(\omega) + iG''(\omega)$ by substituting $i\omega$ for the Laplace frequency s [53]. Eq. 2.2 provides the relation between MSD and dynamic moduli, but Laplace transformations are very sensitive to noise and require data over a wide range of lag times. Therefore, an alternative mathematical implementation was introduced by Mason *et al.* [25, 53], who proposed the following algebraic expansion to obtain accurate local viscoelastic properties:

$$G'(\omega) = G(\omega) \cos[\pi\beta(\omega)/2], \quad (3.1)$$

$$G''(\omega) = G(\omega) \sin[\pi\beta(\omega)/2], \quad (3.2)$$

$$\text{where } G(\omega) = \frac{k_B T}{\pi a \langle \Delta r^2(1/\omega) \rangle \Gamma[1 + \beta(\omega)]}. \quad (3.3)$$

Γ is the gamma function and $\beta(\omega)$ is a local logarithmic derivative of $\langle \Delta r^2 \rangle$ at $\tau = 1/\omega$: $\beta(\omega) = [\partial \ln \langle \Delta r^2 \rangle / \partial \ln \tau]_{\tau=1/\omega}$. This approach has the advantage of easy implementation without the need for Laplace transforms. Eqs. 3.1-3.3 also clearly identify the two dominant physical quantities that are needed to convert MSD data to dynamic moduli: the absolute MSD value $\langle \Delta r^2 \rangle$ at a given lag time τ , and the slope β in the double logarithmic plot of $\langle \Delta r^2 \rangle$ vs. τ .

The slope β is directly related to the relative magnitude of G' and G'' , respectively the storage and the loss modulus. It can easily be shown that for visco-elastic materials, β should have values between 1 (Newtonian fluids, $G'' \gg G'$) and 0 (elastic gels, $G' \gg G''$). As a result, transient microrheological experiments should not be limited to monitoring the mean-squared displacement values at a fixed lag time, but also incorporate the slope β , in order to quantify the dynamics of rheological properties. The algorithm of Eqs. 3.1-3.3 does not perform well for highly curved MSD- τ -plots. To overcome this limitation,

Dasgupta *et al.* modified the above algebraic equation empirically by including second-order derivatives of the MSD [99]. However, the higher-order derivative renders the method more sensitive to experimental noise and is therefore less suitable for small data sets with inherent statistical noise, as typically encountered during the transient analysis of individual tracer trajectories (see results and discussion).

3.2.2 EQUIPMENT

An inverted Leica DM-IRB microscope was equipped with an analog 640 x 480 pixel CCD camera (30Hz frame rate, COHU 4920, Poway, CA), which was connected to a PC. Images were transferred to the PC and recorded real-time with a precision frame grabber (PXC-200, Cyber Optics) and specialized image acquisition software (OpenBox) [51]. The spatial resolution of the imaging system with 100x oil-immersion objective was 0.099 μ m per pixel. Probe particles were premixed in the samples, so that rheological properties could be measured by carrying out particle tracking microrheology [24-26].

3.2.3 SAMPLE PREPARATION

We used two different solvent responsive hydrogel materials and induced changes in sample rheology by changing the solvent composition within a homebuilt microdialysis cell [98]. As homogeneous sample, we used a sodium alginate solution (Keltone LVCR®, ICP) [98]. A stock solution of 1.0wt% sodium alginate was initially prepared in 150mM NaCl. The stock solution was mixed well and left over night. The stock solution was diluted with 150mM NaCl to 0.25wt% of sodium alginate and carboxylate modified fluorescent polystyrene tracer particles (1.0 μ m diameter, F8819, Molecular Probes) were mixed into the sample. The sodium alginate solution forms a physical gel upon the addition of divalent cations, such as calcium ions, and the gel can be broken by adding calcium-chelating agents, such as citrate ions.

The heterogeneous sample for this study was an amphiphilic block copolypeptide (BCP) solution: K₁₆₀L₄₀ (diblock copolypeptide of 160 residues of L-lysine (K) and 40 residues

of L-leucine(L)). BCPs are known to form heterogeneous gel structures at low polypeptide concentrations [100]. A 1.0wt% stock solution of K₁₆₀L₄₀ was prepared in DI-water. The stock solution was mixed well, left over night to ensure full hydration, and diluted with DI-water and amidine-modified fluorescent polystyrene tracer particles (0.72μm diameter, Molecular Probes Co) to a final concentration prepare of 0.15wt% K₁₆₀L₄₀.

3.3 RESULTS AND DISCUSSION

3.3.1 HOMOGENEOUS MEDIA

In standard video-PTμR experiments, it is generally assumed that the rheological properties do not change during the image acquisition and that the MSDs of all particle trajectories can thus be averaged over the entire length of the movie. In transient experiments with characteristic times of the order of seconds to minutes, however, the MSDs must be determined as a function of both lag time τ and clock time t . For example, the microdialysis cell developed in our group [98], makes it possible to monitor the microstructural evolution of samples in response to changes in solvent composition. The required temporal resolution can be achieved by splitting the trajectories of particles into segments of duration Δt and calculating the MSD over the time interval from $t - \frac{1}{2}\Delta t$ to $t + \frac{1}{2}\Delta t$, averaging over all particles i in the field of view:

$$\langle \Delta r^2(\tau, t, \Delta t) \rangle = \langle \Delta r^2(\tau) \rangle_{(t-\frac{1}{2}\Delta t, t+\frac{1}{2}\Delta t)} \quad (2.3)$$

By following this strategy, we can monitor the rheological response of a sample to solvent composition changes. The interval length Δt must be chosen carefully with two primary concerns in mind: statistical validity and temporal resolution. To minimize statistical errors, Eq. (2.2) must satisfy the condition: $\Delta t \gg \tau_{\max}$, where τ_{\max} is the

maximum lag time at which the MSD is to be determined. If Δt is of the same magnitude as τ_{\max} , $\langle \Delta r^2(\tau_{\max}) \rangle$ involves significant statistical errors due to a lack of independent displacement data points within the interval Δt . On the other hand, a large value of Δt leads to poor temporal resolution and reduces the experimental ability to accurately capture physical transitions in a sample. To balance these contradictory requirements, we generally limit the range of lag times by choosing relatively small values of τ_{\max} , which is equivalent to ignoring low-frequency rheology. To ensure statistical validity, all MSD values were calculated by taking the ensemble average of at least 500 independent contributions among all particles at a particular lag time τ [24]. The large number of contributions minimized statistical noise and allowed us to employ the modified algebraic form for calculating the dynamic moduli [99]. For highly viscous or strongly elastic samples, MSD values at the shortest lag times can be very small, and sometimes even be close to the spatial detection limit, which can lead to erroneous data interpretation. In preliminary investigations (not reported here), the spatial resolution of the experimental set-up used in this study was measured by embedding particles in highly elastic gelatin gels: the minimum attainable MSD was $\sim 2 \cdot 10^{-5} \mu\text{m}^2$, which corresponds to threshold tracer displacements of 4-5 nm.

Fig. 3.1 presents the effect of Δt on the transient MSD of Ca^{2+} -induced gelation of the alginate solution. The aqueous 0.25wt.% sodium alginate solution is a Newtonian liquid in an NaCl solution, but forms a hydrogel in the presence of CaCl_2 [98]. In the experiment, a microdialysis cell was used to rapidly change the solvent composition from 150mM NaCl solution to 0.11wt.% CaCl_2 at $t = 60\text{s}$. The figure shows transient MSD values during gelation as a function of time for $\tau = 0.167\text{s}$ (5 video frames) and different lengths of the averaging interval Δt : 1-60s. All curves show a strong decrease of MSD after an initial delay, indicating the onset of gel formation after ca. 100s. For Δt above 15s, the temporal resolution of the analysis becomes too poor to accurately capture the

finer details of the MSD response, as is obvious from the gel transition and the spike of particle mobility around 200s, which marks bulk sample rearrangements. On the other hand, very short Δt intervals yield excellent temporal resolution, but introduce significant uncertainty due to lack of statistically independent data points for averaging. The appropriate trade-off between temporal resolution and statistical accuracy depends on: the characteristic time-scale of the process under investigation, the number of particles within the viewing window and the acceptable signal-to-noise level. For the case of homogenous, Ca^{2+} -induced alginate gelation, we chose $\Delta t = 15\text{s}$ to achieve an optimum balance between statistical validity and temporal resolution.

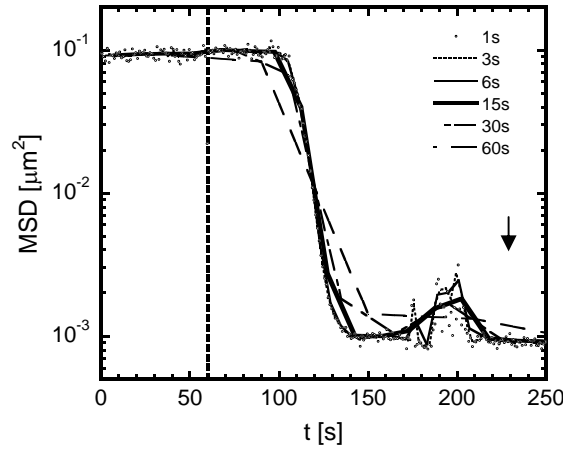


Figure 3.1 Transient MSD ($\tau = 0.167\text{s}$) for alginate gelation, analyzed with different averaging intervals Δt ; the dashed line indicates the time ($t = 60\text{s}$) at which the solvent was switched from 150mM NaCl to 0.11 wt% CaCl_2 .

3.3.2 HETEROGENEOUS MEDIA

For homogeneous media, all tracer particles probe the same local mechanical properties. Therefore, averaging the displacements of all particles within the viewing window is appropriate and yields higher statistical accuracy for determining particle mobility and mechanical properties of the medium (Eq. 2.2). However, in heterogeneous media, individual particles tend to probe different local mechanical environments [78]

and caution is needed with regards to the data analysis protocol. For instance, in porous media, the graph of tracer MSD vs. lag time τ exhibits a plateau for long lag times due to the caging of tracers within finite-size pores. From this MSD plateau value, pore sizes can be obtained. If the medium has a narrow pore size distribution, an accurate and meaningful estimate of pore size can be made directly from the ensemble averaged MSD. On the other hand, for strongly heterogeneous samples, it is preferable to first calculate the MSD of individual particles and use these data to quantify the pore size distribution, as has been done by various researchers [77, 78, 81]. In this study, the aim is to monitor the evolution of mechanical properties as a function of time. As explained in the previous section, long lag times τ cannot be used for such transient measurements, because of the desire for temporal resolution. As a result, it is impossible to monitor the evolution of pore or mesh sizes in rapidly changing samples. Instead, we have to use particle dynamics at shorter lag times to quantify microstructural dynamics of such systems. It is useful at this point to recall that microrheological properties are fully described by two characteristic parameters of the MSD: the MSD value and the slope of $\log(\text{MSD})$ versus $\log(\tau)$, as described in the Methods and Materials section.

The MSD curves of individual tracer particles are shown in Fig. 3.2a for a heterogeneous BCP hydrogel (0.15wt% K₁₆₀L₄₀ in 50mM NaCl). The heterogeneity obviously leads to a broad MSD distribution. In order to calculate transient MSD data for individual tracer particles, the minimum requirement of 500 statistically independent contributions at a particular lag time must be relaxed. The threshold used for generating Fig. 3.2a was only 5. We have to accept the fact that this choice leads to statistical uncertainty, in particular for short tracer trajectories that generally represent the faster moving particles. Because of their mobility, these tracers remain in the viewing window for shorter durations. After the selection of valid tracer trajectories, the MSD data of individual tracers shown in Fig. 3.2a can be compared.

For the calculation of rheological properties from individual MSD curves, we used Eq.(3.1-3) instead of the modified algebraic form. Although the latter could be applied successfully to the homogeneous alginate solution, the noisy MSD curves in Fig. 3.2a prohibit its use for the heterogeneous sample. In order to use Eq.(3.3), we must extract both slopes and MSD values from the MSD curves at each lag time. The local slopes of the individual MSD curves were determined by applying a linear least-square fit method to the double logarithmic plot between $\tau = 0.10$ - 0.20 s (3-6 video frames; the shaded region in Fig 3.2a). As described in the previous section, we must choose τ_{max} much smaller than Δt to increase the number of independent contributions. In this study, we chose $\Delta t = 15$ s (450 video frames), and $\tau_{max}=0.20$ s (6 video frames). With these analysis settings, we created histograms of MSD values and slopes of individual particles at a particular clock time. Figs. 3.2b and c show examples of MSD and slope histograms for the heterogeneous BCP hydrogel. The results for the homogeneous sodium alginate solution described in the previous section have been added for comparison. It can be seen that both histograms exhibit single narrow peaks for the homogeneous alginate sample, while the distributions are much broader for the heterogeneous sample and multiple peaks were observed (see also [82, 94]). Although the slope of $\log(\text{MSD})$ vs $\log(\tau)$ should be between 0 (elastic gel) and 1 (viscous liquid), statistical uncertainty leads to a few cases with values outside these fundamental limits, especially for the heterogeneous sample. The histograms emphasize that in order to analyze heterogeneous samples, it is important to monitor not only the average MSD values and slope, but also their distribution.

The data in Fig. 3.2a-c represent the particle dynamics for a single time interval of 15s. In order to study the dynamics of the heterogeneous BCP sample, we must add the clock time t as an extra variable. The resulting three-dimensional histograms of MSD values and slopes are presented as contour plots in Fig. 3.2d and e. The vertical lines in

the plots mark the transitions in solvent composition (DI water \rightarrow NaCl solution \rightarrow DI water). In Fig. 3.2d, the distribution of MSD values dramatically broadened after the addition of salt, and retightened after salt removal. The response upon addition of salt was also found to be much faster than the recovery after salt removal. In Fig. 3.2e, with the addition of salt, the slope distribution also became very wide, which is evidence for an increased heterogeneity; some tracer particles probe elastic regions (slope equals 0), while others probe liquid-like regions (slope is 1). After salt removal, the slope distribution slowly became narrower and the center of the distribution decreased below the initial level, which indicates that the sample became more elastic after completion of a full dialysis cycle (DI-water \rightarrow 50mM NaCl \rightarrow DI-water). The experiment shows that monitoring transient distribution of MSD values and slopes is useful for understanding the microstructural dynamics of heterogeneous samples.

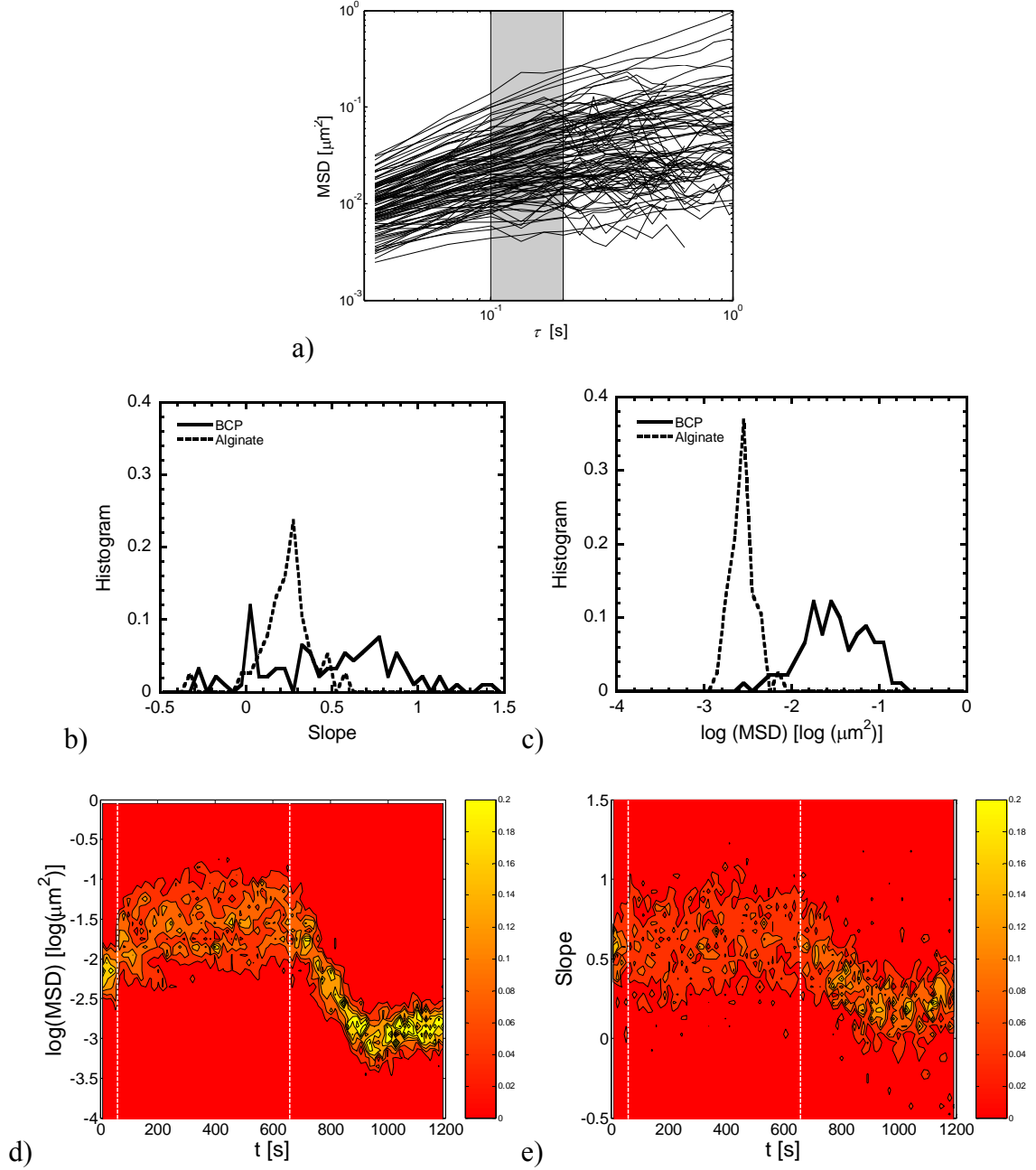


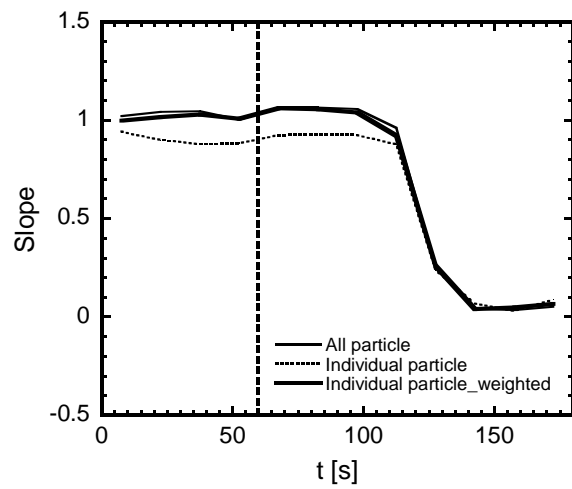
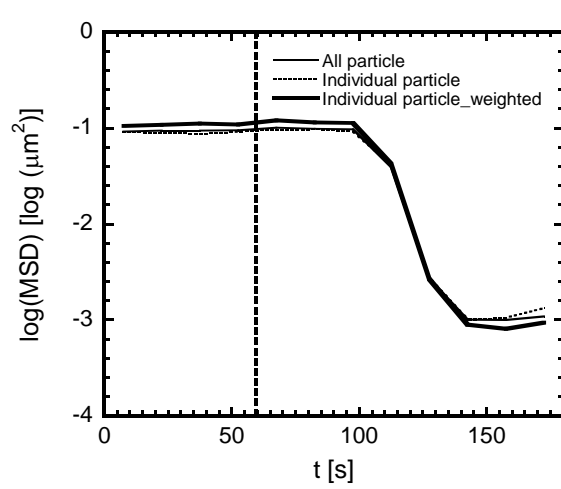
Figure 3.2 a) MSD vs. τ curves for individual tracers after 9 min dialysis against 50mM NaCl, averaged over time interval $\Delta t = 15$ s. Histograms of b) MSD values and c) slopes of $\log(\text{MSD})$ vs $\log(\tau)$ for heterogeneous BCP hydrogel in 50mM NaCl solution (solid line; data from a) and for homogeneous sodium alginate after dialysis against CaCl_2 (dotted line; data from Fig. 3.1 at $t = 120$ s). Contour plots of transient distribution of d) MSD values ($\tau = 0.167$ s) and e) slope ($t = 0.10 - 0.20$ s) for BCP sample during dialysis experiments; solvent is switched from DI water to 50mM NaCl at $t = 60$ s and back to DI water at $t = 660$ s.

Before further analyzing the data from Fig. 3.2 and quantifying rheological properties and heterogeneity, we need to prove the validity of the analysis based on individual trajectories. Previously, we confirmed that the ensemble-averaged MSD based on all particles gave results that were in excellent agreement with bulk rheology measurements for homogeneous samples, *e.g.* sodium alginate solution and sodium polystyrene sulfonate solutions [98]. Therefore, we consider the results from the all particle analysis a benchmark. For both samples, heterogeneous and homogeneous, we calculated the average MSD value and slope for $\tau = 0.167\text{s}$ as a function of time via two different methods: 1) directly from the ensemble averaged MSD (all particle method) 2) as the average of the distribution of MSD values and slopes of individual particles (individual particle method). For the homogeneous sodium alginate sample (Fig. 3.3a-b), the MSD and slope were in reasonable agreement, although some deviations in the slope were observed. The heterogeneous BCP gel (Fig. 3.3c-d) showed a similar picture, with deviations between the individual trajectory analysis and ensemble averaging being most prominent for the slope. The peak at 60s is an artifact caused by vibrations due to touching the microscope stage during solvent switching. One of the possible reasons for the deviation is that the individual particle method lends equal weight to all trajectories, regardless of their length. If anomalous trajectories are detected, these tend to be short. In the all particle method, the contributions from such short trajectories do not have a significant effect on the ensemble-averaged MSD. In order to compensate for this effect, we introduce a third, weighted individual particle method, in which the length of a trajectory, n (in number of frames), is used as weighing factor when calculating the average MSD value and slope from the distribution:

$$\langle \Delta r^2 \rangle = \frac{\sum_i n_i \langle \Delta r^2 \rangle_i}{\sum_i n_i} \quad \text{and} \quad \beta(\omega) = \frac{\sum_i n_i \beta(\omega)_i}{\sum_i n_i}. \quad (3.4)$$

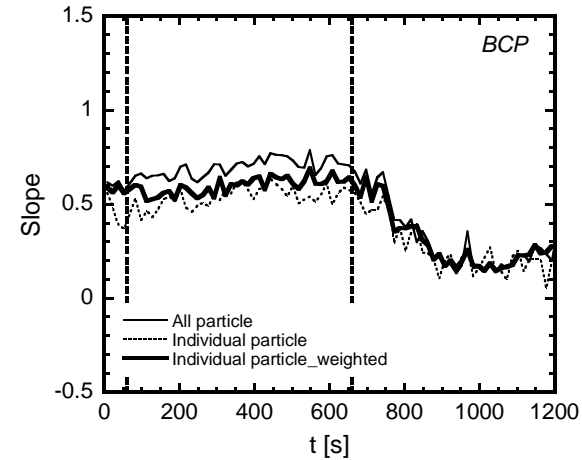
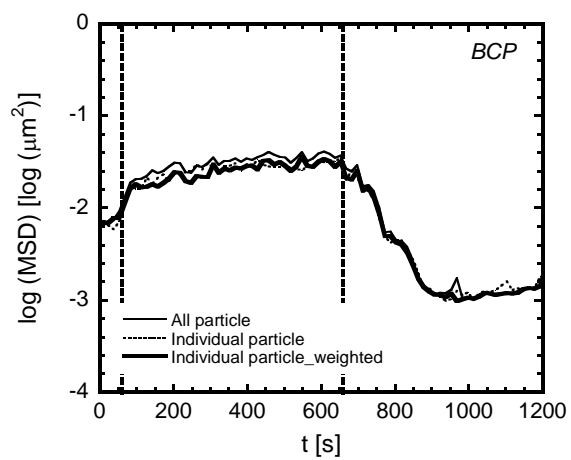
where subscript i denotes the trajectory ID, and n_i represents the length of trajectory i (in number of frames). For the alginate solution, the weighted individual particle method closely agreed with the results with the all particle analysis method (Fig. 3.3a-b), thus confirming the validity of the weighted average.

For heterogeneous media, the definition of an average MSD value is more complicated, because there is no obvious correct approach. The individual particle analysis provides the opportunity to study heterogeneity and is thus preferable over the ensemble average. We argue that the appropriate average MSD for a heterogeneous sample should capture the distribution of particle mobilities that are observed visually in the movie. One of the issues with strongly heterogeneous samples is that a wide variation in tracer mobility results in equally wide distributions of particle residence time in the field of view. For instance, a single fast moving particle might generate multiple independent trajectories by moving in and out of the focal plane. The weighing factor n introduced in Eq. 3.4 compensates for this effect. As can be seen in Fig. 3.3c-d, the weighted individual particle analysis deviates from the other two methods, particularly with regards to the slope. However, since there is no true solution, no significant conclusions can be drawn from the deviations, other than that we are convinced that the weighing captures the sample properties best. When the difference between the MSD values from the ensemble averaged all particle analysis and the weighted individual particle analysis are normalized and plotted as a function of time (Fig. 3.3e), an interesting observation can be made. After the addition of salt, which is known to increase heterogeneity, the normalized difference increased significantly as well; after salt removal the difference became more negligible. This quantity seems to closely track sample heterogeneity and thus, application of both the all particle analysis and weighted individual particle analysis could provide valuable insight into the evolution of heterogeneous microstructures.



a)

b)



c)

d)

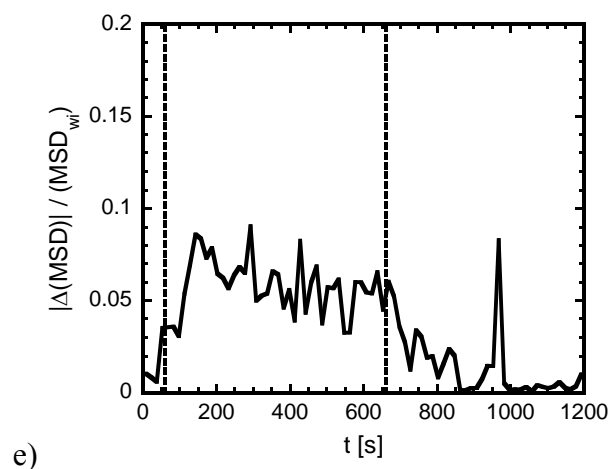


Figure 3.3 Transient average MSD and slope values ($\tau = 0.167\text{s}$) as calculated with three different averaging methods: all particle analysis (thin solid), individual particle analysis (dotted), and weighted individual analysis (thick solid). a) average MSD values and b) slope for homogeneous sodium alginate sample, c) average MSD values and d) slope for heterogeneous BCP sample (0.15wt% $\text{K}_{160}\text{L}_{40}$), e) the normalized MSD difference between all particle analysis, (MSD_a), and weighted individual particle analysis (MSD_{wi}) for the heterogeneous BCP sample (data from c).

After settling on an appropriate analysis method, we needed to confirm the selection of Δt for the heterogeneous case, as was done for the homogeneous sample (Fig. 3.1). As Δt decreased, the apparent MSD response became gradually faster and converged (Fig. 3.4a); for Δt below 6s, the MSD curve became noisy due to poor statistics. Fig. 3.4b quantifies the number of individual particle trajectories that were needed to achieve a meaningful average. With $\Delta t \geq 15$ s, no significant noise was observed and the total number of trajectories was above 100. Considering the threshold of at least 5 displacement contributions per trajectory, this equivalent to a total number of independent contributions to the average of at least 500, which has been an accepted threshold for homogeneous samples [24]. Thus, we could apply the same analysis parameters, $\Delta t=15$ s and $\tau_{max}=6$, as for the homogeneous case to achieve high temporal resolution and statistical validity. In our experiments, the average number of particles identified in every image was 20. In general, the transient analysis settings conditions must be reevaluated and optimized depending on samples properties and tracer particle density.

3.3.3 TRANSIENT HETEROGENEITY

To quantify the heterogeneity, a non-Gaussian parameter, has been introduced [101, 102]:

$$\alpha(\tau) = \frac{\langle \Delta x^4(\tau) \rangle}{3 \langle \Delta x^2(\tau) \rangle^2} - 1. \quad (3.5)$$

The parameter uses the displacement statistics of all tracer trajectories and quantifies the deviations of the displacement distribution (van Hove correlation function) from a Gaussian curve. For homogeneous media, the van Hove correlation function is Gaussian, whereas it largely deviates from a Gaussian distribution for heterogeneous media. For transient analysis, it is necessary to monitor the evolution of α as a function of time:

$$\alpha(\tau, t) = \frac{\langle \Delta r^4(\tau) \rangle_{(t-\frac{1}{2}\Delta t, t+\frac{1}{2}\Delta t)}}{3\langle \Delta r^2(\tau) \rangle_{(t-\frac{1}{2}\Delta t, t+\frac{1}{2}\Delta t)}^2} - 1 \quad (3.6)$$

For a perfect homogeneous case, $\alpha(\tau, t)$ equals zero and its value increases as deviations from the Gaussian distribution become stronger. In this study, we fixed τ at 0.33s. The transient $\alpha(t)$ for the BCP hydrogel in the microdialysis is shown in Fig. 3.4c for different averaging interval lengths Δt . A large spike appeared at 60s, which is caused by vibrations due to switching the solvent. For Δt below 6s, the curve becomes noisy as a result of poor statistics. The noise significantly decreases for $\Delta t \geq 30$ s. However, for such long intervals, the temporal resolution becomes insufficient to capture sample dynamics (see peak around 800s). Moreover, long averaging intervals can even generate artificial spikes in α during rapid microrheological transitions of homogeneous samples, because tracer trajectories in distinctly different environments (for example, before and after gelation) contribute to the van Hove correlation function. Thus, again, we chose $\Delta t = 15$ s. When the number of independent data points to the ensemble average is analyzed (Fig. 3.4d), it can be concluded that at least 10^4 independent contributions are required for statistically relevant α values [24]. When we focus our attention on the curve with $\Delta t = 15$ s, it is noteworthy that the curve closely tracks previous, qualitative observations of sample heterogeneity (Fig. 3.2c-d and 3.3e). The non-Gaussian parameter is obviously useful method to quantify the heterogeneity. However, because it is an average parameter, details about sample heterogeneity are lost during the calculation of $\alpha(\tau, t)$. For example, the parameter does not distinguish between samples with a broad distribution of tracer environments and samples with several distinct peaks in the displacement distribution, in which case, classification of particles into different clusters might be preferred [78, 82]. In conclusion, for the characterization of strongly heterogeneous media, we still need to investigate distributions of individual trajectory properties in addition to the non-Gaussian parameter α .

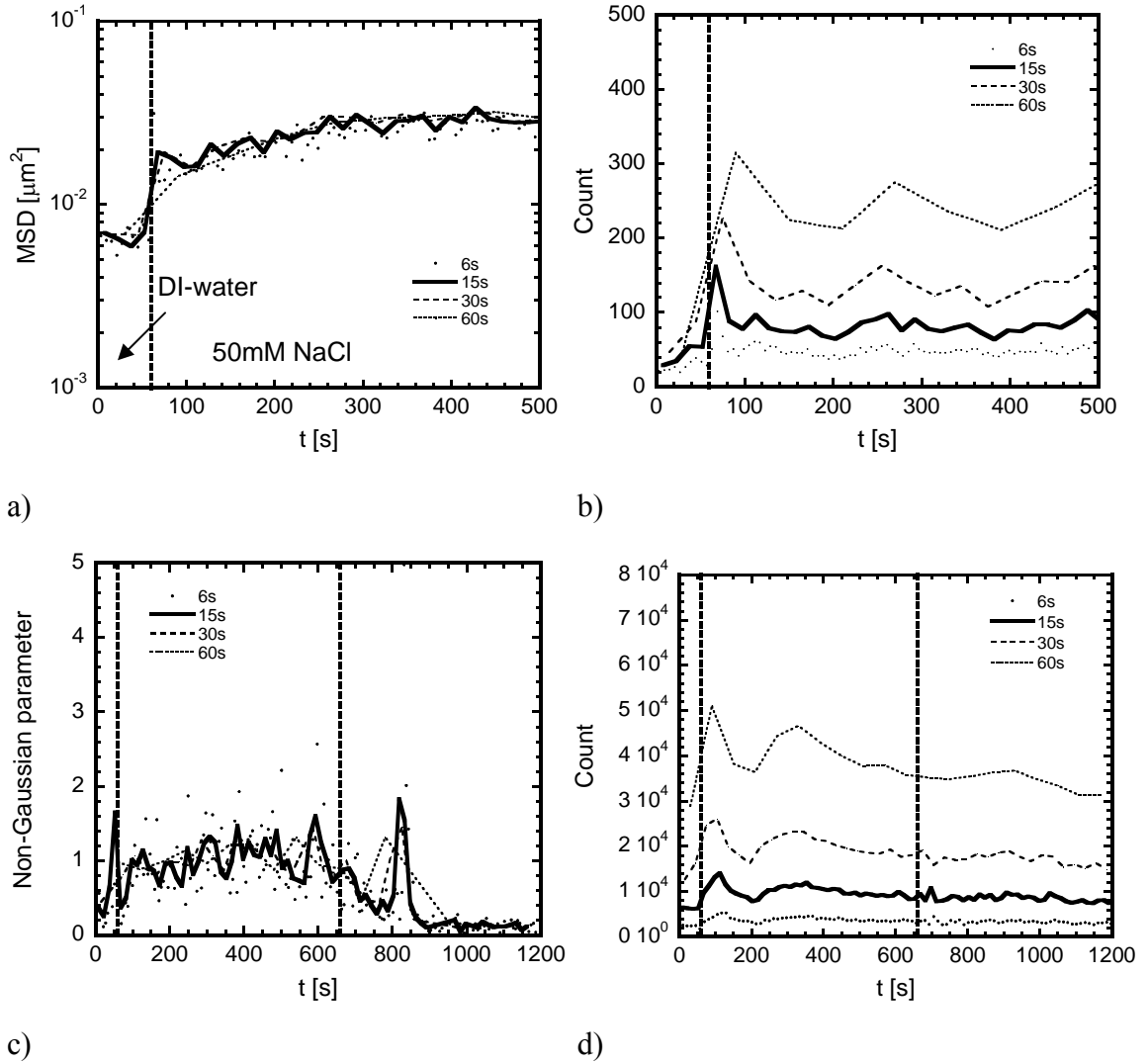


Figure 3.4 The effect of choice of Δt on a) the average MSD value ($\tau = 0.167\text{s}$) for heterogeneous BCP sample (0.15wt% $\text{K}_{160}\text{L}_{40}$) and b) the number of particle trajectories that constitute the average. c) Transient non-Gaussian parameter, $\alpha(0.33\text{s})$, of heterogeneous hydrogels with different Δt s and d) the number of displacements used to generate the Van Hove diagrams. The solvent was switched from DI-water to 50mM NaCl at 60s, and 50mM NaCl to DI-water at 660s.

3.3.4 TRANSIENT COMPLEX MODULUS

The ultimate goal of transient PTuR is to provide quantitative rheological data, i.e. transient dynamic moduli $G'(\omega)$ and $G''(\omega)$. Eqs. (3.1-3) provide the means to calculate $G'_i(\omega)$ and $G''_i(\omega)$ of individual particles by using the MSD values and slopes for individual particle trajectories. The observed distributions of MSD values, $\langle \Delta r^2(1/\omega) \rangle$, and slopes, $\beta(\omega)$, generate a very wide distribution of $G(\omega)$. Particle trajectories that resulted in physically unacceptable slope values $\beta(\omega)$ less than -1 due to statistical noise, were eliminated upon calculating the gamma function, because the gamma function is undefined for β values smaller than -1. In spite of this preselection, negative values of $G'_i(\omega)$ and $G''_i(\omega)$ were found for some trajectories, depending on $\beta(\omega)$ in Eq. (3.1, 3.2). These data were not ignored since they represent the inherent experimental noise.

Again, we compared three methods for calculating the average moduli, analogous to the determination of the average MSD: all particle analysis, individual particle analysis, and weighted individual particle analysis. For the all particle analysis, we substituted the ensemble averaged transient MSD and slope results (Fig. 3.3c-d) into Eq. (3.3) to determine the dynamic moduli. The individual particle analysis simply determines the mathematical average of all individual moduli $G'_i(\omega)$ and $G''_i(\omega)$, while the weighted individual analysis employs the same weighing function as used for the MSD and slope in Eq. (3.4):

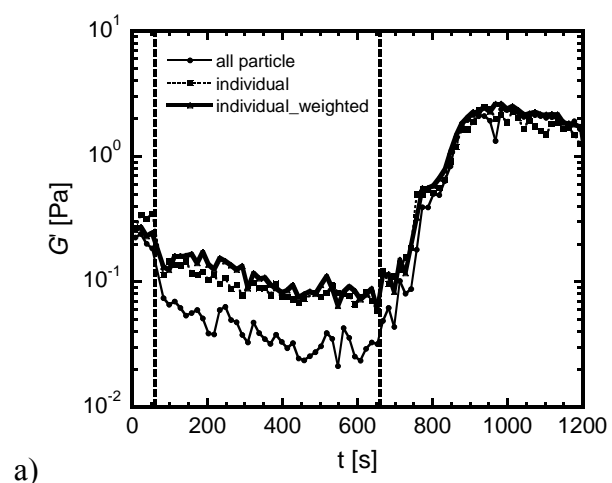
$$G' = \frac{\sum_i n_i G'_i}{\sum_i n_i} \text{ and } G'' = \frac{\sum_i n_i G''_i}{\sum_i n_i} \quad (3.7)$$

The moduli obtained with all three methods are presented in Fig. 5 for $\omega = 6$ rad/s and the graph shows that all three averaging methods yield similar microrheological dynamics.

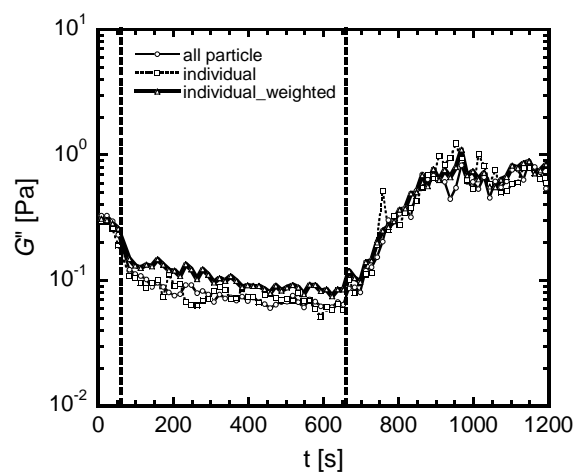
The transient moduli G' and G'' from weighted and non-weighted individual trajectory analysis are close to each other. The all particle analysis results in similar values for the loss modulus, but a noticeably lower loss modulus after the addition of salt, when the system is most heterogeneous regime ($t = 60\sim 660$ s). This result is directly related to the higher slopes that were found for the same sample (Fig. 3.3d). The spikes at 60s and 660s are again the result of small sample motion that is induced by touching the microscope during solvent switching.

In order to check the effect of the algorithm of Eqs. 3.1-3, we also performed a pseudo-steady-state analysis for the last 50s of each solvent step. The ensemble averaged (all particle) MSD was determined and we could apply the modified algebraic form of Dasgupta *et al.* [99], because of the larger amount of available data. The results (not shown here) were in excellent agreement with the transient all particle analysis in Fig. 3.5, which proved that the variability between analysis methods (Fig. 3.5) does not originate from the use of approximated forms of the GSE equation or statistical uncertainty. The microrheological moduli of the 0.15 wt.% K₁₆₀L₄₀ gels in DI water are in good agreement with previously published macrorheological properties measured with a rheometer [100]; unfortunately, the variation of moduli calculated with the three microrheological analysis methods is fairly small and does not allow for strong conclusions about their respective validities for heterogeneous samples. Moreover, it is impossible to perform macrorheological measurements for direct comparison on the samples with added salt, the regime where the moduli variations in Fig. 3.5 are most pronounced. Work in our group has shown that convective mixing during the preparation of BCP gels with added salt for microrheology affects the microstructure. As a result, direct comparison with data from the microdialysis cell in which salt transport occurs via diffusion is impossible (see Chapter 4). Nevertheless, the data in Fig. 3.5 underline that it is possible to measure transient dynamic moduli with PT μ R. The preferred analysis

method is the one that calculates moduli for each individual trajectory before determining the weighted average.



a)



b)

Figure 3.5 Transient dynamic moduli, a) G' (solid) and b) G'' (open), of 0.15wt. % $K_{160}L_{40}$ hydrogels analyzed with three different methods: all particle analysis (thin solid), individual particle analysis (dotted), and weighted individual particle analysis (thick solid). Solvent manipulation scheme during the experiment: DI-water (60s) \rightarrow 50mM NaCl (600s) \rightarrow DI-water (540s).

3.4 CONCLUSIONS

We have investigated the use of video-PT μ R for monitoring dynamic changes of the local mechanical properties of solvent-responsive, homogeneous and heterogeneous hydrogels. The challenge of such studies is to extract accurate rheological quantities from limited data sets of tracer trajectories. This paper provides guidelines for the optimum analysis parameters for such transient experiments, which requires trade-offs between temporal resolution and statistical validity.

Additional complications arise for heterogeneous samples, in which case ensemble averaging over all available tracer particles is not appropriate. We have presented novel methodology to present the key microrheological parameters, the value and local slope in a double logarithmic of $\log(\text{MSD})$ vs $\log(\tau)$, in transient histograms. This data representation provides immediate qualitative insight into the average microrheological properties, as well as the spatial heterogeneity. For comparison with macrorheological data, it is important to translate the results into meaningful average rheological quantities. We have compared three different methods for averaging mean-squared displacement data: 1) the ensemble averaged MSD of all displacements of all particles (all particle method), 2) the average of the distribution of MSD values of individual tracer trajectories (individual particle method), and 3) the weighted average of the distribution of MSD values of individual tracer trajectories to account for variations in trajectory length (weighted individual particle method). Although the ensemble average works well for homogeneous samples and results in higher statistical accuracy, the weighted individual particle most accurately describes the microstructural evolution of heterogeneous samples. It was also found that the difference between the all particle MSD and the weighted individual particle MSD can be used as an indicator of sample heterogeneity. Close agreement was found between the evolution of this parameter and a

more commonly used non-Gaussian parameter, which compares the histogram of all displacements with a Gaussian distribution.

Finally, we discussed algorithms to obtain transient dynamic moduli, G' and G'' , for heterogeneous samples and proposed the calculation of these quantities for individual tracer trajectories before determining the weighted average of this distribution. The study resulted in the first report of transient dynamic moduli for heterogeneous samples as measured with particle tracking microrheology. Although the experimental study was limited to a homogeneous alginate gel and heterogeneous block copolypeptide gel, the results are applicable to a wide variety of complex fluids undergoing microstructural rearrangements.

CHAPTER 4

MICROSTRUCTURAL EVOLUTION OF SALT-RESPONSIVE GELS UNDERGOING DIFFUSIVE SOLVENT EXCHANGE ³

4.1 INTRODUCTION

A challenge in designing hydrogels with well-defined responsiveness to external environmental stimuli is to quantify their microstructure under conditions that mimic *in vivo* environments, in which mass transport of solvent components is dominated by diffusion. In contrast, *in vitro* sample preparation for characterization typically involves active, convective mixing. To overcome this discrepancy, the microdialysis cell is a suitable instrument, which enables us to qualitatively and quantitatively monitor the microstructure and local mechanical properties during diffusive solvent exchange. In this chapter, we employed the microdialysis cell to study the microstructural evolution of synthetic self-assembled block copolypeptide (BCP) hydrogels via microrheology and confocal microscopy [98].

Synthetic, amphiphilic block copolypeptides (BCPs) can be designed to self-assemble into porous hydrogels [103]. The synthesis methods of these biomimetic materials facilitate manipulation of molecular architecture: molecular weight, amino acid composition, and number and lengths of blocks [104]. In previous work, this design space was explored to elucidate the mechanism that is responsible for the observed low gelation concentrations [100]. It was found that self-assembly into fibrillar structures

³ The contents of this chapter have been submitted for publication:
Sato, J., Nowak, A.P., Deming, T.J., and Breedveld, V. "Microstructural evolution of self-assembled stimuli-responsive hydrogels".

originates from a subtle balance of repulsive forces between charged hydrophilic blocks and attractive forces between hydrophobic blocks [103], in which secondary structure plays a major role. The mechanical properties of the resulting gels strongly depend on molecular architecture. This tunability, the porosity of the hydrogels, and their rapid recovery after breakdown under external shear stress [100], make them excellent candidates for tissue engineering and drug delivery [105]. For such applications, however, the microstructural response to changes in environmental conditions is highly relevant, since gel strength and porosity are key properties for manipulating molecular diffusion and cell proliferation.

The morphology and mechanical properties of BCP gels strongly depend on pH and ionic strength, two important physiological parameters [100, 105-108]. The presence of salt shifts the intermolecular force balance by screening polyelectrolyte charges and can either strengthen or weaken the self-assembled BCP hydrogels, depending on molecular architecture, as was measured macroscopically with a rheometer [109]. However, steady-state macroscopic rheometry provides only limited insight into the microstructure and the dynamics of its evolution. Here, we present an experimental performed with a recently developed dialysis cell for microscopy [98]. The microfluidic device enables rapid solvent manipulation inside a hydrogel sample and simultaneous optical observation of the microstructure and local rheology with a high-resolution microscope. The dialysis cell closely mimics *in vivo* solvent transport in tissue and artificial biomaterials, which is generally governed by diffusion. Unfortunately, most sample preparation protocols for *in vitro* characterization require convective mixing after the addition of salt or pH buffer. The resulting shear stress can affect the microstructure and strength of the hydrogels, thus leading to incorrect interpretations of the responsiveness to environmental stimuli. The dialysis cell relies purely on diffusive mass transport without external shear stress and can thus provide unique insight into the microstructural evolution of stimuli-responsive hydrogels. In addition, the device permits

complex multi-step solvent exchanges, including the removal of ions, which would be impossible with traditional add-and-mix protocols. The results provide guidance for the design of new responsive biomaterials with optimized *in vitro* performance.

4.2 METHODS AND MATERIALS

4.2.1 EQUIPMENT AND MICRORHEOLOGY

The dialysis cell consists of a reservoir, porous membrane, and sample chamber. Small solvent and solute molecules can freely diffuse into the sample chamber through the semi-permeable membrane while macromolecular sample components are trapped in a sample chamber. The solvent composition in the chamber can be quickly manipulated via diffusion due to the small dimensions of the device (\sim a few minutes) [98]. After loading a sample into dialysis cell, the sample chamber is tightly sealed with nail polish and molten polymer. Macroscopically mixed samples were vigorously homogenized on a vortex mixer. Samples were rested overnight, before loading into a simple sample chamber (microscope slide, coverslip and paraffin film spacers) and tightly sealing with vacuum grease.

An inverted microscope (Leica DM-IRB, 100x oil immersion lense) was equipped with an analog 640 x 480 pixel CCD video camera (30Hz frame rate, Cohu 4920), and movies were recorded in real-time with a precision frame grabber (PXC-200, Cyber Optics) and specialized image acquisition software (OpenBox [51]) as described elsewhere [98]. MSDs were calculated from particle trajectories as a function of time [24-26] with the software package IDL (Research Systems Inc.), using algorithms developed by Crocker and co-workers [52]. The dynamic moduli, G' and G'' , were calculated as a function of angular frequency via the generalized Stokes-Einstein relation. Transient PT μ R was performed by cutting the initial particle trajectories into segments of

duration Δt and calculating MSD for the time interval from $t - \frac{1}{2}\Delta t$ to $t + \frac{1}{2}\Delta t$ (see Eq.(2.2)).

To evaluate the heterogeneity of samples, we used a non-Gaussian parameter, which quantifies the level of deviation from a Gaussian displacement distribution by comparing the fourth and second moment of the distribution [101] (see Eq. (3.5). For a perfect Gaussian distribution, $\alpha(\tau)$ is 0.

4.2.2 SAMPLE PREPARATION

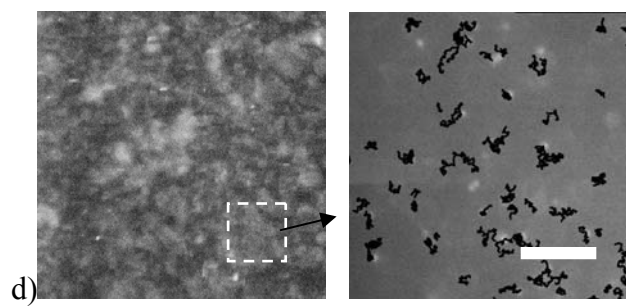
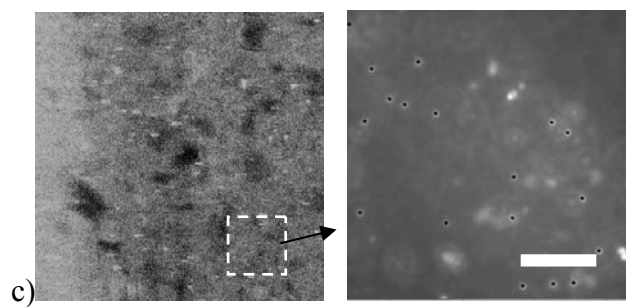
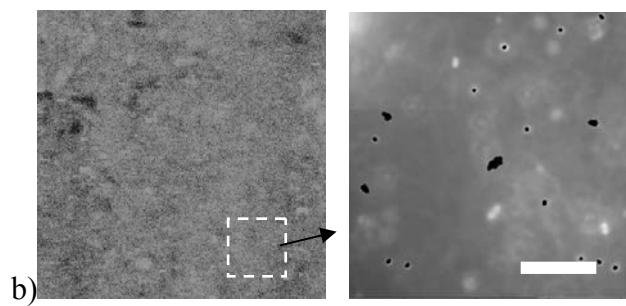
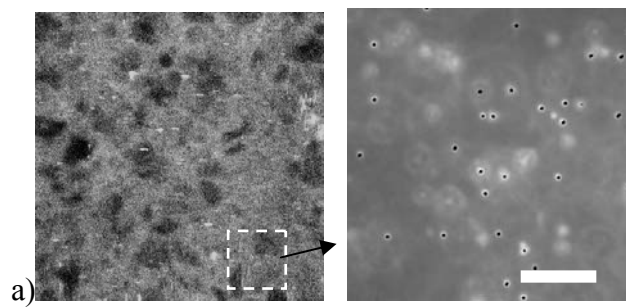
Initially, 1.0wt% K₁₆₀L₄₀ and 4.0wt% K₁₈₀L₂₀ hydrogels were prepared in DI-water as stock solutions, vigorously mixing the BCP powder with the water, and letting the sample rest for at least a few days to fully hydrate. We diluted the stock solution to the desired concentration with DI-water and suspensions of amidine modified fluorescent polystyrene tracer particles (Molecular Probes Co). After dilution, the sample was rested overnight.

4.2.3 LASER SCANNING CONFOCAL MICROSCOPY (LSCM)

For hydrogel imaging with LSCM (VT-eye, VisiTech International), lipophilic fluorescent dye (DiOC18, Molecular Probes) was dissolved in THF to saturation (micromolar range). Then, a small quantity of the dye solution (several μ l) was added to the hydrogel [110]. The dye exhibits fluorescence in hydrophobic environments and little fluorescence in the water phase. For transient LSCM, a slow shutter speed was used to avoid excessive photobleaching (0.17sec exposure time, image every 30seconds, 20x oil immersion lens).

For most of the experiments in this study, hydrogels of K₁₆₀L₄₀ (diblock copolypeptide of 160 residues of L-lysine (K) and 40 residues of L-leucine(L)) in DI-water were used. Aqueous solutions were prepared at 0.25wt.% K₁₆₀L₄₀, slightly above the critical gelation point as measured with a mechanical rheometer.[100] A hydrophobic

fluorescent dye (DiOC18) was used to stain hydrophobic domains, so that the microstructure of the gels could be visualized inside the dialysis cell with laser-scanning confocal microscopy (LSCM) [100, 110]. Local mechanical properties were also measured with particle-tracking microrheology (PT μ R) [25, 26, 52]. Figs. 4.1a-c show the structure before and after two step-wise changes in solvent composition: DI-water \rightarrow 50mM NaCl \rightarrow DI-water. Initially, in DI water, LSCM revealed a highly porous structure (Fig. 4.1a; see also [100]). The trajectories of positively charged polystyrene tracer particles (0.72 μ m diameter) exhibit strong elasticity (Fig. 4.1e), indicating that the particles were trapped within the gel network that surrounds the large aqueous pores. Control experiments with PEGylated particles [70] yielded the same result, proving that the particle dynamics was not affected by interactions between the tracer particles and the gel network [111]. The introduction of 50mM NaCl solution leads to a gradual disappearance of the porous structure, and after 10min the sample looked much more homogeneous (Fig. 4.1b). However, the particle trajectories revealed a surprisingly heterogeneous microstructure, in which some tracers diffused freely, while others were strongly restricted by a highly elastic environment. These structural changes are caused by the local deswelling of the gel network upon the addition of salt. After 10min dialysis against DI-water to remove the salt, the initial structure recovered and particle trajectories showed strongly elastic behavior (Fig. 4.1c). The dynamics can be observed in more detail in a movie of the LSCM experiment (see snapshots of entire experiment in Fig. 4.2). When macroscopic mixing was used after the addition of 50mM NaCl instead of dialysis, the observed microstructure was significantly different (Fig. 4.1d vs. 4.1b): the gel was broken into small fragments. The probe particles freely diffused with the gel fragments and the sample appeared liquid-like with PT μ R, only marginally more viscous than DI water (Fig. 4.1d and 4.1e). The microrheology of this macroscopically mixed sample did not change over the course of several days.



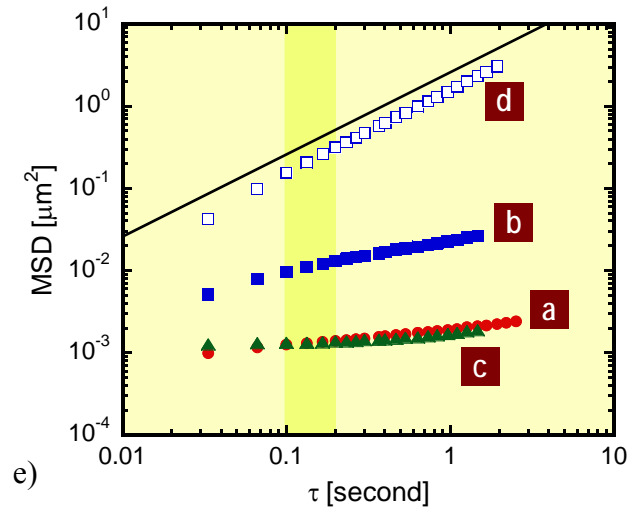
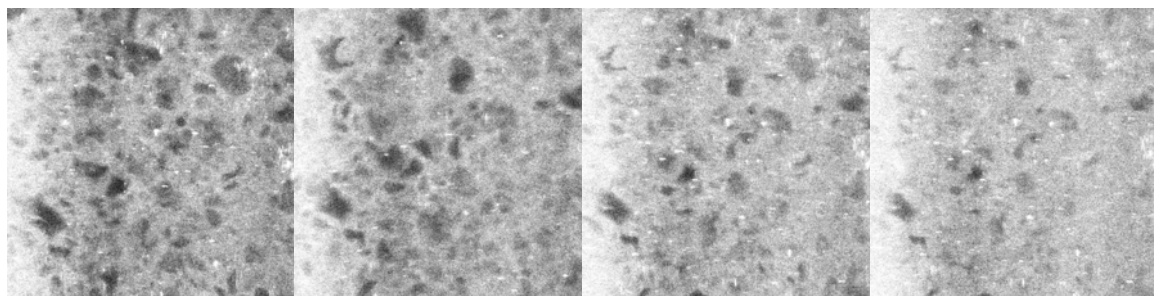


Figure 4.1 LSCM and PTμR. a) in DI-water before dialysis, b) in 50mM NaCl after 10min dialysis, c) in DI-water after salt removal, and d) in 50mM NaCl with macroscopic mixing. Viewing area of LSCM is $200 \times 200\mu\text{m}$, while PTμR images with trajectory overlays are $40 \times 40\mu\text{m}$. e) steady state mean-squared displacements for a)-d); solid line represents MSD of particles in DI-water and the shaded region marks the lag times that were used for transient PTμR in Fig. 4.2.

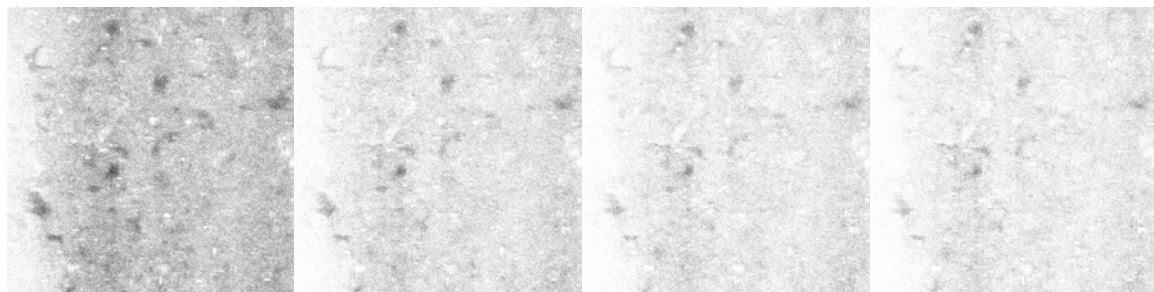


0min

1min

2min

3min

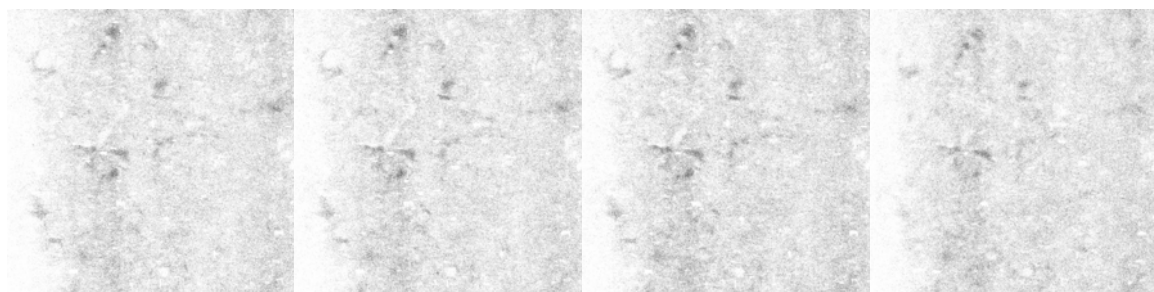


4min

5min

6min

7min



8min

9min

10min

11min

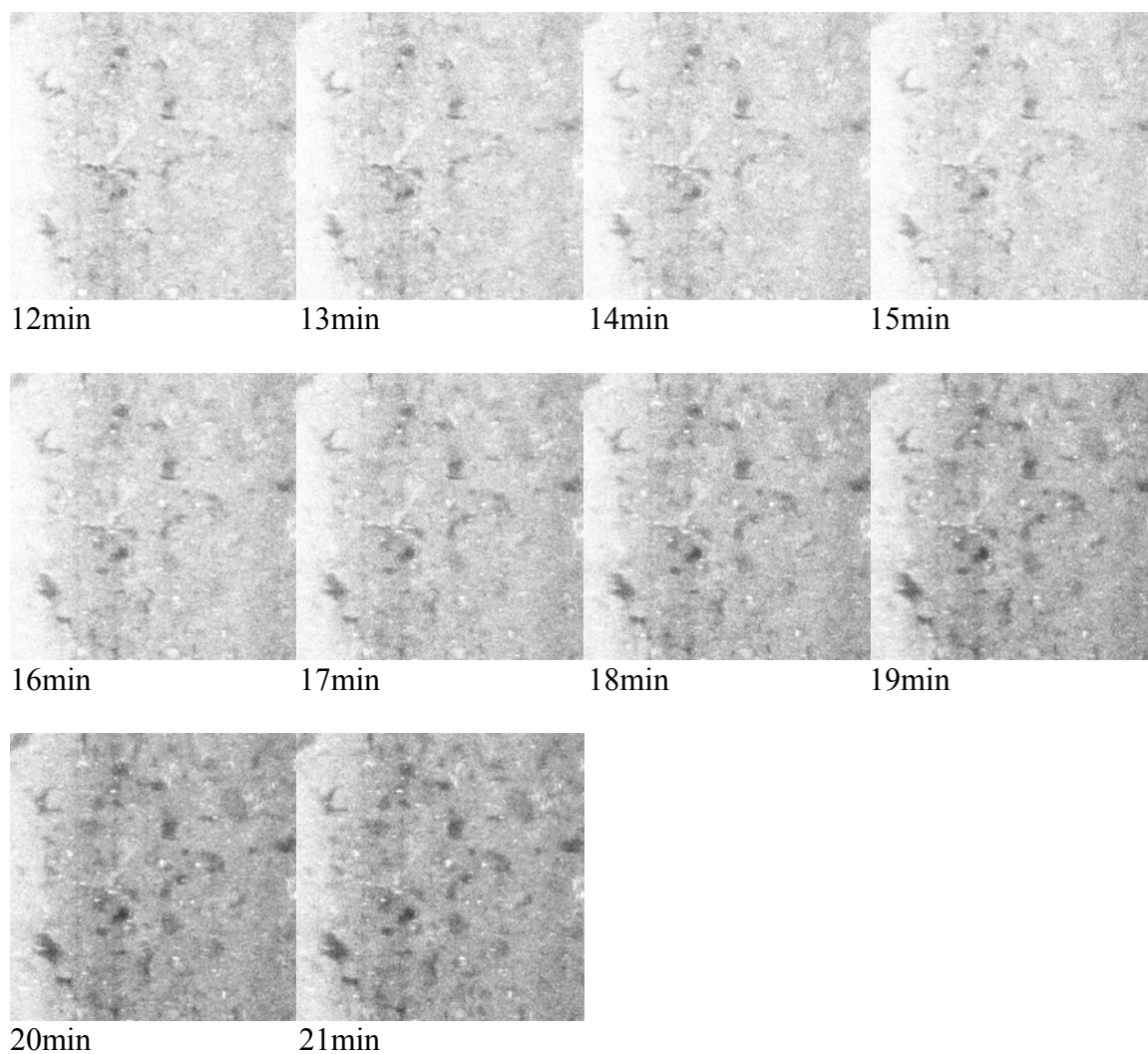


Figure 4.2 Snapshots of a transient confocal experiment; solvent is switched from DI water to 50mM NaCl at $t = 1\text{min}$ and back to DI water at $t = 11\text{min}$. $\text{K}_{160}\text{L}_{40}$ 0.25wt.% with 50mM NaCl. Viewing area is $55\mu\text{m} \times 55\mu\text{m}$.

4.3 RESULTS AND DISCUSSION

Figure 4.1 only provides snapshots of the gel microstructure, but the dialysis cell enables continuous monitoring of sample microrheology (transient PT μ R [98]) during the solvent exchange process. The mean squared displacement (MSD), $\langle \Delta x^2 \rangle_i$ of individual particle trajectories were used to create histograms of the MSD distribution as a function of time [78, 94] (see contour plot in Fig. 4.3a). A non-Gaussian parameter, $\alpha = \langle \Delta x^4 \rangle / 3 \langle \Delta x^2 \rangle^2 - 1$ (Eq. (3.5)), was used to evaluate gel heterogeneity (insets Fig. 4.3) [101]. For homogeneous media, the MSD distribution is expected to be Gaussian ($\alpha = 0$), while heterogeneity leads to non-Gaussian MSD distributions and an increase of α . While the 0.25wt.% K₁₆₀L₄₀ hydrogel in DI water is homogeneous ($\alpha \cong 0$), the diffusive addition of 50mM NaCl resulted in a significant increase of both the MSD, $\langle \Delta x^2 \rangle_{\tau=0.1}$, and α (Fig. 4.3a), which means that the hydrogel became weaker and more heterogeneous. After removal of salt via dialysis, the gel regained its strength and homogeneity.

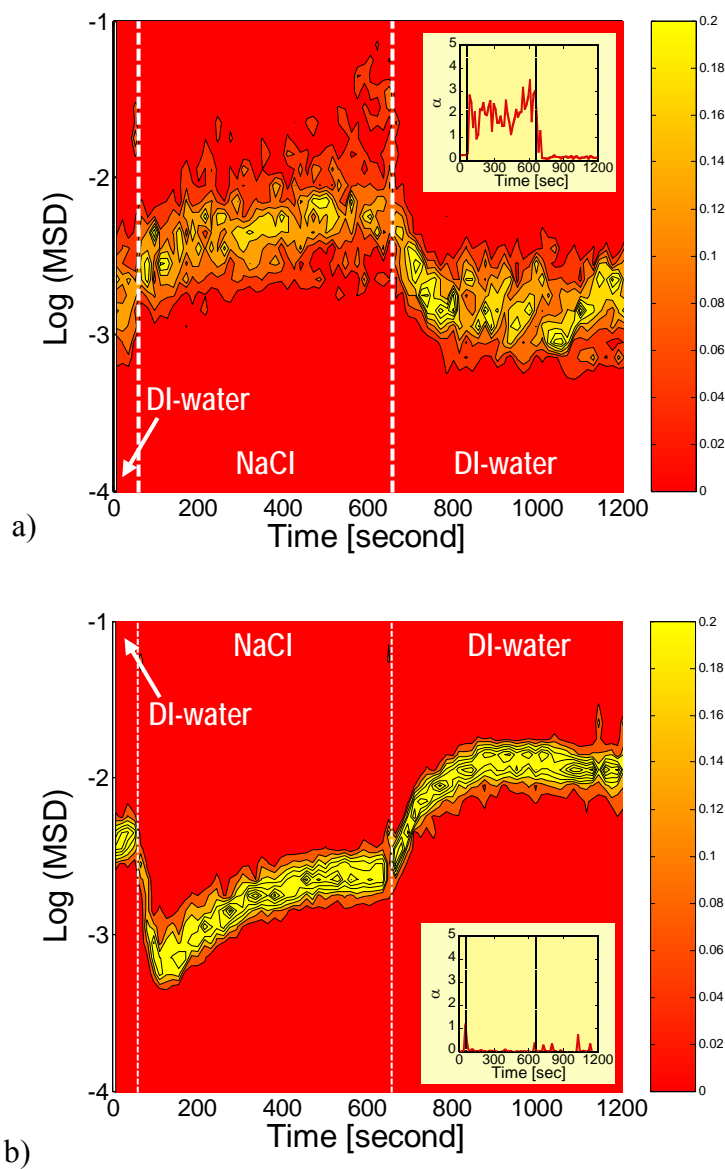


Figure 4.3 Transient PT μ R. Transient MSD distribution at $\tau=0.1$ sec and sample heterogeneity α (insets) for a) 0.25wt.% K₁₆₀L₄₀ and 50mM NaCl, and b) 2.5wt.% K₁₈₀L₂₀ and 100mM NaCl. The dotted lines represent solvent switching.

The PT μ R data can also be used to quantitatively extract the dynamic moduli of the gel in the dialysis cell. Fig. 4.4 shows the steady-state loss and storage moduli, G' and G'' , as a function of salt concentration for dialyzed and macro-mixed gels. In the dialysis cell, a gel-to-liquid transition (crossover of G' and G'') was observed around 50mM NaCl, and the non-Gaussian parameter also reached a maximum for this concentration. At higher ionic strength, the gel structure disintegrated and the samples became homogenous, viscous solutions. Macroscopic mixing of salt resulted in breakdown of the hydrogel for all NaCl concentrations above 10mM. To investigate the reversibility of this process, an actively mixed sample with 100mM NaCl was loaded in the dialysis cell and dialyzed against DI-water for 10min. Interestingly, the gel strength and structure fully recovered after salt removal, becoming even slightly stronger than the initial sample prepared in DI water.

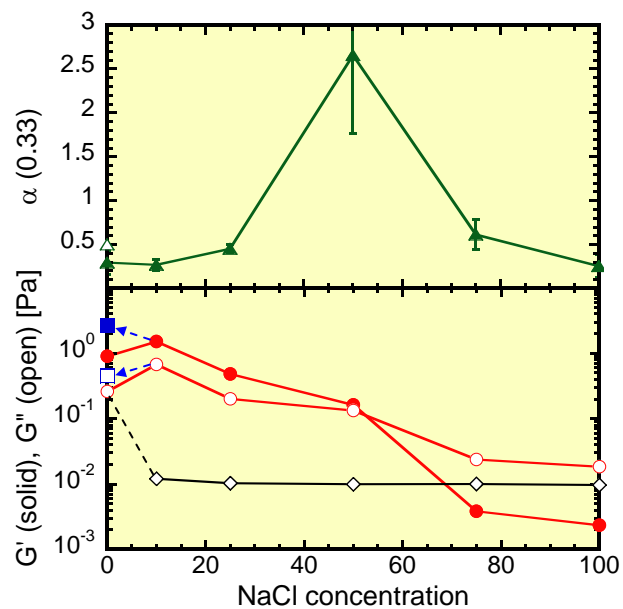


Figure 4.4 Rheology of 0.25wt.% $K_{160}L_{40}$ hydrogel at different NaCl concentrations. Non-Gaussian parameter α ($\tau=0.33$), storage modulus G' (solid symbols), and loss modulus G'' (open symbols), after 10min dialysis (red circles) and with convective macromixing (black diamonds). Blue squares represent rheology of macromixed sample (100mM) after salt removal in the dialysis cell.

Hydrogel microrheology was also determined for different concentrations of $K_{160}L_{40}$ at each stage of the dialysis process (Fig. 4.5). Initially, in DI water the critical gelation point is $\sim 0.2\text{wt}\%$ (red circles). Once dialyzed against 100mM NaCl for 10min, the gels weakened and the critical gelation shifted to $\sim 0.3\text{wt}\%$ (blue squares). After salt removal (green triangles), the critical gelation point dropped to $\sim 0.15\text{wt}\%$, slightly below the initial critical point. Over the entire range of gel concentrations, the gel strength after salt removal was higher than the initial gel strength. When samples were subjected to multiple cycles of salt addition and removal, the gel strength kept creeping up after each dialysis cycle (see section 5.4.2).

Finally, we also investigated the effect of the molecular architecture. Weaker hydrogels of $K_{180}L_{20}$, which is less hydrophobic, were prepared at 2.5wt.%, the macroscopic critical gelation point [100] for this material in DI water (0.25wt.% for $K_{160}L_{40}$). In contrast to $K_{160}L_{40}$, the addition of salt to $K_{180}L_{20}$ (Fig. 4.3b) led to a dramatic decrease of MSD (gel strengthening), followed by a slow increase towards an equilibrium situation in which the gel was still stronger than in DI water. After salt removal, MSD quickly increased and the gel became weaker than the initial sample. Homogeneity was maintained through the entire series of solvent exchanges. A subtle variation in molecular architecture, $K_{160}L_{40}$ and $K_{180}L_{20}$, clearly causes a major change in response dynamics of the gel to the addition and removal of salt.

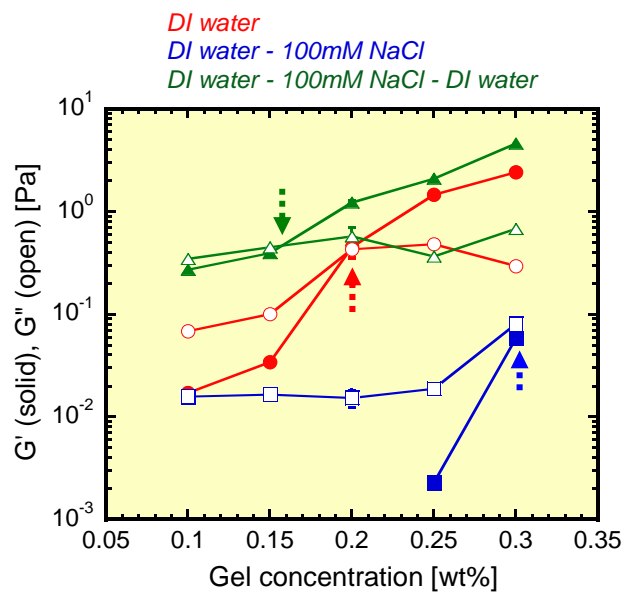


Figure 4.5 Rheology of $K_{160}L_{40}$ hydrogels at different concentrations. Storage and loss moduli, G' and G'' in dialysis cell. Red circles: in DI-water before salt addition, blue squares: in 100mM NaCl after 10min dialysis, and green triangles: in DI-water after salt removal; arrows mark the critical gelation concentrations.

4.4 CONCLUSION

In summary, our experiments provide unique quantitative insight into the evolution of the microstructure and mechanical properties of self-assembled BCP hydrogels in a set-up that mimics the *in vivo* conditions encountered in biomedical applications. We have shown that solvent exchange via convective mixing and dialysis can lead to significantly different hydrogel properties and that commonly applied sample preparation protocols for the characterization of soft biomaterials could lead to erroneous conclusions about microstructural dynamics. It was also found that the breakdown of BCP hydrogels due to mechanical mixing after the addition of salt can be reversed upon dialysis. For practical applications, one can imagine that a sample is prepared at elevated salt concentration and actively mixed to obtain a liquid-like consistency that facilitates injection. Diffusion of excess salt from the gel into surrounding tissue would then restore the gel strength. The 0.25wt.% K₁₆₀L₄₀ gel in this study experiences a gel-to-liquid transition at 50mM NaCl, which is below the typical physiological value of 100mM, but the critical salt concentration increases with BCP concentration and can further be tuned via molecular architecture to obtain hydrogels with the desired salt tolerance. The methodology facilitates the design of gels with appropriate microstructural dynamics for *in vivo* applications like tissue engineering and drug delivery, and can also be applied to study the effect of solvents on self-assembly mechanisms in other responsive soft materials, such as polymer solutions and colloidal dispersions.

CHAPTER 5

SYSTEMATIC INVESTIGATION OF MORPHOLOGY AND RHEOLOGY OF BLOCK COPOLYPEPTIDE HYDROGELS ⁴

5.1 INTRODUCTION

As discussed in Chapter 4, for biomedical applications, it is important to characterize the microstructure of BCP hydrogels under physiological relevant solvent conditions, like *pH* and ionic strength. Previous work revealed that the rheological response of the BCP hydrogels to the presence of additional salt strongly depends on molecular architecture [109]. The addition of salt changes the intermolecular force balance by screening the surface charges of the hydrophilic polyelectrolyte blocks and thus weakens electrostatic repulsion. The shift of intermolecular force balance can cause BCP hydrogels to either strengthen or weaken. In Chapter 4, we proved that the new experimental approach, a microdialysis cell, is a suitable technique since the transport of solvent in the dialysis cell is dominated by diffusion and therefore closely mimics *in vivo* solvent transport in tissue and artificial biomaterials. The work described in Chapter 4 also revealed that the diffusive addition of salt to certain BCP hydrogels in the dialysis cell resulted in a unique porous microstructure, which was easily broken by the external shear stress that is typically applied during sample preparation for rheometry. This result underscored the importance of characterization of microstructural and rheological responses in an environment that mimics *in vivo* conditions in order to optimize the

⁴ The contents of this chapter have been submitted for publication:
Sato, J., Nowak, A.P., Deming, T.J., and Breedveld, V., "Morphological and rheological changes of heterogeneous salt responsive block copolypeptide hydrogels".

performance of biomaterials for tissue engineering and drug delivery applications. Furthermore, the dialysis cell makes it possible to applying a complex series of solvent changes, including repetitive addition and removal of solvent components via dialysis, to investigate sample recovery and reversibility of microstructural changes. Such experiments would provide important information for biomedical applications and the results would also be useful for elucidating the self-assembly mechanism of BCP hydrogels in more detail.

This chapter describes a systematic study of the microstructural response of BCP hydrogels to the controlled manipulation of ionic strength of the solvent. The following control parameters were varied during the study: BCP hydrogel concentration, BCP molecular structure, salt concentration, and tracer particle size for microrheology. The transient microrheological experiments provide a unique view of the microstructural rearrangements that take place in these hydrogels as a result of changes in solvent composition. The results provide guidance for the design of new responsive biomaterials with optimized *in vivo* performance.

5.2 METHODS AND MATERIALS

5.2.1 SAMPLE PREPARATION

We studied $K_{160}L_{40}$ and $K_{180}L_{20}$ hydrogels (K_mL_n : diblock copolypeptide of m residues of L-lysine (K) and n residues of L-leucine(L)). Initially, we prepared a stock solution at high concentration, which was mixed with a vortex mixer and hydrated over night. This cycle of mixing and resting was repeated for at least few days to completely dissolve and homogenize the concentrated stock solution. Samples were then prepared by dilution with DI water and tracer particle suspension to achieve the desired BCP concentration. Since the K_mL_n BCPs have positively charged polyelectrolyte lysine-blocks, we selected positively charged fluorescently labeled polystyrene tracer particles

(0.37 μ m and 0.72 μ m in diameter, amidine-functionalized, Invitrogen), so that their surface chemistry was compatible with sample properties. The surface charge densities of both particle types are the same. The diluted samples were again left over night to achieve equilibrium.

5.2.2 DIALYSIS CELL AND SOLVENT MANIPULATION

As reported in Chapter 2, the dialysis cell for transient microrheology of solvent responsive complex fluids [98] is capable of rapid solvent manipulation without applying external shear stress. During the solvent exchange, the microstructure and rheology of the sample can be monitored. The sample thickness is about 120 μ m (thickness of No.0 coverslip) and the volume is ca. 0.9 μ l. Diffusive transport of ions in the dialysis cell has been characterized in detail previously through numerical calculations (section 2.2.2) and validation experiments (section 2.4.1) confirmed that solvent is fully exchanged within a few minutes.

In the experiments reported here, the solvent was switched from DI water to NaCl solutions of varying ionic strength to study the salt response of BCP hydrogels and successively changed back to DI water to study reversibility of the microstructural changes. In recovery tests, the BCP samples were initially prepared in NaCl solution and the dialysis cell was used to change the solvent to DI water. In all experiments, the solvent was changed after recording a 1 min movie to establish a baseline; the length of successive solvent exchange intervals was 10 min to enable equilibration. In most experiments, the NaCl concentration was 100mM, a physiologically relevant ionic strength.

Optical access to the sample chamber on a research-grade inverted microscope makes the dialysis compatible with fluorescence microscopy techniques. For this study, we used laser scanning confocal microscopy to visualize the distribution of fluorescent

dye molecules and particle tracking microrheology (PT μ R) of fluorescent tracer particles to quantify the local mechanical properties in the sample.

5.2.3 LSCM

For LSCM (VT-eye, VisiTech International) hydrogel imaging, lipophilic fluorescent dye (DiOC18, Molecular Probes) was dissolved in THF to saturation (micromolar range) and mixed completely [100, 110]. Then, the solution was added to hydrogel to achieve 0.25wt. % K₁₆₀L₄₀ hydrogel solution. The dye has fluorescence at hydrophobic region and little fluorescence in the water phase, so that we can achieve a high-contrast image. For transient LSCM, a slow shutter speed (0.17s exposure every 30s, 20x oil immersion lens) was used to avoid excessive photobleaching.

5.2.4 TRANSIENT MICRORHEOLOGY

An inverted microscope (Leica DM-IRB) was equipped with an analog, Peltier-cooled 640 x 480 pixel CCD camera (30Hz frame rate, COHU 4920, Poway, CA), which was connected to a PC. Images were transferred to the PC and recorded real-time onto the hard drive with a precision frame grabber (PXC-200, Cyber Optics) and specialized image acquisition software (OpenBox) [51]. The spatial resolution of the imaging system with 100x oil-immersion objective was 0.099 μ m per pixel.

The fluorescent particles that were premixed in the hydrogel samples acted as tracers for particle tracking microrheology (PT μ R) [24-26]. PT μ R determines the rheological properties of a sample by tracking the motion of Brownian tracer particles and takes advantage of the generalized Stokes-Einstein relation (GSE) that links particle mobility to the sample rheology:

$$\langle \Delta \tilde{r}^2(s) \rangle = \frac{dk_B T}{3\pi a s \tilde{G}(s)}, \quad (2.2)$$

where $\langle \Delta \tilde{r}^2(s) \rangle$ is the Laplace transform of the mean-squared displacement (MSD) of the

particles, $\langle \Delta r^2(\tau) \rangle$, τ is the lag time, s is the Laplace frequency, a is the radius of the tracer particles, k_B is Boltzmann's constant, T is the absolute temperature, and d is the dimensionality of the displacement vector Δr . Particle positions were detected in every video frame and trajectories were reconstructed through image analysis with the software package IDL (Research Systems Inc.), using algorithms developed by Crocker and co-workers [52].

In Chapter 3, we have reported guidelines and methodology for extracting transient microrheological data from particle trajectories with the objective to monitor dynamic changes in rheology and microstructure. The key element of this process is to optimize the trade-off between temporal resolution and statistical validity, which is particularly challenging for heterogeneous samples. In brief, the transient method splits the movie of tracer particle motion into short segments (15s), during which MSD values of individual particle are calculated only for short lag time values ($\tau = 0.033\text{--}0.2\text{s}$) because of statistical limitations. It was shown that these settings are appropriate for accurately tracking rheological and microstructural changes of BCP gels in response to salt addition and/or removal.

In this chapter, data about tracer mobility evolution is presented in the form of contour plots of transient histograms. Because of the heterogeneous nature of the BCP samples, the mean-squared displacements must be determined for individual tracer trajectories. The MSD of individual tracer trajectories can be characterized by two parameters: the magnitude of MSD at $\tau = 0.167\text{s}$ and the local slopes in the $\log(\text{MSD})\text{--}\log(\tau)$ plot. These two quantities have clear physical meaning and accurately describe the rheological properties of the sample. The magnitude of the MSD represents particle mobility, and is thus a direct measure of the strength of the material, low MSD values being equivalent to high tracer mobility and vice versa. The local slope must range between 0 and 1 for all viscoelastic materials in thermal equilibrium and describes the

degree of viscoelasticity of the material: for viscous Newtonian fluids (dominant loss modulus $G'' \gg G'$) the slope equals 1 ($\text{MSD} \sim \tau$), while for purely elastic solids (dominant storage modulus $G' \gg G''$) the slope is close to 0 (constant MSD). Gelation occurs when $G' = G''$, which is equivalent to a slope of 0.5. As a result, transient histograms of the MSD magnitude and slope are excellent for visualizing changes in sample microrheology and give a clear qualitative picture of sample microrheology. Quantitative rheological analysis is then performed by calculating the dynamic moduli G' and G'' for each tracer trajectory from the corresponding MSD value and slope via an algebraic form of the generalized Stokes-Einstein equation (Eq. (3.1)) [25, 53, 99]. The advantage of the algebraic approximation is that it does not require Laplace transforms. Average microrheological properties for the tracer population (MSD, slope and dynamic moduli) are determined as the weighted average of the individual particle distribution; the weighing factor is the length of individual trajectories in order to properly account for statistical relevance of each data point (see section 3.3).

In addition to transient microrheological studies, results from more traditional steady state analysis methods are presented. When sample properties are constant, tracer MSD can be averaged over longer time intervals than in transient experiments, which leads to reduction of statistical noise. In these cases, we applied a modified algebraic form of the GSE equation [99] that results in slightly more accurate calculations of the local dynamic moduli, G' and G'' . Finally, a non-Gaussian parameter, $\alpha(\tau) = (\langle \Delta x(\tau)^4 \rangle / 3 \langle \Delta x(\tau)^2 \rangle^2 - 1)$ (Eq. 3.5), is used to quantify the heterogeneity of the sample. For homogeneous samples, the distribution of tracer displacements due to Brownian motion follows a Gaussian distribution, which results in $\alpha = 0$ for all lag times τ . Non-Gaussian distributions are observed for heterogeneous systems, resulting in positive, non-zero values for α , that are a measure for the degree of sample heterogeneity.

5.3 RESULTS

To elucidate the microstructural response of BCP hydrogels to changes in solvent composition, we systematically varied key experimental parameters: block copolypeptide concentration, molecular structure and salt concentration. We also investigated the effect of two key experimental parameters: the tracer particle size and spatial variation of hydrogel rheology across the dialysis cell.

5.3.1 THE EFFECT OF GEL CONCENTRATION

5.3.1.1 $K_{160}L_{40}$

At first, we studied the effect of BCP concentration on salt-responsiveness in $K_{160}L_{40}$ hydrogels. Concentrations were varied from 0.1 to 0.3wt.%, around the macroscopic critical gelation concentration as measured with a rheometer [109]. Tracer particles with 0.37 μ m diameter were used. After 60s exposure to DI water, the hydrogels were dialyzed against 100mM NaCl for 600s and subsequently the solvent was switched back to DI water for another 600s. The movies of tracer particle motion were recorded ~35 μ m above the bottom of the dialysis cell in order to avoid wall effects. The results are presented in Fig. 5.1, which shows the transient distributions of MSD magnitude and slope for three different samples during the entire experiment. As can be seen, significant changes in hydrogel rheology were observed after the addition of 100mM NaCl for all $K_{160}L_{40}$ concentrations. Although the slope did not change noticeably after the first solvent switch from DI water to salt solution, the MSD values clearly increased. This indicates that the hydrogels in this concentration range weakened after the addition of salt, while the level of viscoelasticity remained unaffected. The weakening of $K_{160}L_{40}$ gels in response to salt addition was previously observed with macroscopic rheometer measurements [109]. With increasing BCP concentration, we observed decreasing MSD values and slopes. The weighted average slope for 0.1wt.% samples is approximately 1,

which is characteristic for liquid-like behavior; at 0.2wt.% the slope is close to 0.5, which marks the critical gelation point at which G' equals G'' . For reference, these 0.37mm tracer particles would have an average slope of 1 and $\log(\text{MSD})$ values of circa -0.8 when dispersed in DI water, according to the Stokes-Einstein equation. The lower MSD values at higher concentrations represent an increase in gel strength. Interestingly, the MSD values at 0.2wt. % and 0.3wt. % (data not shown here) are much more broadly distributed than at lower concentrations, which is the signature of sample heterogeneity. This was in agreement with qualitative observation under the microscope in Chapter 4: some particles seemed to diffuse freely, while others were trapped in gel networks.

The removal of NaCl after 660s, caused significant drops of both the MSD values and slopes to even below their initial values in DI water. Apparently, the dialysis cycle enhances the gel strength. For instance, at 0.15wt.% (Fig. 5.1b), which is slightly below the macroscopic gelation concentration in DI water, the liquid-like initial sample changed to a weak gel after completion of the dialysis experiment. The wide MSD distribution for 0.2wt.% after the addition of salt, narrowed again after salt removal: the sample became heterogeneous with the addition of salt and regained homogeneity after salt removal. As seen in Fig. 5.1a-c, the MSD values rapidly reached plateau values after the addition of salt, and the BCP concentration does not seem to affect the transition speed in this concentration range. However, the gel strengthening transition upon salt removal was noticeably quicker at higher salt concentration; this effect will be analyzed in more detail towards the end of the results section.

5.3.1.2 $K_{180}L_{20}$

We performed the same salt-response experiments as described above for 1.75~3.5wt. % $K_{180}L_{20}$ hydrogels. Again the concentration range was chosen to be near the macroscopic critical gelation concentration [109]. The results of the experiments are shown in Fig. 5.2. For all concentrations, we observed opposite rheological transition

trends from the behavior of $K_{160}L_{40}$ in Fig. 5.1 Upon the addition of salt, both the MSD values and slopes dropped drastically, followed by a slow recovery process. This indicates that the hydrogels stiffened with the addition of salt and successively relaxed to a weaker equilibrated state. The gel stiffening of $K_{180}L_{20}$ with added salt was previously observed in macroscopic rheometry as well, but the dynamics of the process could not be probed [109]. As expected, the MSD values and slopes decreased with increasing BCP hydrogel concentration. The spikes around 60 and 660s are artifacts and are caused by mechanical disturbances that occur when the microscope stage is touched during solvent switching. Broad distributions of MSD values, which were found for $K_{160}L_{40}$ hydrogels in the presence of salt (Fig. 5.1c), were not observed for $K_{180}L_{20}$ hydrogels. The narrow MSD distributions suggest that these gels are more homogeneous on the particle length scale.

After the removal of salt at $t = 660$ s, both the MSD values and slopes increased strongly: the gels weakened beyond their initial gel strength. Again, there is evidence of an overshoot, followed by slow recovery. For instance, at 3.5wt.%, the initially weak gel near the critical gelation point, showed a clear liquid-to-gel transition after the addition of salt and gel-to-liquid transition after salt removal. The microrheological transitions upon salt addition occurred rapidly for all concentrations, whereas the recovery processes after salt removal were relatively slow. The contrast between the two BCP materials could not have been starker: while $K_{160}L_{40}$ hydrogels weaken in the presence of salt, $K_{180}L_{20}$ gels, which have lower initial strength, actually become stronger. The experimental data of Figs. 5.1 and 5.2 represents the first in-situ transient studies of these microstructural rearrangements.

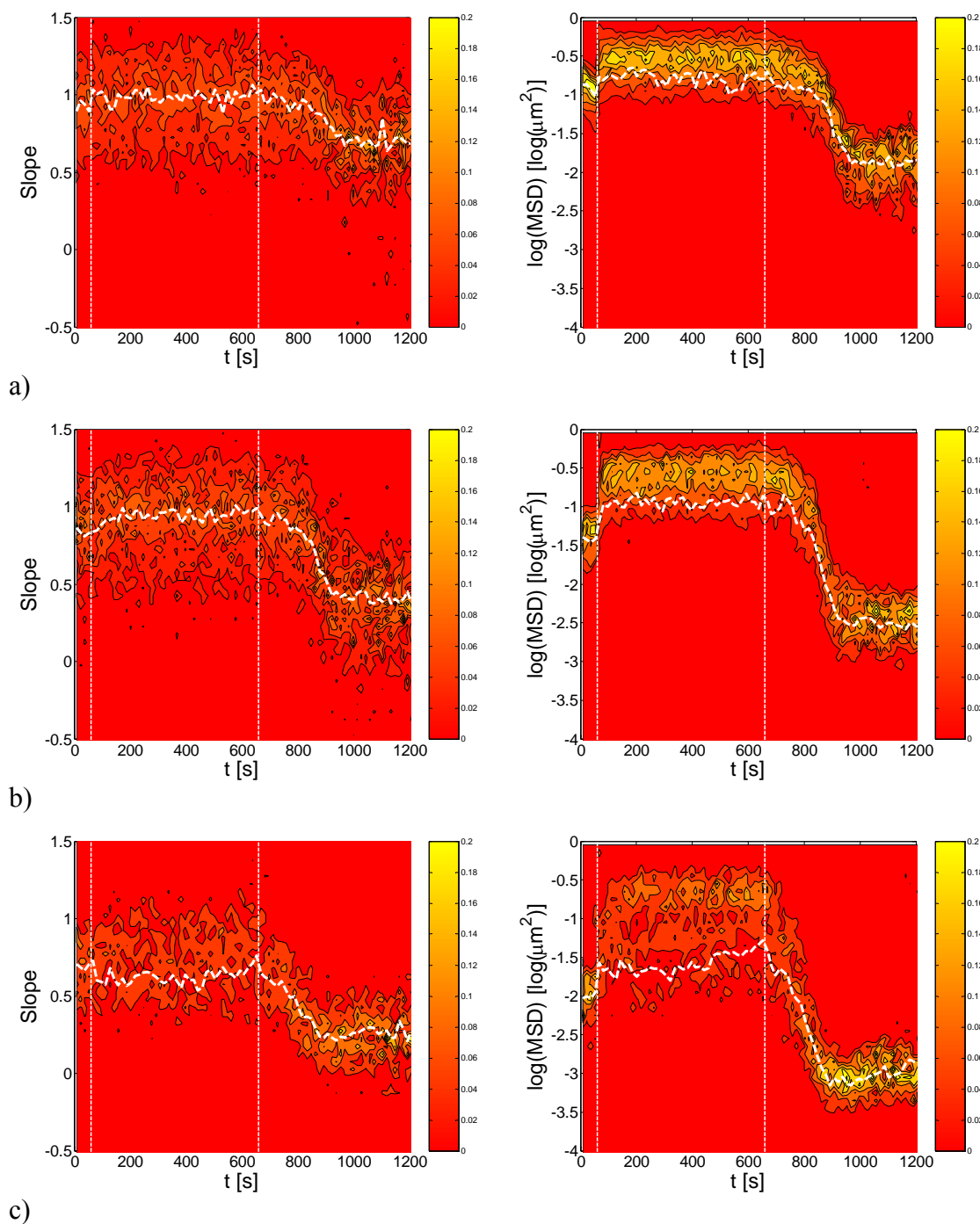


Figure 5.1 Contour plots of transient histograms of slope and MSD values ($\tau=0.167s$) for $K_{160}L_{40}$ hydrogels at a) 0.1wt.%, b) 0.15wt.%, and c) 0.2wt.% with $0.37\mu m$ particles, $35\mu m$ from the bottom of the dialysis cell. Solvent manipulation sequence: DI-water (60s) \rightarrow 100mM NaCl (600s) \rightarrow DI-water (600s), solvent switches indicated by vertical lines. The dashed white curve represents the weighted average values for slope and MSD values.

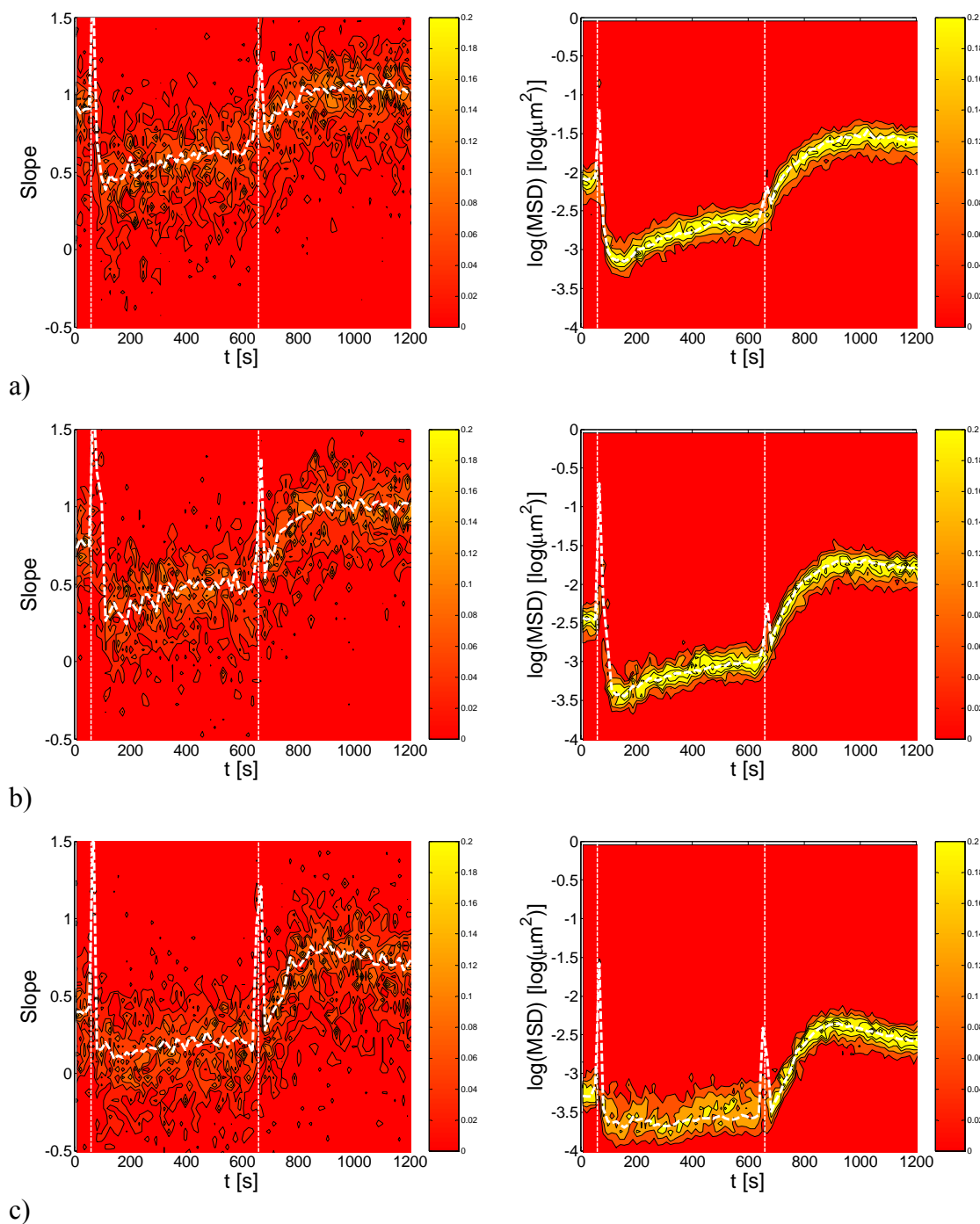


Figure 5.2 Contour plots of transient histograms of slope and MSD values ($\tau=0.167s$) for $K_{180}L_{20}$ hydrogels at a) 2.0wt.%, b) 2.5wt.%, and c) 3.5wt.% with $0.37\mu m$ particles, $35\mu m$ from the bottom of the dialysis cell. Solvent manipulation sequence: DI-water (60s) \rightarrow 100mM NaCl (600s) \rightarrow DI-water (600s), solvent switches indicated by vertical lines. The dashed white curve represents the weighted average values for slope and MSD values.

5.3.2 THE EFFECT OF MOLECULAR ARCHITECTURE

The initial comparison of the two molecular architectures, which only differ in relative block lengths of the lysine and leucine blocks, motivated a more detailed quantitative analysis of the sample rheology. For the samples studied above (0.1-0.3wt.% K₁₆₀L₄₀ and 1.75-3.5wt.% K₁₈₀L₂₀ hydrogels), the dynamic moduli G' and G'' , were determined through steady state PT μ R analysis of the final 50s of each solvent interval. The salt concentration was fixed as 100mM NaCl.

The dynamic moduli for all K₁₆₀L₄₀ and K₁₈₀L₂₀ hydrogels are shown in Fig. 5.3 at three stages of the dialysis cycle: in DI water, after addition of NaCl, after removal of NaCl. Initially, the gelation concentration, marked by the crossover of G' and G'' , was ca. 0.2wt. % for the K₁₆₀L₄₀ hydrogels, which is in good agreement with the macroscopic measurements with a rheometer [109]. After the addition of salt, the gelation concentration increased to ca. 0.3wt.%. This stronger, more brittle microstructure is unique for diffusive transport of salt molecules. As reported in Chapter 4, macroscopic convective mixing after the addition of 100mM NaCl results in complete break-down of the gel structure. In the dialysis cell, NaCl can be removed by dialysis against DI water, and after salt removal the gelation concentration dropped to 0.15wt.%, even slightly lower than the initial gelation concentration (Fig. 5.3a). This behavior coincides with the gel weakening upon salt addition and strengthening transition upon salt removal as was observed in Fig. 5.1. The shift of the gel point with the addition of salt (0.2wt.% \rightarrow 0.3wt.%) is more dramatic than the shift from initial to final gelation concentration in DI water (0.2wt.% \rightarrow 0.15wt.%). For K₁₈₀L₂₀, the gelation concentration was initially ca. 2.8wt.%, which is somewhat higher than the macroscopic critical concentration (2.0wt.%) observed with a rheometer (Fig. 5.3b) [109]. The addition of salt results in a drop to ca. 2.2wt.%, which corresponds to the gel strengthening observed in Fig. 5.2 and with a rheometer [109]. After salt removal, the gelation concentration increased to ca.

3.4wt.%, higher than the initial critical concentration. Again, this is consistent with the qualitative observations in Fig. 5.2.

$K_{160}L_{40}$ hydrogels, which have a longer hydrophobic block, showed more pronounced salt sensitivity than $K_{180}L_{20}$ hydrogels. As was already obvious from the transient measurements in Figs. 5.1 and 5.2, a slight variation in molecular architecture ($K_{160}L_{40}$ and $K_{180}L_{20}$) leads to completely opposite gelation behavior in the presence of NaCl. These experiments highlight our ability to monitor the response of these hydrogels in detail in a device that mimics *in vivo* transport conditions, which is of critical importance for designing high-performance biomaterials for tissue engineering and drug delivery. The results also emphasize that the microstructural response of these materials is highly tunable via molecular architecture, spanning the range from salt weakening to salt strengthening.

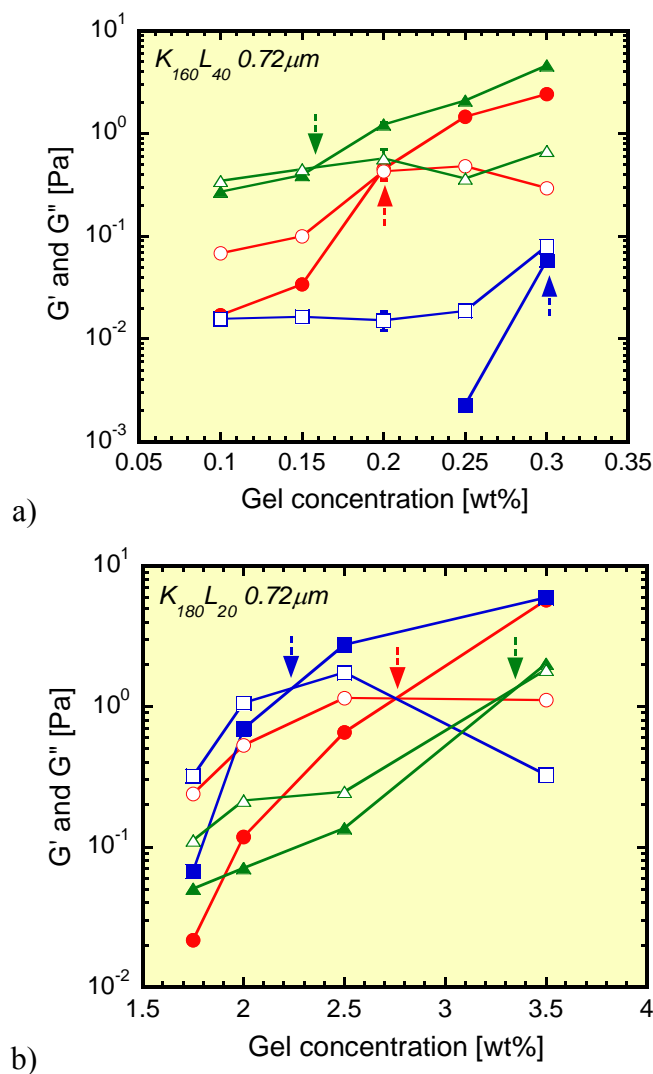


Figure 5.3 The dynamic moduli, G' (solid symbols) and G'' (open), for a) $K_{160}L_{40}$ and b) $K_{180}L_{20}$ hydrogels as a function of BCP concentration at three stages of the dialysis cycle: in DI water (red circles), after addition of 100mM NaCl (blue squares), after removal of NaCl (green triangles); the gelation concentrations are identified by arrows.

5.3.3 HETEROGENEITY

Transient heterogeneity was evaluated by calculating the non-Gaussian parameter α for the lag time $\tau = 0.33$ s. The results for $\alpha(t)$ are shown in Fig. 5.4a for 0.15wt.% and 0.25wt.% K₁₆₀L₄₀ hydrogels (see also Fig. 5.1a-c) during the dialysis cycle with a 50mM NaCl solution (DI-water (60s)→ 50mM NaCl (600s)→DI-water (600s)). The value of α rapidly increased after the addition of salt and reached an equilibrium state, which suggests the evolution of a strongly heterogeneous structure, which was already suggested by the wide distribution of MSD values in Fig. 5.1c. After the removal of salt, α dropped to values close to zero, indicating reversibility of the salt-induced heterogeneity. At the higher BCP concentration, 0.25wt.%, the heterogeneity of the hydrogel with 50mM NaCl is more noticeable. The response during the second solvent exchange (50mM NaCl→DI-water) was slower for lower BCP concentrations; this is in agreement with the qualitative observation in Fig. 5.1 that the recovery speed of gel strength varied with BCP concentration. Before and after the dialysis cycle, α values were close to zero, and no hysteresis was observed in heterogeneity.

The effect of salt concentration on heterogeneity was studied for 0.15 and 0.25wt.% K₁₆₀L₄₀ hydrogels (Fig. 5.4b). The values of α in this graph were taken by averaging the results of a transient experiment over the last 60s before switching back to DI water. The interesting observation is that there is a distinct peak in heterogeneity around 50mM NaCl concentration. Both below and above this salt concentration, the samples appear more homogeneous. If we combine these observations with the data in Fig. 5.1 (for 100mM NaCl), the following picture emerges: the addition of NaCl leads to a decrease in gel strength for all K₁₆₀L₄₀ concentrations and ionic strengths and increasing the NaCl concentration from 0 to 100mM leads to initially an increase in heterogeneity, which subsequently decreases again. At intermediate salt concentrations, a stable, brittle heterogeneous gel structure exists, which falls apart at higher salt concentrations,

resulting in a more homogeneous, weak gel. The distinct peak at 50mM NaCl coincides with the salt concentration that leads to a critical gel with $G' \approx G''$. It is expected that around this gelation transition, the sample consists of liquid and gel-like regions, which contribute equally, thus resulting in maximum heterogeneity. For 0.15wt.%, the α -peak became smaller and broader, because of lower gel formation tendencies. These results show the microstructural heterogeneity can be tuned with salt and gel concentrations, which is of importance for the transport of macromolecular components (drugs, nutrients, waste products) in potential application.

In the final set of heterogeneity experiments, we investigated the effect of tracer particle size on the measured sample heterogeneity. We used two particle sizes (0.37 and 0.72 μ m diameter) and at different concentrations of K₁₆₀L₄₀. Fig. 5.4c presents the resulting heterogeneity 10min after switching the solvent from DI water to 100mM NaCl. For both particle types, α increased with gel concentration. Also the heterogeneity experienced by the 0.37 μ m particles was significantly larger than the 0.72 μ m particles at all BCP concentrations. These experiments confirm that the BCP hydrogels have characteristic length scales that are on μ m length scale, so that the tracer particle size is relevant. For example, one might imagine a system with pores that have a size distribution with average pore diameter of 0.5 μ m; many of these pores would be accessible to the small 0.37 μ m tracers for free diffusion, while the larger 0.72 μ m tracers would be stuck. As the length scale of heterogeneities grows, one would expect small tracers to experience them first. The effect of particle size on the measurements of rheological parameters is discussed in more detail below.

For all K₁₈₀L₂₀ hydrogels, the α values stayed close to zero during the entire series of solvent exchanges (DI-water \rightarrow 100mM NaCl), independent of the gel concentration within the range of 1.75~3.5wt.% (not shown here). These results proved that K₁₈₀L₂₀ hydrogels are homogeneous on the micrometer length scale.

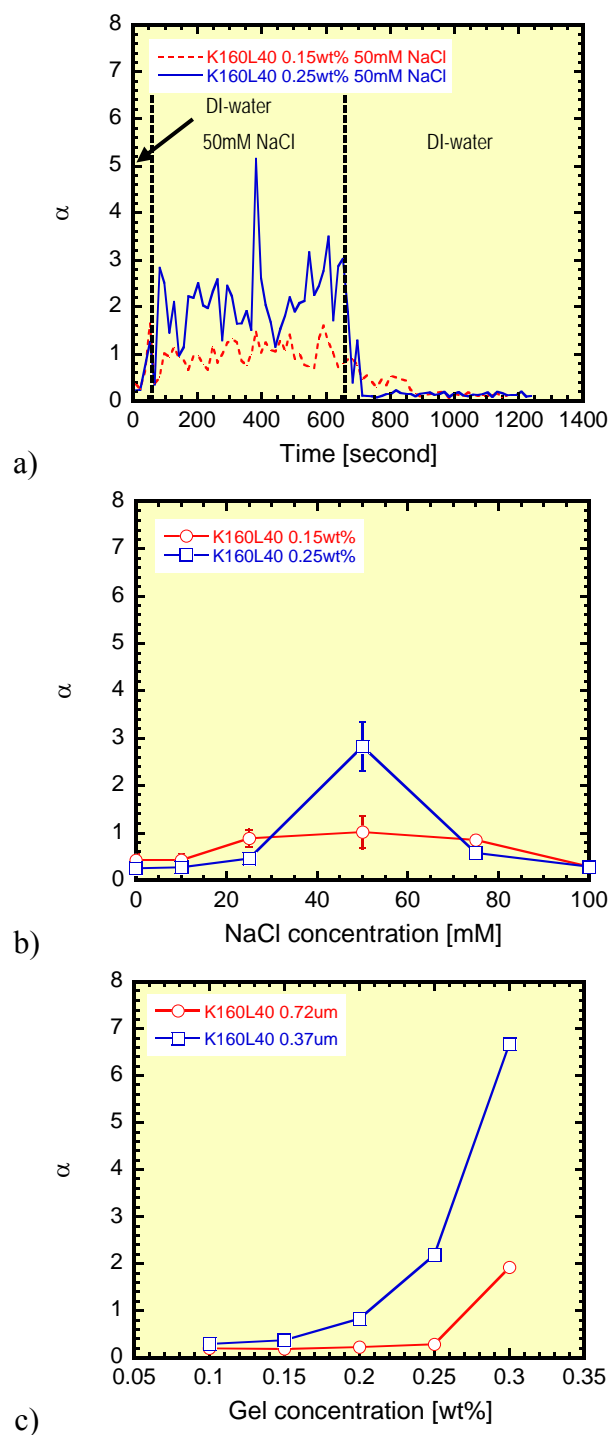


Figure 5.4 a) Transient non-Gaussian parameter α for two concentrations of $K_{160}L_{40}$ (0.15 and 0.25 wt.%) during a dialysis cycle, b) The effect of NaCl concentration on the sample heterogeneity for the same samples, and c) The effect of particle size on α at various concentrations of $K_{160}L_{40}$.

5.3.4 SPATIAL VARIATIONS ACROSS THE DIALYSIS CELL

During the measurements of transient microrheology, suspicions arose about the homogeneity of samples across the sample. Since PT μ R readily enables measurements at different locations inside the sample chamber by moving the focal plane of the micrometer, we performed a set of experiments to investigate the effect of location in the dialysis cell on the dynamic moduli for 0.25wt.% K₁₆₀L₄₀ and 2.5wt.% K₁₈₀L₂₀ hydrogels with 100mM NaCl. For these experiments, the larger tracer particles (0.72 μ m diameter) were used. PT μ R was carried inside the sample chamber was varied from the bottom to the top (near the membrane surface): four locations excluding the both surfaces (see the inset of Fig. 5.5b). Movie segments (60s) at the end of each solvent step were used to determine the local dynamic moduli, G' and G'' .

For K₁₈₀L₂₀ gels, we did not observe significant depth dependence of the dynamic moduli, whose variation was within 10% across the entire cell. However, K₁₆₀L₄₀ hydrogels showed a strong depth dependency. Figure 5a presents spatial variations of the moduli at the end of all three stages of the dialysis cycle. Before the addition of salt, in DI water, the moduli were found to be location independent. After the addition of salt, this picture changed drastically and moduli were strongly dependent on location. The hydrogel sample remained gel-like near the bottom surface, with relatively minor changes in moduli, while strong weakening and transition to liquid-like behavior were observed near the membrane; the gel transition for which $G' \approx G''$, occurred around 40 μ m from the bottom. Variations of G' across the sample were as large as a factor 10^3 in these measurements. Upon salt removal, the gel strength recovered and near the bottom it even exceeded the original value in DI water. However, the sample remained liquid-like near the membrane and did not fully recover to the initial gel strength over the course of the experiment. The gel transition after salt removal occurred at a distance of ca. 80 μ m from the bottom.

In the same experiments, the location dependence of the non-Gaussian parameter α was also measured (Fig. 5.5b). It was found that in DI water, both before salt addition and after salt removal, the sample is locally homogeneous, even though the moduli varied between different locations (Fig. 5.5a). In the presence of salt, however, significant local heterogeneity was observed, in particular near the bottom of the sample.

The spatial variation of moduli and α present an interesting picture of the microstructure of the self-assembled K₁₆₀L₄₀ hydrogel. From the rheological data we can conclude that the diffusive addition induces macroscopic phase separation across the sample, which does not fully recover after 10min dialysis against DI water. At the same time, the non-Gaussian parameter α indicates that there is also a local microscopic phase separation in the K₁₆₀L₄₀ gels due to the addition of salt, especially in the gel-like regions of the sample. This microscopic phase separation is reversible and disappears after salt removal. The depth dependence was also evaluated at a slightly lower concentration of 0.15wt.% K₁₆₀L₄₀ and similar results were observed, although the variations in moduli were not quite as strong. Apparently, the self-assembled K₁₆₀L₄₀ gel collapses both on a microscopic and macroscopic scale when salt is added, because the additional ions screen the repulsive interactions between polyelectrolyte lysine-blocks. After removal of salt, the gel recovers quickly on the microscopic level, but swelling on the macroscopic level is much slower and full recovery was not observed. This effect can of course not be neglected when interpreting the data presented in Fig. 5.1, where data were collected in the gel-like region close to the bottom of the sample chamber. Once again, the slightly different molecular architecture of K₁₈₀L₂₀ strongly affects gel swelling and deswelling behavior, which provides excellent opportunities for the design of materials with tunable responsiveness.

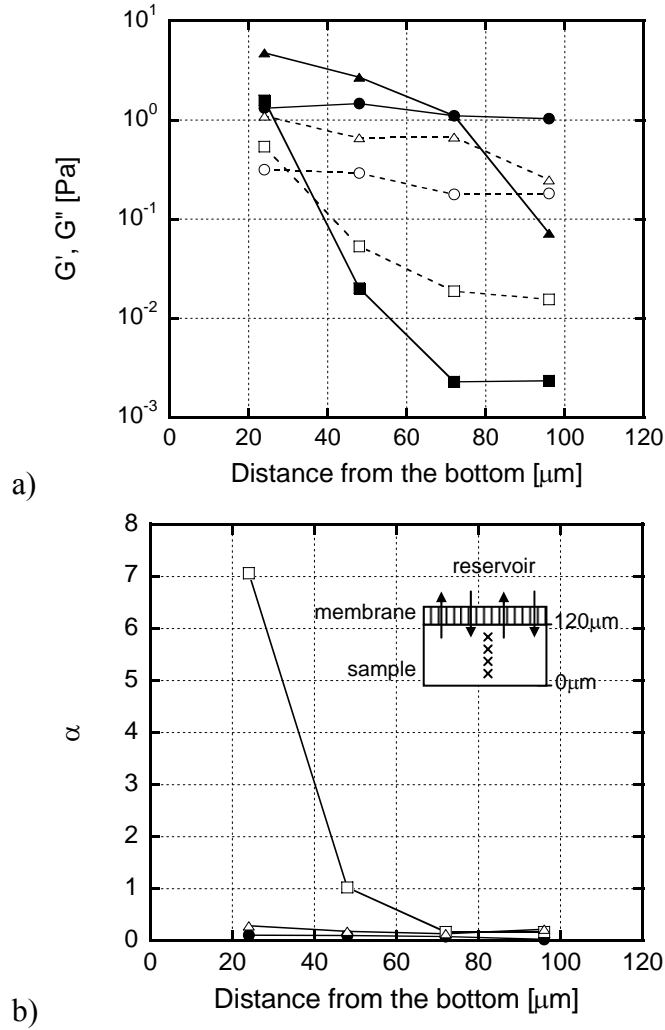


Figure 5.5 Depth dependent a) dynamic moduli, G' (solid symbols) and G'' (open symbols), and b) non-Gaussian parameter α ($\tau=0.33\text{s}$) for 0.25wt. % K₁₆₀L₄₀ hydrogels at three stages of the dialysis cycle: in DI water (●, ○), after 10min dialysis against 100mM NaCl (■, □), and after 10min of salt removal with DI water (▲, △). The distance is measured from the bottom of the sample chamber as shown in the inset of b).

In addition to the microrheology measurements, samples were also monitored with LSCM during the solvent exchange experiments. A hydrophobic dye was used to label the structure and some interesting qualitative observations were made that strengthen the quantitative results presented above. The local collapse of the gel structure was occasionally observed very clearly with LSCM through the formation and growth of cracks in the gel structure after the the addition of salt. After salt removal, these cracks shrunk, but the gel matrix never healed completely (see Fig. 5.6b). Our hypothesis is that locally the phase separation creates stresses that are strong enough to disrupt the fragile network. We have previously reported significant changes of brittleness of $K_{160}L_{40}$ hydrogels with added salt: in oscillatory strain sweeps in the rheometer, the critical strain decreased by a factor of ~ 30 after the addition of 100mM NaCl [109]. Since hydrogel fracturing in response to solvent exchange would generally be undesirable for *in vivo* biomaterial applications [112], further investigation on these fracturing mechanisms in a confined sample volume is needed.

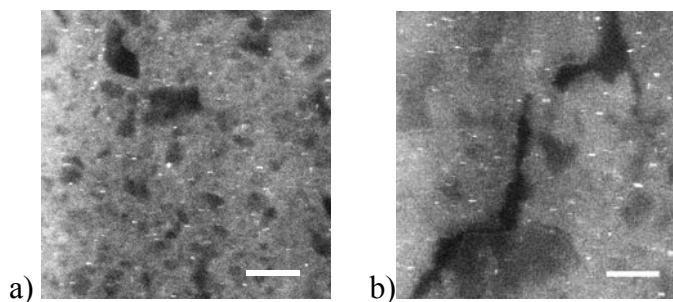


Figure 5.6 LSCM images of 0.25 wt.% $K_{160}L_{40}$ hydrogel with evolving crack a) in DI water before addition of salt, b) in DI water after the addition and subsequent removal of 100mM NaCl; scale bar 10 μ m.

5.4 DISCUSSION

5.4.1 THE EFFECT OF TRACER SIZE

For homogeneous viscoelastic media, the effect of the particle radius a on tracer mobility must obey a scaling rule, $\text{MSD} \sim 1/a$, when $a \gg \xi$, where ξ is the typical length scale of microscopic sample inhomogeneity, for example the mesh size of the hydrogels, or pore size in porous medium. As a result, $(\text{MSD} \cdot a)$ should be constant. If $a \approx \xi$, particle mobility depends strongly on the particle size and generally the $(\text{MSD} \cdot a)$ decreases as the ratio a/ξ increases: larger particles are more hindered by interaction with the inhomogeneous medium than small ones [75]. For porous samples with a well-defined, narrow pore size distribution, the size of these pores can be obtained by using small tracers ($a < \xi$) and evaluating the quantity $a + (\text{MSD})^{1/2}$ at long lag times τ , independent of particle size. The quantity $a + (\text{MSD})^{1/2}$ represents the average pore size [78]. When the mesh sizes ξ are broadly distributed, like in many heterogeneous media, a mesh size distribution can be extracted by evaluating the pore size for individual tracer trajectories [81]. In our transient microrheology measurements, such an analysis cannot be performed, because we can only access short lag time values in time-resolved experiments. Instead, we evaluated the effect of particle size on the local rheological properties and tracer MSDs by using two particle sizes: $0.37\mu\text{m}$ and $0.72\mu\text{m}$ in diameter. Both particles have a similar surface charge density: $15.2 \mu\text{C}/\text{cm}^2$ for $0.72\mu\text{m}$ and $15.3 \mu\text{C}/\text{cm}^2$ for $0.37\mu\text{m}$. We used short movie segments (50s) at the end of each solvent step to calculate steady-state dynamic moduli.

Data for the larger particles ($0.72\mu\text{m}$) were presented in Fig. 5.3a and Fig. 5.7a contains the equivalent results for the small tracers ($0.37\mu\text{m}$) as a function of $K_{160}L_{40}$ concentration. Qualitatively, the figures look similar, exhibiting the same trends as discussed in detail for Fig. 5.3a. For both particles, we observed shifts in the gelation

transitions after subsequent solvent changes. However, a closer inspection of the quantitative data reveals that the small tracer particles probed slightly higher local elasticities after dialysis, while we did not observe a significant difference before dialysis. We looked at these effects in more detail by using the scaling rule for homogeneous samples: $(\text{MSD} \cdot a) = \text{constant}$. We calculated $(\text{MSD} \cdot a)$ for both particle sizes after each solvent change and in Fig. 5.7b the ratio $(\text{MSD} \cdot a)_{0.37} / (\text{MSD} \cdot a)_{0.72}$ is plotted versus BCP concentration. If the sample is homogeneous, one would expect this ratio to be equal to 1 (solid line in Fig. 5.7b); another interesting limiting case would be $\text{MSD}_{0.37} = \text{MSD}_{0.72}$, which leads to a value of 0.51 for the ratio (dotted line). Before the addition of salt, the ratio fluctuates slightly below 1, but after the addition and subsequent removal of salt the ratio drops much further to values below 0.51. Physically, this means that the larger tracers experience larger displacements than the small particles, which is unexpected and counterintuitive; even in heterogeneous samples one would expect small tracers to be more mobile than large ones [74, 113]. There are a few cases in literature where similar observations have been made. Lu and Solomon studied the effect of particle size on tracer MSD for solutions of hydrophilic-hydrophobic associating polymers, and observed that MSD increased with increasing particle size at high polymer concentrations [27]. Tuesta *et al.* pointed out the analogy between this behavior and size exclusion chromatography, where small molecules have a longer retention time than large species because they can become trapped in tortuous networks of narrow pores, while large molecules never enter these pore networks [114]. Another potential explanation for the observed anomalous scaling with particle size could be the presence of a depletion layer near the particle surface. The effect of depletion layers on tracer diffusion has been studied in the framework of a two-layer model [115] by employing both one-particle and two-point microrheology [29, 30]. It was found that the depletion layer thickness decreased linearly with the polymer concentration for coil-like polymer (λ -DNA) [33] and that the layer thickness increased for increasing particle size for semi-flexible polymers (*f*-actin) [32] and

rigid rods [116]. If the mobility of the particle is dominated by the depletion layer, this would explain our results. From previous rheometry studies, it was concluded that BCP hydrogels consist of fairly rigid fibrillar assemblies [106]. Although both hypotheses would explain the results which look anomalous at first sight, further investigations are required to determine the appropriate explanation.

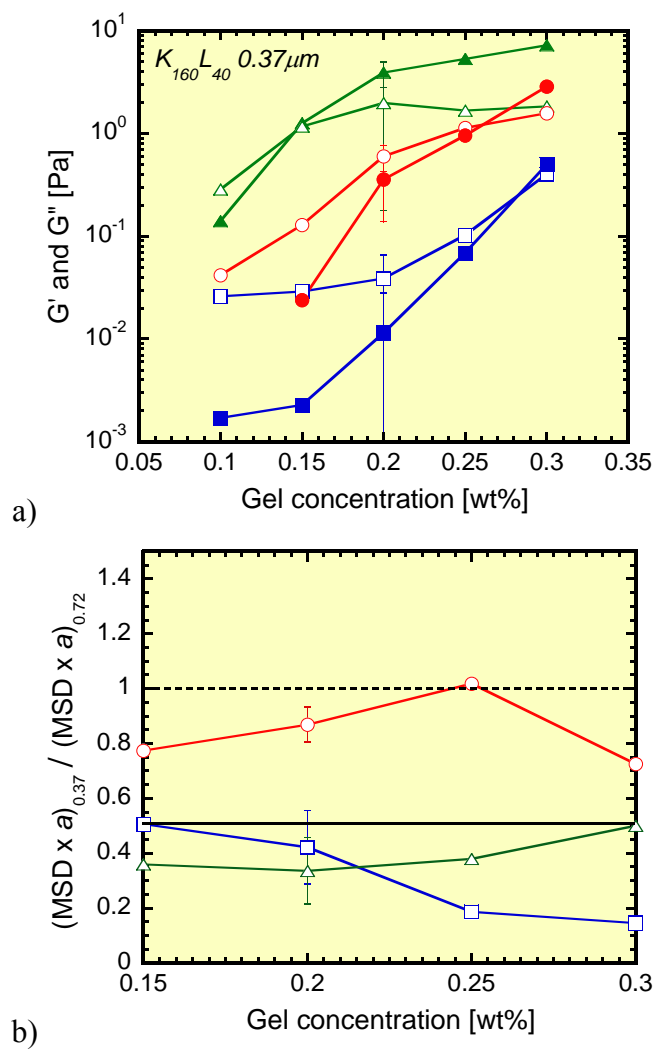


Figure 5.7 a) Gelation behavior with 0.37mm particles, and b) the effect of particle size on MSDs, at different concentrations.

5.4.2 REPETITIVE DIALYSIS AND RECOVERY AFTER BREAK-DOWN

Most experiments were performed with a single dialysis cycle. In order to study the effect of repeated dialysis cycles, we exposed a hydrogel sample with 0.15wt.% K₁₆₀L₄₀ to multiple solvent exchanges between DI water and 100mM NaCl. The repetitive dialysis steps each lasted 10min. The sample showed liquid-like behavior after the addition of salt, and formed a gel-like structure after salt removal (compare Fig. 5.8a with Fig. 5.1b). In subsequent dialysis cycles, the liquid state (with salt) was very reproducible, while the gel strength kept increasing during the experiment.

We reported in Chapter 4 that active, convective mixing with 100mM NaCl easily destroys the self-assembled microstructure of K₁₆₀L₄₀ hydrogels. This suggests another interesting hydrogel preparation scheme with potential relevance for practical applications as biomaterials. We destroyed 0.15 and 0.25wt.% K₁₆₀L₄₀ hydrogels by macroscopically mixing them with 100mM NaCl on a vortex mixer. The liquid sample was loaded into the dialysis cell and salt was removed by dialysis against DI-water. Upon salt removal, the tracer mobility (MSD) decreased significantly (Fig. 5.8b-c), which proved that the gel strength effectively recovered despite initially break-down by external shear stress. The gel strength increased further after a second dialysis cycle with NaCl and DI water, analogous to the observations in the repetitive dialysis test (Fig. 5.8a). At the slightly higher concentration (0.25wt.% K₁₆₀L₄₀), the response was similar to the 0.15wt.% gel, but the gel recovery occurred much more rapidly and the strengthening in the second dialysis cycle was minimal. This result is reasonable since one could expect that the gel fragments are able to find neighboring fragments more readily at higher BCP concentrations, so that a gel network is reformed more easily. In applications, one can imagine that a sample is prepared at elevated salt concentration and then injected to a location with lower salt concentrations in the surrounding tissue, so that a hydrogel can be formed in situ.

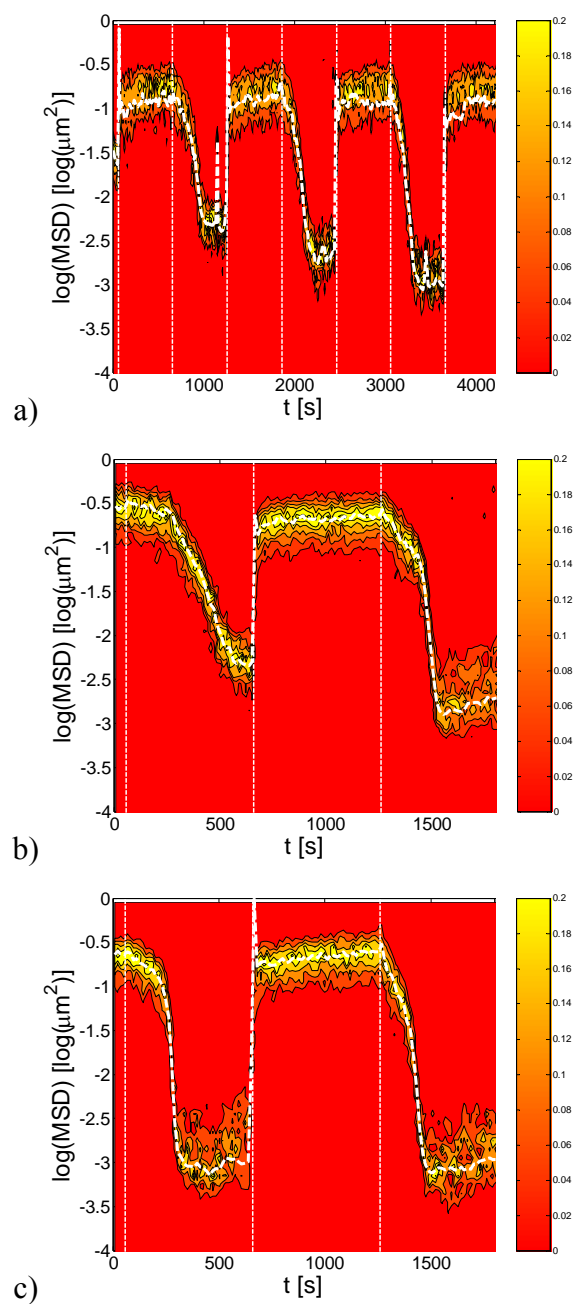


Figure 5.8 Contour plots of transient histograms of MSDs during a) a repeatability test with 0.15wt. % K₁₆₀L₄₀ Hydrogels, b) a recovery test with 0.15wt. % K₁₆₀L₄₀ Hydrogels, c) a recovery test with 0.25wt. % K₁₆₀L₄₀ Hydrogels

5.4.3 LAG TIME ANALYSIS

In practical applications, the response time of the hydrogels would be a key parameter during the optimization of performance and functionality. The responses of both $K_{160}L_{40}$ and $K_{180}L_{20}$ hydrogels to the addition of salt were very rapid, independent of gel concentration (see Figs. 5.1 and 2) and salt concentration (10-100mM NaCl). The response of the gels to removal of salt was noticeably slower and was analyzed quantitatively by fitting the transient MSD data to a sigmoidal function (see Fig. 5.9a). The response time of the sample was defined as the time between solvent switching and the time at which the MSD reached the halfway point between the initial and final plateau values. Fig. 5.9b contains the results of lag time as a function of concentration and 100mM NaCl for both BCPs. For $K_{160}L_{40}$ hydrogels the response time decreased as the gel concentration increased, which is reasonable because the gel network can quickly form at high concentrations, as was discussed in the previous section. The response time seems to asymptotically reach a minimum level of ca. 70s. From numerical calculations of the diffusion of NaCl in the dialysis cell, it was concluded that the NaCl concentration decreases to half of the initial concentration after ca. 40s dialysis against DI-water [98]. Therefore, we believe that the observed minimum lag time is the result of diffusion limitations in the dialysis cell, while at lower gel concentration the response is controlled by gel formation kinetics. For $K_{180}L_{20}$, again two distinct regimes are observed: a plateau at low BCP concentrations and a monotonic increase for more concentrated samples. Again, the plateau value seems to be caused by diffusion limitations: as soon as salt diffuse out of the gel, the networks break with little kinetic resistance. At higher concentrations, the structural rearrangements during break-up become hindered and a longer time is needed to break up the gel networks.

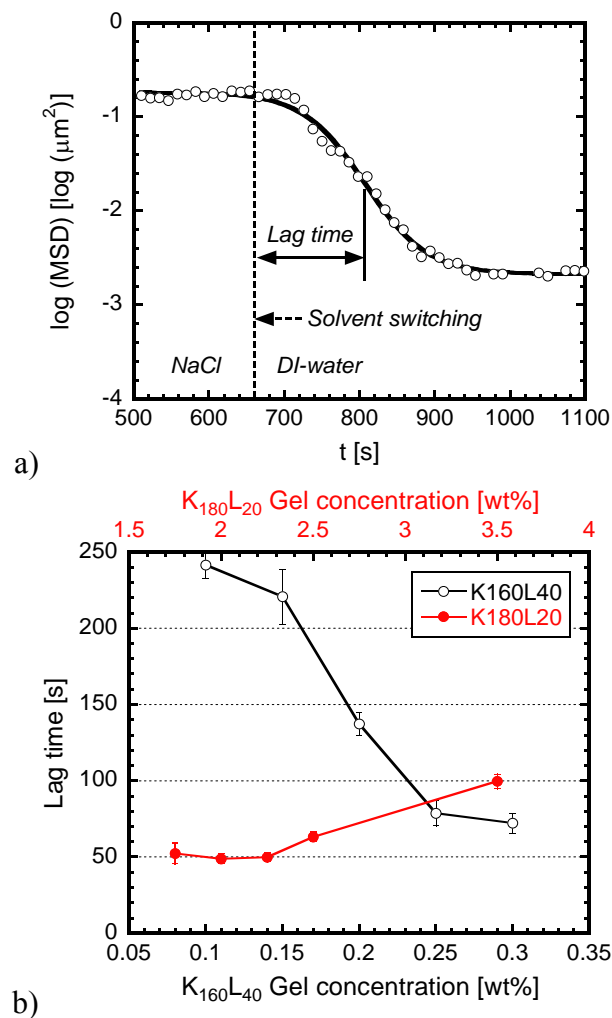


Figure 5.9 Lag time analysis. a) Example of a sigmoidal fitting curve for transition from salt-solution to DI water; the logarithmic half time was used to define the lag time. b) the effect of BCP concentration on the lag time for 100mM NaCl solutions.

5.5 CONCLUSIONS

We studied the microstructural changes of self-assembled block co-polypeptide hydrogels in response to changes in solvent ionic strength with particle tracking microrheology in a microdialysis cell. This dialysis cell mimics application environments in which solvent transport is governed by diffusion instead of convection, which is relevant for many biomaterials. The device provides unique insight into the evolution of microstructure and rheology in solvent responsive materials undergoing solvent exchange.

A systematic investigation was performed by varying hydrogel concentration, molecular architecture, salt concentration and tracer particle size. Experiments with a three step solvent exchange protocol (DI water \rightarrow NaCl solution \rightarrow DI water) results revealed that a slight difference in molecular architecture of the block copolypeptide, K₁₆₀L₄₀ vs. K₁₈₀L₂₀, dramatically affected the response of the hydrogel to changes in ionic strength. In many of the tests performed, the two samples reacted in opposite ways. While K₁₆₀L₄₀ weakens with increasing salt concentration and undergoes phase separations at microscopic and macroscopic length scales, K₁₈₀L₂₀ remains homogeneous and strengthens. Both materials show reversibility of gel strength and microstructure after removal of excess salt through dialysis. By employing different sizes of tracer particles, it was shown that heterogeneity strongly depends on the length scale at which the structure is probed and can be manipulated via salt and block copolypeptide concentrations. Since heterogeneity is crucial for controlling the transport of macromolecules and viability of cells, the tunability of the microstructure is of importance for potential tissue scaffold and drug delivery application.

CHAPTER 6

CONCLUDING REMARKS

6.1 CONCLUSIONS

The research described in this thesis has resulted in the following major achievements:

- A new microrheology set-up which enables quantitative measurements of transient rheological properties of solvent-responsive complex fluids, was designed and constructed by integrating particle tracking microrheology and microfluidics.
- A framework was developed for the quantitative analysis of transient microrheological experiments on homogeneous and heterogeneous samples.
- The dialysis cell and transient analysis methods were successfully employed to investigate liquid-gel transitions, viscosity transitions, and microstructural evolutions of various solvent-responsive complex fluids.
- It was found that diffusive solvent exchange can result in different microscopic structures than macroscopic addition and mechanical mixing for biomimetic block copolypeptide hydrogels. Since biotransport is often governed by diffusion, while traditional experiments require convective mixing during sample preparation, this discrepancy is highly relevant for the future evaluation of biomaterials.
- A systematic study of self-assembled block copolypeptide hydrogels provided unique insight into the microstructural evolution of these materials in response to changes in solvent ionic strength, which can be used for the optimization of these materials for biomedical applications.

These major achievements are described in more detail below.

6.1.1 DIALSYS CELL AND TRANSIENT PT μ R

A new microrheology set-up which allows us to quantitatively measure the transient rheological properties of solvent-responsive complex fluids was constructed by integrating particle tracking microrheology and microfluidics. The dialysis cell consists of a reservoir, porous dialysis membrane, and sample chamber. Solvent molecules can freely diffuse between the reservoir and the sample chamber while macromolecular sample components are trapped in the sample chamber with a rigid semipermeable dialysis membrane. The design enables manipulation of the solvent composition in the sample chamber by simply switching the fluid composition in the reservoir. Validation experiments for solvent diffusion in the dialysis cell showed good agreement with numerical solutions of the transport equations and confirmed that the solvent composition in a sample can be changed in a controlled and predictable fashion within a few minutes due to the small device dimensions. The solvent composition can be exchanged with no external force during solvent changes, which is suitable for applying fragile, solvent-responsive complex fluids. The instrument also allows us to study reversibility and repeatability, which cannot be performed with a conventional rheometer.

Guidelines for the optimum analysis parameters for transient experiments to accurately capture physical transitions were provided in view of trade-offs between temporal resolution and statistical validity. To understand spatial heterogeneity of heterogeneous samples, it is necessary to analyze histograms of individual particle displacements as well as monitoring a non-Gaussian parameter. Careful evaluation of different averaging methods to determine a meaningful ensemble average for heterogeneous and homogeneous sample led to the conclusion that a weighted average of the properties of individual particles, using the trajectory length as weighing factor was the preferable method. It was also found that the difference between the all particle analysis and the weighted individual particle analysis can be used as an indicator of

sample heterogeneity. We discussed algorithms to obtain transient dynamic moduli for heterogeneous samples and proposed the calculation of rheological quantities for individual tracer trajectories before determining the weighted average of this distribution.

The study resulted in the first report of transient dynamic moduli for heterogeneous samples as measured with particle tracking microrheology.

6.1.2 APPLICATIONS OF DIALYSIS CELL AND TRANSIENT $PT_{\mu R}$

As an example of applications for this new device and methods, we successfully quantified several solvent-induced rheological transitions: the liquid-gel transition of sodium alginate solutions due to the addition of divalent cations, melting of these gels after addition of chelating agents, and changes in viscosity of polyelectrolyte solutions as a function of ionic strength. For these homogeneous samples, the rheological transitions could be measured with high temporal resolution, and complex solvent exchange protocols could be performed, involving of multiple solvents and reversible steps. The experiments highlighted the ability of the dialysis cell to investigate the kinetics of the molecular processes that are responsible for the observed changes in mechanical properties.

As heterogeneous samples, we investigated self-assembled solvent-responsive block copolypeptide (BCP) hydrogels, and their rheological properties and heterogeneity were successfully quantified. Moreover, the microstructural changes were qualitatively visualized with confocal microscopy. We have shown that solvent exchange via convective mixing and dialysis can lead to significantly different hydrogel properties and that commonly applied sample preparation protocols for the characterization of soft biomaterials could lead to erroneous conclusions about microstructural dynamics. It was also found that the transient responses in rheology and heterogeneity were fully reversible and that the breakdown of BCP hydrogels due to mechanical mixing after the addition of

salt can be also reversed upon dialysis, which can potentially be used for *in vivo* gel injection and gentle mixing of living cells into hydrogels.

A systematic investigation of the salt-responsiveness of BCP hydrogels revealed that slight difference in molecular structure can dramatically change the transient salt responses of hydrogel rheology and microstructure. We found that the heterogeneity significantly increased as the probing length scale decreased and that heterogeneity can be controlled by changing salt and gel concentrations. A quantitative lag time analysis showed that the methodology can be used to study network formation and breakup kinetics for these heterogenous self-assembled materials..

The research has proven that the dialysis cell is a useful and versatile tool to study the response of a wide variety of solvent-responsive complex fluids, including reversible and repetitive changes in solvent composition. The methodology facilitates the design of gels with appropriate microstructural dynamics for *in vivo* applications like tissue engineering and drug delivery, and can also be applied to study the effect of solvents on self-assembly mechanisms in other responsive soft materials, such as polymer solutions and colloidal dispersions.

6.2 RECOMMENDATIONS

6.2.1. GEL FORMATION AND BREAK-UP KINETICS OF SODIUM ALGINATE

Sodium alginate hydrogels have been widely used as immobilization matrix for living cells [65, 117] since a pioneering microencapsulation technique was introduced by Lim and Sun [118]. With their method, alginate hydrogel beads are generated by dropping sodium alginate solution into a CaCl_2 solution and subsequently covered with a poly-L-lysine coating which acts as a biocompatible semipermeable membrane. For liquid core capsules, the alginate hydrogel core is finally liquefied by applying a

chelating agent that removes the Ca^{2+} ions embedded in crosslinks. Gel formation mechanisms of an alginate gel was studied by Skjak-braek *et al.* and they observed an inhomogeneous concentration profile of calcium alginate within a gel cylinder [119]. Based on these experiments, they constructed a diffusion controlled gelation model in order to explain the inhomogeneity, assuming that gelation kinetics is very fast [120]. Chrastil generated calcium salt solution beads covered with an alginate gel shell and obtained rate constants, diffusion coefficient and activation energies from time dependent shell thickness profiles by fitting the data to a binomial diffusion equation: $L = L_{\max} [1 - \exp(-kt)]^n$ [121], where k and n are rate constants and L is the shell thickness. Blandino *et al.* applied a peristaltic pump to generate calcium salt solution beads with alginate shell, and investigated the effect of sodium alginate and CaCl_2 concentration on gelation kinetics by obtaining the constants n and k , of the above equation from the time dependent shell thickness [122]. In both methods, however, the effect of dimensions of beads and diffusion of sodium alginate and Ca^{2+} were not mentioned. Hassan *et al.* measured time-dependent concentration profiles of residual metal ions in the reservoir in which alginate hydrogels were formed and evaluated rate constants of gelation kinetics by adopting a two-step reaction expression: $C_t - C_\infty = B_0 e^{-R_f t} + P_0 e^{-R_s t}$, where C is the concentration of metal ion, R_f and R_s are the first-order rate constants for the fast and slow gelation steps, B_0 and P_0 initial concentration at each steps [123]. The challenging point is to extract only the kinetics of gel formation since the gel formation process involves both diffusion and kinetics. Therefore, few studies on the kinetics have been reported, although understanding gel formation kinetics of calcium alginate hydrogels is essential for optimizing chemical and mechanical properties of the capsules [124]. Moreover, gel break-up kinetics has not been investigated so far.

In section 2.5.1, we demonstrated microrheological measurements of sodium alginate solution during gel formation and break-up in response to solvent changes. The

results with two different CaCl_2 concentrations revealed that the response curves are very sensitive to the balance between reactants.

Preliminary transient measurements were performed over a wide range of CaCl_2 concentrations: 0.0277-1.11wt.%. Figure 6.1 shows step response curves after changing the solvent from DI water to solutions of different CaCl_2 concentration. As the CaCl_2 concentration in the reservoir flow increases, the lag time decreases, which is reasonable: the more calcium is supplied, the faster the alginate gel is formed (also see Fig. 6.2). As was used in Chapter 5, the characteristic quantities of the response curves were extracted with a sigmoidal fitting curve, in which all fitting parameters have a clear physical relevance: $\log_{10}(MSD) = A + B/(1 + \exp(-(t - t_l)/\tau_l))$, where A is the initial MSD, B is the stepsize of a drop or rise of the MSD (depending on the sign of B), t_l is the lag time between flow switching and observed changes in MSD, and τ_l is the characteristic timescale of the MSD response.

The results in Fig. 6.2, which presents the lag time for both gel formation and break-up as a function of CaCl_2 concentration, indicate that the gel formation process was governed by diffusion. In the gel break-up process, on the other hand, two distinctive regimes were found; for low CaCl_2 concentrations, the lag time is independent of CaCl_2 concentration, while it monotonically increases once the CaCl_2 concentration increases past a threshold value. The constant lag time in dilute CaCl_2 solutions suggests that the gel break-up process is governed by chelation kinetics of calcium ions embedded in the gel: incoming citrate ions wipe up free calcium ions in solution very rapidly and subsequently start to chelate the calcium ions embedded in the gel, which is the limiting factor in the chelation process. At high CaCl_2 concentration, chelation of the free calcium ions is no longer negligible because the calcium concentration is comparable to the citrate concentration. The increasing time lag at high CaCl_2 concentration thus suggests that gel break-up is governed by both diffusional supply of citrate and chelation kinetics.

The lag time curves of Fig. 6.2 are expected to be a function of sodium alginate and sodium citrate concentration due to a shifting balance between kinetics and diffusion. In particular, the plateau lag time and the bending point in the break-up curve relate to the competition between kinetics and diffusion. Therefore, we should be able to develop a better understanding of the kinetics of alginate gel formation and to find rate constants of gel formation and gel break-up based on observed shifting behavior of the lag time curves with different concentrations of sodium citrate and sodium alginate.

Based on the results of the numerical calculations in Chapter 2, the total moles of calcium ions supplied to specific locations in the chamber can readily be calculated as a function of time. As a result, by taking into account the effects of sodium alginate, sodium citrate and calcium ions on the lag time, a full kinetic model for the gel formation and gel break-up could be constructed and validated with the dialysis cell.

Additional measurements should be carried out at different alginate concentrations (0.1 - 1 wt.%) and as a function of sodium citrate concentration (0.11 – 2.2 wt.%).

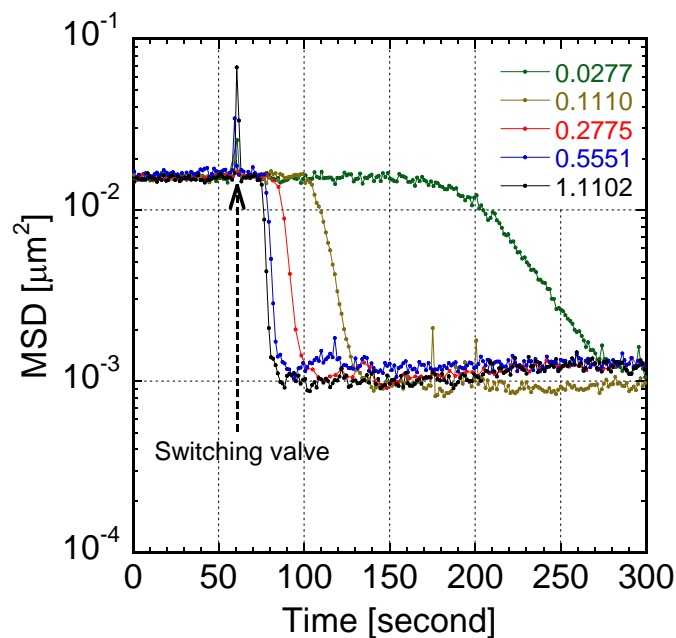


Figure 6.1: Step response curves of MSD ($\tau = 0.033\text{s}$) for solutions of 0.25wt.% sodium alginate after changing solvent from 150mM NaCl solution to various CaCl_2 concentrations; solvent composition was changed at $t = 60\text{s}$.

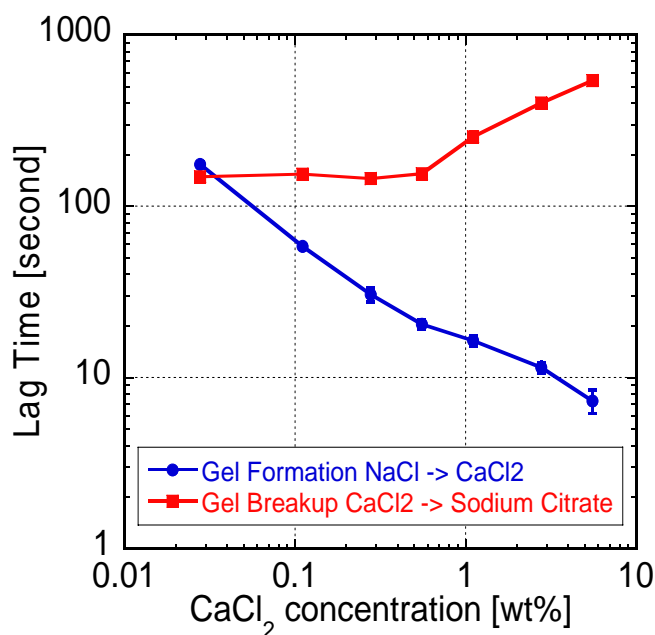


Figure 6.2: Time lag for alginate gel (0.25wt.%) formation and gel break-up function of CaCl_2 concentration; sodium citrate concentration during break-up was kept constant at 75mM.

6.2.2. HIGH THROUGHPUT SCREENING ⁵

6.2.2.1 Current limitations

For the traditional rheological characterization of solvent-responsive materials at a particular solvent composition with mechanical rheometers, a sample must be mixed after the solvent composition is changed, loaded into the test geometry of the rheometer, and rested before a measurement can be taken. Thus, it takes at least an hour to measure the mechanical properties for each sample. When the rheology of the same sample needs to be determined at different solvent compositions, the total measurement time becomes extremely long (more than a day). Furthermore, the total required sample volume becomes large since samples must be prepared independently at each solvent composition. This is disadvantageous for samples whose properties are time-dependent and for materials that are not available in sufficient amount, *e.g.* purified biomaterials and output from high-throughput synthesis.

To overcome these difficulties, devices for high-throughput rheology have recently been invented [125-135]. However, they primarily provide viscosity data of a sample and the required sample volumes are still greater than 1 ml. In the past, Breedveld & Pine reported a high-throughput screening method for rheology measurement by using particle tracking microrheology [24]. This method allows us to perform 300 measurements per day instead of 5-10 measurements with a mechanical rheometer. However, sample preparation is still the time-consuming step and one needs

⁵ U.S. Patent Application:
Sato, J. and Breedveld, V. "Device for High-Throughput Characterization of Solvent-Responsive Materials", Patent Pending (GTRC proprietary #3676)

about a hundred micro-liter of sample per measurement, so that the total sample volume can still be prohibitively large for screening a large number of samples.

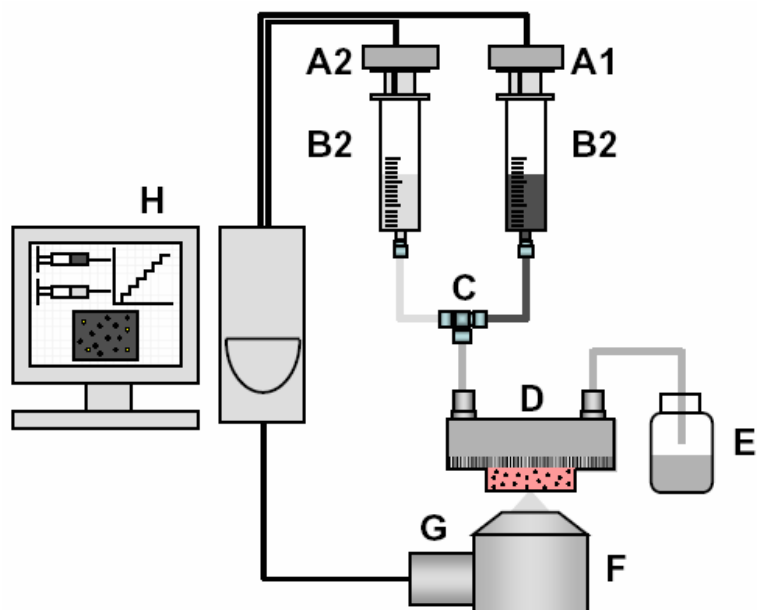
6.2.2.2 Concept

The high-throughput device we invented here primarily consists of a dialysis cell, optical microscope, syringe pumps, micromixer, and PC for instrument control and data analysis. In Chapter 2, we constructed a new dialysis cell for microrheology set-up that allows us to rapidly manipulate solvent composition and to measure the transient rheological properties and morphology of complex fluids during solvent changes by integrating microrheology and microfluidics. With this dialysis cell, the solvent composition in a macromolecular sample can be changed in a stepwise fashion within tens of seconds, rather than in hours as was the case with a mechanical rheometer. By choosing a porous dialysis membrane with the desired selectivity, one can apply the dialysis cell to a wide variety of complex fluids, not limited to cross-linked gels.

The schematic illustration of the high throughput device is shown in Fig. 6.3. Syringe pumps and a micromixing tee are connected upstream of the dialysis cell. The outlets of the syringe pumps are connected to the micromixer inlets, and the outlet of the mixer is connected to the dialysis cell inlet. The syringe pumps are controlled with PC and the flow rate of the syringes are controlled individually in a programmed manner so that the composition of the mixer outlet flow (and dialysis cell inlet) can be manipulated. Probe particles are premixed in the sample for particle tracking microrheology. The dialysis cell is mounted on an inverted microscope and movies are recorded with videomicroscopy. One can monitor particle motion during and after the rapid solvent changes within tens of seconds. By converting the particle motion to rheological properties, one can rapidly measure rheology of samples at a particular solvent composition. For high-throughput screening, the following operation steps are repeated: (1) change solvent composition via syringe pumps and mixer (within tens of seconds), (2)

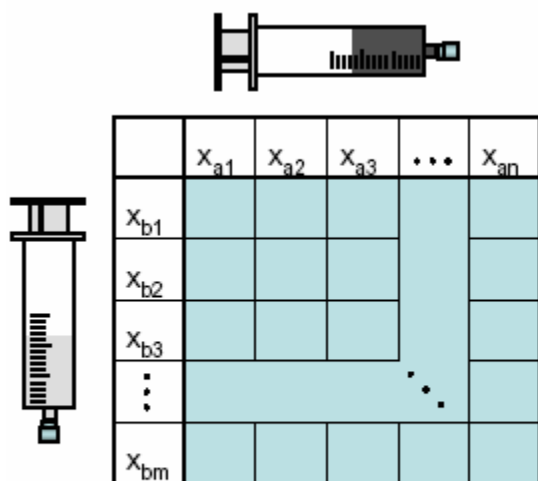
take a movie of tracer particle motion (within tens of seconds), and (3) calculate sample rheology (a few minutes) via image analysis. Thus, the device speeds up the data collection by a factor of ~ 30 , compared to macroscopic measurements with a rheometer. Furthermore, the measurements and analysis can be automated with PCs.

With the device, one can rapidly measure the microstructure, phase behavior and rheology of salt/pH responsive materials at a desired solvent composition, salt concentration or pH, within several minutes for very small sample volumes (less than 1 micro-liter). As a further application of this device, by combining a number of stepwise solvent changes and/or implementing complex sequences of solvent composition, we can easily test the reversibility of the sample response. Another application is to use multiple syringes to manipulate the complex solvent composition of a sample and rapidly screen samples in a multidimensional phase space of sample composition (Fig. 6.4).



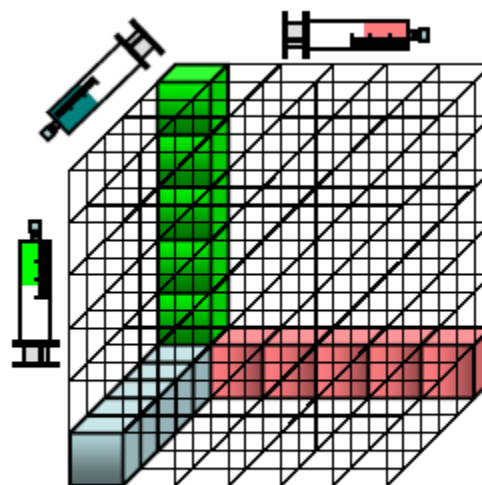
- A1 . Syringe pump 1
- A2 . Syringe pump 2
- B1 . Syringe 1
- B2 . Syringe 2
- C . Mixing tee
- D . Dialysis cell
- E . Drain tank
- F . Fluorescent microscope
- G . CCD camera
- H . PC

Figure 6.3: Schematic illustration of High-Throughput Characterization Device of solvent responsive complex fluids



With two syringes

a)



With three syringes

b)

Figure 6.4: Examples of concentration array: a) two dimensional and c) three dimensional libraries.

6.2.3. TRANSPARENT DIALYSIS CELL

The microchannels of the dialysis cell in Chapter 2 were fabricated on a silicon wafer via photolithography techniques (Fig. 6.5). The dialysis cell was mounted onto an inverted microscope, and the fluorescent mode was used for microrheology measurements. Because the silicon wafer is not transparent, bright field microscopy cannot be used. Thus, the samples need to be visible under fluorescent light: *e.g.* fluorescent tracer particles, or dyes and other fluorescently labeled molecules. To apply the dialysis cell for a wide variety of complex fluids including non-fluorescent materials, it is required to construct the microchannels in a transparent material, such as glass or PDMS (polydimethylsiloxane). Glass would be the most desirable material due to its rigidity and optical transparency. However, fabricating the exact dimension of microstructures in glass is rather complicated. On the other hand, PDMS is widely used in soft lithography because of simple fabrication processes, rapid production and low cost. Attention must be paid upon employing PDMS instead of silicon wafer. Since PDMS is a soft material, the softness must be controlled by sample preparation. For assembling the PDMS channel structure, dialysis membrane, and coverslip, we would need to carefully select glue, considering surface chemistry of PDMS. The connector ports used for silicon wafer cannot be used because of the PDMS flexible surface. Good tubing connections might be achieved by directly piercing relatively stiff tubing into PDMS.

The transparent dialysis cell can be immediately used for observing phase behavior of pH responsive colloidal crystals, colloid aggregation and dispersion dynamics, formation of emulsion droplets under the different solvent conditions. For biomedical applications, we could for example observe deformation, rouleaux formation, and hemolysis of red blood cells in solutions of different ionic strength.

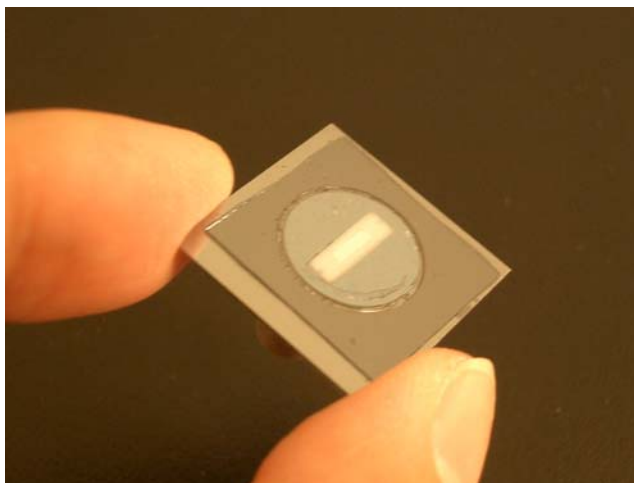


Figure 6.5: An image of the dialysis cell with a silicon wafer.

APPENDIX A

IDL CODES FOR TRANSIENT ANALYSIS OF HETEROGENEOUS

METDIA

A.1 TRANSIENT HETEROGENEITY

```
; ALPHA_IND.pro
; by Jun Sato, Georgia Tech, Dec 2005
;
; Calculate the quantified inhomogeneity parameter,
;  $\text{Alpha} = \langle \text{dy}^4 \rangle / 3 \langle \text{dy}^2 \rangle^2 - 1$ 
; Eric Weeks et al. Science, 287, p627-631 (2000)
;
; EXAMPLE:
;
alpha,'20051218_D6A2_100_SS125',dt=10,dim=2,binsize=0.5,int=0.2,ini=0,tot=21,disp
=40
;
; MODIFICATION HISTORY
; -Modified from ALPHA.pro (JunSato GTech 11/2005)
; 2/7/2006 Jun Sato @ Georgia Tech
; displacement calculation is the summation method.
;  $\langle r^{2n} \rangle = 1/N * \text{sum}(r(t)-r(0))^{2n}$ 
; see Rahman A., Physical Review 136,2A(1964)
; - Output of number of trajectories, JunSATO 7/29/2006

pro alpha_ind,name,dir=dir,dt=dt,dim=dim,binsize=binsize,int=int,ini=ini,tot=tot,$
disp=disp,smt=smt,maxalpha=maxalpha

if not keyword_set(dt) then dt=10
if not keyword_set(dim) then dim=2
if not keyword_set(binsize) then binsize=0.5
if not keyword_set(int) then int=0.5
if not keyword_set(ini) then ini=0
if not keyword_set(tot) then tot=21
if not keyword_set(disp) then disp=10
if not keyword_set(dir) then dir = ""
if not keyword_set(smt) then smt = 10
if not keyword_set(maxalpha) then maxalpha = 5

filen = findfile(dir+name+'_trm.gdf')
filen = filen(sort(filen))
if filen(0) eq "" then message,"No file '"+name+"' found"
```

```

trm=read_gdf(filn)

num=tot/int
ini=int/2
tddx=FLTARR(num+1,2/binsize*disp+1)
tddy=FLTARR(num+1,2/binsize*disp+1)
pdfs=FLTARR(3,num)
n_trj=make_array(2,num)
for i=1,disp*2/binsize+1 do begin
    tddx(0,i-1)=-disp+binsize*(i-1)
    tddy(0,i-1)=tddx(0,i-1)
end
maxtrm=max(trm(5,*))
for i=1,num do begin
    print,'                               Time Slice # =' + string(i) + '/' + string(num)
    if (((i-(0.5))*int+ini)*30*60 lt maxtrm) then begin
        if (((i+(0.5))*int+ini)*30*60 lt maxtrm) then begin
            trma=eclip(trm,[5,((i-(0.5))*int+ini)*30*60,((i+(0.5))*int+ini)*30*60])
        endif else begin
            trma=eclip(trm,[5,((i-(0.5))*int+ini)*30*60,maxtrm])
        endelse
        pdf = mkpdf(trma,dt,dim=dim)
        pdfs(0,i-1)=((i-1)*int+ini); *60*30
        plot_hist,pdf(0,*),/fit,/log,nombre=name,binsize=binsize,xrange=[-disp+binsize,disp-
        binsize],yrange=[1e-6,1],/normalize; was eliminated
        ;plot_hist,pdf(0,*),/fit,/log,nombre=name,/normalize,xrange=[-disp+binsize,disp-
        binsize],yrange=[1e-6,1]
        bx=readtext(dir+name+'_Histogram.txt')
        plot_hist,pdf(1,*),/fit,/log,nombre=name,binsize=binsize,xrange=[-disp+binsize,disp-
        binsize],yrange=[1e-6,1],/normalize; was eliminated
        ;plot_hist,pdf(1,*),/fit,/log,nombre=name,/normalize,xrange=[-disp+binsize,disp-
        binsize],yrange=[1e-6,1]
        by=readtext(dir+name+'_Histogram.txt')
        smx=pdf(0,*)
        smy=pdf(1,*)
        smx2=smx^2
        smy2=smy^2
        smx4=smx^4
        smy4=smy^4
        smx2m=total(smx2)/n_elements(smx2)
        smx4m=total(smx4)/n_elements(smx4)
        smy2m=total(smy2)/n_elements(smy2)
        smy4m=total(smy4)/n_elements(smy4)
        ;pdfs(1,i-1)=(smx4m/(smx2m^2)/5)-3/5 ;J.Phys:Condens.Matter 17 (2005) S4035-46
        ;pdfs(2,i-1)=(smy4m/(smy2m^2)/5)-3/5 ;J.Phys:Condens.Matter 17 (2005) S4035-46
        pdfs(1,i-1)=(smx4m/(smx2m^2)/3)-1 ;Eric's science

```



```

pdfs(2,i-1)=(smy4m/(smy2m^2)/3)-1 ;Eric's science
tddx(i,*)=bx(1,*)
tddy(i,*)=by(1,*)

n_trja= trma(6,*)
uni_tr= n_elements(smx(0,*));n_trja[UNIQ(n_trja, SORT(n_trja))]
n_trj(0,i-1)= (i-1)*int+ini
n_trj(1,i-1)=uni_tr ; max(uni_tr)-min(uni_tr)+1
endif
endfor
;print,pdfs
w=where(pdfs(1,*) ne 0)
pdfs=pdfs(*,w)
w=where(pdfs(1,*) lt maxalpha)
pdfs=pdfs(*,w)
print,pdfs
write_gdf,pdfs,dir+name+'_TransAlpha.gdf'
write_text,pdfs,dir+name+'_TransAlpha.txt'
write_text,tddx,dir+name+'_TransDispDist_x.txt'
write_text,tddy,dir+name+'_TransDispDist_y.txt'
write_text,n_trj,dir+name+'_n_trajectories.txt'
print,'done'

end

```

A.2 TRANSIENT MSDS, SLOPES, AND MODULUS

```

function trans_modulus,filename,int=int,tot=tot,dia=dia, $
mintau=mintau,maxtau=maxtau,minN=minN,minmsd=minmsd,maxmsd=maxmsd, $
minslp=minslp,maxslp=maxslp,Dt=Dt,timestep=timestep,mpp=mpp,temp=temp,dim=di
m,weigh=weigh, $
isostress=isostress

;TRANS_MODULUS by JunSATO, June 2006
;Transient G' & G'' Distribution
;Individual particle analysis
;
;Use Generalized Einstein-Stokes Equation
;(algebraically transformed)
;Mason TG, Rheol. Acta,39,371-378(2000)
;
;OUTPUT
;-AVEALL = Average quantities
;=
<time><MSD><logMSD><Slope><logSlope><Gs><logGs><Gp><logGp><Gpp><log
Gpp><#Trajectory>

```

```

; -array@ (*,*,0) = Histogram of @
; = <grid><counter> Note: # of column = # of time slices
; -array@ (*,*,1) = Normalized Histogram of @
; = <grid><fraction> Note: # of column = # of time slices
;
;EXAMPLE
;a=trans_modulus('20060122_L6E2',int=1,tot=21,maxtau=6,mintau=3,maxmsd=0,minms
d=-5,
;maxslp=1.5,minslp=-
0.5,minN=5,Dt=2,mpp=0.0988,timestep=1/30.,temp=296.65,dia=0.72,dim=2,/weigh)
;
;INSTRUCTION
; int: mini-movie length [min]
; tot: total length of movie [min]
; maxtau: maximum tau value [frame]
; mintau: minimum tau value [frame]
; ->transient msd is at roundup((maxtau+mintau)/2) [frame]
; e.g. mintau3, maxtau=6-> MSD=5
; minmsd, maxmsd: cut-off line for anomalous MSDs [log(MSD)]
; minslp, maxslp: cut-off line for anomalous Slopes [-]
; ->Note that slope<-1 cannot be accepted in gamma function
; minN: minimum acceptable # of contribution
; dia: particle diameter
;
;MODIFICATION HISTORY
;-eliminate Gp=0d and Gpp=0d, JunSATO 6/28/06
;-eliminate Slope=0d, JunSATO 6/28/06
;-"weigh" was added Jun Sato 8/7/06
; Gs, Gp, and Gpp, are weighted by n: trajectory length [frame number]
; weigh=1 ON
; weigh=0 OFF
;-"weigh" was implemented Jun Sato8/24/06
;
;COMMENT
; -#Particles=counter2 JunSATO 7/29/06
; counter2: number of trajectories satisfied minN
; Thus, total contribution of independent trajectories = counter2 x minN !!!
;

if not keyword_set(int) then int=0.25
if not keyword_set(tot) then tot=21
if not keyword_set(maxtau) then maxtau=5
if not keyword_set(mintau) then mintau=2
if not keyword_set(maxmsd) then maxmsd=0
if not keyword_set(minmsd) then minmsd=-5
if not keyword_set(maxslp) then maxslp=1.5

```

```

if not keyword_set(minslp) then minslp=-0.5
if not keyword_set(minN) then minN=2
if not keyword_set(Dt) then Dt=2
if not keyword_set(mpp) then mpp=0.0988
if not keyword_set(timestep) then timestep=1/30.
if not keyword_set(temp) then temp = 290D ; approx. 17 degC
if not keyword_set(dia) then dia = 0.5D ; Diameter in microns
if not keyword_set(dim) then dim=2
if not keyword_set(weigh) then weigh=0
if not keyword_set(isostress) then isostress=1

```

```

kB = 1.38065d-23      ; MKS

```

```

gmax=50
gmin=-1
gbin=10

```

```

maxgs =gmax
mings =gmin
maxgp =gmax
mingp =gmin
maxgpp=gmax
mingpp=gmin
binmsd=10 ;
binslp=20 ;
bings =gbin ;
bingp =gbin ;
bingpp=gbin ;

```

```

OPENW,1, filename+'_parameters.dat'
PRINTF,1, 'General
Parameters:int,tot,maxtau,mintau,maxmsd,minmsd,maxslp,minslp,maxgs,mings,maxgp,
mingp,maxgpp,mingpp,binmsd,binslp,bings,bingp,bingpp,minN,Dt,mpp,timestep,Temp,d
ia,dim,weigh'
printf,1,int,tot,maxtau,mintau,maxmsd,minmsd,maxslp,minslp,maxgs,mings,maxgp,ming
p,maxgpp,mingpp,binmsd,binslp,bings,bingp,bingpp,minN,Dt,mpp,timestep,temp,dia,di
m,weigh
CLOSE,1

```

```

;***File Read***
trmname=filename+'_trm.gdf'
trm=read_gdf(trmname)

```

```

;***Output Array***
num=tot/int ;# of data column
ini=int/2

```

```

arraymsd=make_array(num+1,binmsd*(maxmsd-minmsd),2);MSD histogram,
normalized histogram
arrayslp=make_array(num+1,binslp*(maxslp-minslp),2);SLOPE
arraygs=make_array(num+1,bingp*(maxgs-mings),2);G
arraygp=make_array(num+1,bingp*(maxgp-mingp),2);G'
arraygpp=make_array(num+1,bingpp*(maxgpp-mingpp),2);G''
timef=make_array(num);time segment [frame]
times=make_array(num);time segment [second]
;<time><MSD><logMSD><Slope><logSlope><Gs><logGs><Gp><logGp><Gpp><log
Gpp><#Particles>
aveall=make_array(12,num)

for i=1,num do begin
    timef(i-1)=((i-1)*int+ini)*30*60
    times(i-1)=((i-1)*int+int)*60
endfor
aveall(0,*)=times

;***Minimovies for Transient***
tlen=0;summation of length of all trajectories
for i=1,num do begin
    tlen=0;summation of length of all trajectories
    print,i
    trma=trm
    if (timef(i-1) lt max(trm(5,*))) then begin
        if ((timef(i-1)+int*30*60/2) gt max(trm(5,*))) then begin
            trma=eclip(trma,[5,timef(i-1)-int*30*60/2,max(trm(5,*))])
        endif else begin
            trma=eclip(trma,[5,timef(i-1)-int*30*60/2,timef(i-1)+int*30*60/2])
        endelse
    endif

;***Data Processing***
counter=n_elements(uniq(trma(6,*))) ;# of particles
t_uni=uniq(trma(6,*)) ;particle ID
device,decomposed=0
tek_color
window,0,xsize=225,ysize=180,title='MSD vs Tau',xpos=350,ypos=0
msdi=make_array(2,counter)
slpi=make_array(2,counter)
gsi=make_array(2,counter)
gpi=make_array(2,counter)
gppi=make_array(2,counter)
msdiw=make_array(2,counter)
slpiw=make_array(2,counter)
gsiw=make_array(2,counter)

```

```

gpiw=make_array(2,counter)
gpwi=make_array(2,counter)
counter2=0 ;ACTIVE trajectory ID
for j=0,counter-1 do begin ;actually i = counter2
  w=where(trma(6,*) eq trma(6,t_uni(j)))
  s=size(w)
  if (s(0) ne 0) then begin
    msdi(0,counter2)=1.0 ;switch on!
    slpi(0,counter2)=1.0
    gsi(0,counter2)=1.0
    gpi(0,counter2)=1.0
    gpwi(0,counter2)=1.0
    trmai=trma(*,w)
    res1=0
    if (n_elements(trmai(0,*)) ge 5) then begin ;factor 5
      res=msd_vb(trmai,minN=minN,micperpix=mpp,timestep=timestep, $
        mydts=indgen(maxtau)+1),,erode=1) ;trm->rrm

      ;***MSD***
      if (n_elements(res(0,*)) ge mintau) then begin
        msdi(1,counter2)=alog10(res(5,round((mintau+maxtau)*0.5)))
      endif else begin
        msdi(1,counter2)=minmsd-1 ;eliminate short trajectories
      endelse
      if (alog10(msdi(1,counter2)) gt maxmsd) then begin
        msdi(1,counter2)=10
      endif
      if (alog10(msdi(1,counter2)) lt minmsd) then begin
        msdi(1,counter2)=10
      endif
    endif

    ;***Slope***
    ;res1=an active "rrm" array of active particle trajectory
    if (n_elements(res(0,*)) ge maxtau) then begin
      res=res(*,where((res(0,*)/timestep) ge mintau))
      res=res(*,where((res(0,*)/timestep) le maxtau))
      res1=res
    endif else begin
      if (n_elements(res(0,*)) ge mintau+4) then begin ;at least 4 data points
        res1=res(*,where((res(0,*)/timestep) ge mintau))
      endif
    endelse
    ;Plot active trajectories
    if (counter2 eq 0) then begin
      plot,res1(0,*),res1(5,*),xtitle='tau [s]',ytitle='MSD [um^2]', $
        psym=0,/ylog,yrange=[0.0001,1], /xlog, xrange=[0.01,100]
    endif
  endif
endfor

```

```

endif else begin
    oplot,res1(0,*),res1(5,*),psym=0
endelse
;Linear Fitting
sr=size(res1)
X=alog10(res1(0,*))
Y=alog10(res1(5,*))
measure_errors =0.01/Y
go=0
for g=1,n_elements(Y) do begin
    if ((Y(g-1) gt -10) AND (Y(g-1) lt 10)) then begin ;normal if |MSDs|<10^+/-10
        go=go+1
    endif
endif
endfor
if (go eq n_elements(Y)) then begin ;if all MSDs are normal, then let's fit!
    fita=linfit(X,Y,MEASURE_ERRORS=measure_errors,/double)
    slpi(1,counter2)=fita(1)
endif

;***G***
am=double(dia*0.5)*1d-6      ; convert microns to meters
dt=reform(res1(0,*))
omega=1d/double(dt)
msdm=reform(res1(5,*))*1d-12  ; convert msd to meters
C=dim*kB*temp/(3!*pi*am)      ; multiply by the dimensionality/3.
foo=(!pi/2d)-1d              ; a handy constant
gsi(1,counter2)=C/(10^(msdi(1,counter2))*1d-12*gamma(1d+slpi(1,counter2)))
gpi(1,counter2)=gsi(1,counter2)*cos(!pi*slpi(1,counter2)/2d)
gppi(1,counter2)=gsi(1,counter2)*sin(!pi*slpi(1,counter2)/2d)

msdiw(1,counter2)=msdi(1,counter2)*(n_elements(trmai(1,*))/100);^0.5
slpiw(1,counter2)=slpi(1,counter2)*(n_elements(trmai(1,*))/100);^0.5
gsiw(1,counter2)=gsi(1,counter2)*(n_elements(trmai(1,*))/100);^0.5
gpiw(1,counter2)=gpi(1,counter2)*(n_elements(trmai(1,*))/100);^0.5
gppiw(1,counter2)=gppi(1,counter2)*(n_elements(trmai(1,*))/100);^0.5
tlen=tlen+(n_elements(trmai(1,*))/100);^0.5

;<eliminate unreasonably calculated values>
if (((gpi(1,counter2) eq 0d) OR (gppi(1,counter2) eq 0d) OR (slpi(1,counter2) eq
0d)) then begin
    ;slpi(1,counter2)=-10
    gpi(1,counter2)=-10
    gppi(1,counter2)=-10
end

endif

```

```

        counter2=counter2+1
    endif
    print,'Processing...(' +string(counter2)+'/'+string(counter)+')
endfor
endif
print,'Finished'
print,'The number of qualified MSD = ' +string(counter)

;***Histograms***
wmsd=maxmsd-minmsd
wslp=maxslp-minslp
wgs =maxgs -mings
wgp =maxgp -mingp
wgpp=maxgpp-mingpp

;<MSD>array
a=maxmsd
b=minmsd
bin=binmsd
histxmsd=((dindgen(bin*(a-b))+b*bin)/(bin)) ;histogram x data
histymsd=make_array(bin*(a-b))
avemsd=make_array(bin*(a-b))
avesummsd=make_array(bin*(a-b))
gridminmsd=make_array(bin*(a-b))
gridmaxmsd=make_array(bin*(a-b))
avemsd=0
avemsdb=0
avesummsd=0
avemsdw=0
avemsdbw=0
for k=1,bin*(a-b) do begin
    gridminmsd(k-1)=(double(k)-1)/double(bin)+b
    gridmaxmsd(k-1)=double(k)/double(bin)+b
    for m=1,counter do begin
        if (msdi(1,m-1) ge gridminmsd(k-1)) AND (msdi(1,m-1) lt gridmaxmsd(k-1)) then
begin
            if (msdi(1,m-1) ne 0d) then begin
                histymsd(k-1)=histymsd(k-1)+msdi(0,m-1)
                avemsd =avemsd+ (msdi(1,m-1)) ;log average
                avemsdb=avemsdb+10^(msdi(1,m-1)) ;linear average
                avemsdw=avemsdw+ (msdiw(1,m-1)) ;log average
                avemsdbw=avemsdbw+10^(msdiw(1,m-1)) ;linear average
                avesummsd=avesummsd+1
            endif
        endif
    endfor
endfor

```

```

    histxmsd(k-1)=(gridminmsd(k-1)+gridmaxmsd(k-1))/2
endfor
histymsdnorm=histymsd/total(histymsd) ;normalized
;print,i
if (weigh eq 0d) then begin
    aveall(1,i-1)=avemsd/avesummsd
    aveall(2,i-1)=alog10(avemsdb)/avesummsd
endif else begin
    aveall(1,i-1)=avemsdw/tlen;/avesummsd
    aveall(2,i-1)=alog10(avemsdbw)/tlen;/avesummsd
endelse

;<Slope>array
a=maxslp
b=minslp
bin=binslp
histxslp=((dindgen(bin*(a-b))+b*bin)/(bin)) ;histogram x data
histyslp=make_array(bin*(a-b))
aveslp=make_array(bin*(a-b))
avesumslp=make_array(bin*(a-b))
gridminslp=make_array(bin*(a-b))
gridmaxslp=make_array(bin*(a-b))
aveslp=0
aveslpb=0
aveslpw=0
aveslpbw=0
avesumslp=0
for k=1,bin*(a-b) do begin
    gridminslp(k-1)=(double(k)-1)/double(bin)+b
    gridmaxslp(k-1)=double(k)/double(bin)+b
    for m=1,counter do begin
        if (slpi(1,m-1) ge gridminslp(k-1)) AND (slpi(1,m-1) lt gridmaxslp(k-1)) then begin
            if (slpi(1,m-1) ne 0d) then begin
                histyslp(k-1)=histyslp(k-1)+slpi(0,m-1)
                aveslp =aveslp+ (slpi(1,m-1)) ;linear average
                aveslpb=aveslpb+10^(slpi(1,m-1)) ;log average
                aveslpw=aveslpw+ (slpiw(1,m-1)) ;linear average
                aveslpbw=aveslpbw+10^(slpiw(1,m-1)) ;log average
                avesumslp=avesumslp+1
            endif
        endif
    endfor
    histxslp(k-1)=(gridminslp(k-1)+gridmaxslp(k-1))/2
endfor
histyslpnorm=histyslp/total(histyslp) ;normalized
if (weigh eq 0d) then begin

```



```

    aveall(3,i-1)=aveslp/avesumslp
    aveall(4,i-1)=alog10(aveslpb)/avesumslp
endif else begin
    aveall(3,i-1)=aveslpw/tlen;/avesumslp
    aveall(4,i-1)=alog10(aveslpbw)/tlen;/avesumslp
endelse

;<G>array
a=maxgs
b=mings
bin=bing
histxgs=((dindgen(bin*(a-b))+b*bin)/(bin)) ;histogram x data
histygs=make_array(bin*(a-b))
avegs=make_array(bin*(a-b))
avesumgs=make_array(bin*(a-b))
gridmings=make_array(bin*(a-b))
gridmaxgs=make_array(bin*(a-b))
avegs=0
avegsb=0
avegs=0
avegsbw=0
avesumgs=0
for k=1,bin*(a-b) do begin
    gridmings(k-1)=(double(k)-1)/double(bin)+b
    gridmaxgs(k-1)=double(k)/double(bin)+b
    for m=1,counter do begin
        if (gsi(1,m-1) ge gridmings(k-1)) AND (gsi(1,m-1) lt gridmaxgs(k-1)) then begin
            if (gsi(1,m-1) ne 0d) then begin
                histygs(k-1)=histygs(k-1)+gsi(0,m-1)
                avegs =avegs+ (gsi(1,m-1)) ;linear average
                avegsb=avegsb+10^(gsi(1,m-1)) ;log average
                avegs=avegs+ (gsiw(1,m-1)) ;linear average
                avegsbw=avegsbw+10^(gsiw(1,m-1)) ;log average
                avesumgs=avesumgs+1
                ;print,avegs
            endif
        endif
    endfor
    histxgs(k-1)=(gridmings(k-1)+gridmaxgs(k-1))/2
endfor
histygsnorm=histygs/total(histygs) ;normalized
if (weigh eq 0d) then begin
    aveall(5,i-1)=avegs/avesumgs
    aveall(6,i-1)=alog10(avegsb)/avesumgs
endif else begin
    aveall(5,i-1)=avegs/tlen;/avesumgs

```

```

    aveall(6,i-1)=alog10(avegsbw)/tlen;/avesumgs
endelse
print,tlen
;<Gp>array
a=maxgp
b=mingp
bin=bingp
histxgp=((dindgen(bin*(a-b))+b*bin)/(bin)) ;histogram x data
histygp=make_array(bin*(a-b))
avegp=make_array(bin*(a-b))
avesumgp=make_array(bin*(a-b))
gridmingp=make_array(bin*(a-b))
gridmaxgp=make_array(bin*(a-b))
avegp=0
avegpb=0
avegpw=0
avegpbw=0
avesumgp=0
for k=1,bin*(a-b) do begin
    gridmingp(k-1)=(double(k)-1)/double(bin)+b
    gridmaxgp(k-1)=double(k)/double(bin)+b
    for m=1,counter do begin
        if (gpi(1,m-1) ge gridmingp(k-1)) AND (gpi(1,m-1) lt gridmaxgp(k-1)) then begin
            if (gpi(1,m-1) ne 0d) then begin
                histygp(k-1)=histygp(k-1)+gpi(0,m-1)
                avegp =avegp+ (gpi(1,m-1)) ;linear average
                avegpb=avegpb+10^(gpi(1,m-1)) ;log average
                avegpw =avegpw+ (gpiw(1,m-1)) ;linear average
                avegpbw=avegpbw+10^(gpiw(1,m-1)) ;log average
                avesumgp=avesumgp+1
                ;print,avegpw
            endif
        endif
    endfor
    histxgp(k-1)=(gridmingp(k-1)+gridmaxgp(k-1))/2
endfor
histygpnorm=histygp/total(histygp) ;normalized
if (weigh eq 0d) then begin
    aveall(7,i-1)=avegp/avesumgp
    aveall(8,i-1)=alog10(avegpb)/avesumgp
endif else begin
    aveall(7,i-1)=avegpw/tlen;/avesumgp
    aveall(8,i-1)=alog10(avegpbw)/tlen;/avesumgp
endelse
print,avegpw
;<Gpp>array

```

```

a=maxgpp
b=mingpp
bin=bingpp
histxgpp=((dindgen(bin*(a-b))+b*bin)/(bin)) ;histogram x data
histygpp=make_array(bin*(a-b))
avegpp=make_array(bin*(a-b))
avesumgpp=make_array(bin*(a-b))
gridmingpp=make_array(bin*(a-b))
gridmaxgpp=make_array(bin*(a-b))
avegpp=0
avegppb=0
avegppw=0
avegppbw=0
avesumgpp=0
for k=1,bin*(a-b) do begin
  gridmingpp(k-1)=(double(k)-1)/double(bin)+b
  gridmaxgpp(k-1)=double(k)/double(bin)+b
  for m=1,counter do begin
    if (gppi(1,m-1) ge gridmingpp(k-1)) AND (gppi(1,m-1) lt gridmaxgpp(k-1)) then
begin
      if (gppi(1,m-1) ne 0d) then begin
        histygpp(k-1)=histygpp(k-1)+gppi(0,m-1)
        avegpp =avegpp+ (gppi(1,m-1)) ;linear average
        avegppb=avegppb+10^(gppi(1,m-1)) ;log average
        avegppw =avegppw+ (gppi(1,m-1)) ;linear average
        avegppbw=avegppbw+10^(gppi(1,m-1)) ;log average
        avesumgpp=avesumgpp+1
      endif
    endif
  endfor
  histxgpp(k-1)=(gridmingpp(k-1)+gridmaxgpp(k-1))/2
endfor
histygppnorm=histygpp/total(histygpp) ;normalized
if (weigh eq 0d) then begin
  aveall(9,i-1)=avegpp/avesumgpp
  aveall(10,i-1)=alog10(avegppb)/avesumgpp
endif else begin
  aveall(9,i-1)=avegppw/tlen;/avesumgpp
  aveall(10,i-1)=alog10(avegppb)/tlen;/avesumgpp
endelse
  aveall(11,i-1)=counter2

;***Display***
device,decomposed=0
tek_color
;<MSD>

```

```

window,1,xsize=225,ysize=180,title='MSD distribution',xpos=350,ypos=214
plot,histxmsd,histymsd,psym=10,xtitle='Log(MSD)',ytitle='fraction [-]';
xrange=[0,1];yrange=[0,1]
ave=avemsd/avesummsd
;print,ave
avex=[ave,ave]
avey=[0,10]
oplot,avex,avey,psym=0,color=3,linestyle=0

;<SLOPE>
window,2,xsize=225,ysize=180,title='Slope distribution',xpos=350,ypos=428
plot,histxslp,histyslp,psym=10,xtitle='Slope',ytitle='fraction [-]';
xrange=[0,1];yrange=[0,1]
ave=aveslp/avesumslp
;print,ave
avex=[ave,ave]
avey=[0,10]
oplot,avex,avey,psym=10,color=3,linestyle=0

;<Gs>
window,3,xsize=225,ysize=180,title='G distribution',xpos=580,ypos=0
plot,histxgs,histygs,psym=10,xtitle='G [Pa]',ytitle='fraction [-]';
xrange=[0,1];yrange=[0,1]
ave=avegs/avesumgs
;print,ave
avex=[ave,ave]
avey=[0,10]
oplot,avex,avey,psym=10,color=3

;<Gp>
window,4,xsize=225,ysize=180,title='Gp distribution',xpos=580,ypos=214
plot,histxgp,histygp,psym=10,xtitle='Gp [Pa]',ytitle='fraction [-]';
xrange=[0,1];yrange=[0,1]
ave=avegp/avesumgp
;print,ave
avex=[ave,ave]
avey=[0,10]
oplot,avex,avey,psym=10,color=3

;<Gpp>
window,5,xsize=225,ysize=180,title='Gpp distribution',xpos=580,ypos=428
plot,histxgpp,histygpp,psym=10,xtitle='Gpp [Pa]',ytitle='fraction [-]';
xrange=[0,1];yrange=[0,1]
ave=avegpp/avesumgpp
;print,ave
avex=[ave,ave]

```

```

avey=[0,10]
oplot,avex,avey,psym=10,color=3
print,avesumgpp
,***Output***
arraymsd(0,*,0)=histxmsd ;Grid
arrayslp(0,*,0)=histxslp
arraygs (0,*,0)=histxgs
arraygp (0,*,0)=histxgp
arraygpp(0,*,0)=histxgpp
arraymsd(i,*,0)=histymsd ;MSD histogram
arrayslp(i,*,0)=histyslp
arraygs (i,*,0)=histygs
arraygp (i,*,0)=histygp
arraygpp(i,*,0)=histygpp

arraymsd(0,*,1)=histxmsd ;Grid
arrayslp(0,*,1)=histxslp
arraygs (0,*,1)=histxgs
arraygp (0,*,1)=histxgp
arraygpp(0,*,1)=histxgpp
arraymsd(i,*,1)=histymsdnorm ;Normalized Histogram
arrayslp(i,*,1)=histyslpnorm
arraygs (i,*,1)=histygsnorm
arraygp (i,*,1)=histygpnorm
arraygpp(i,*,1)=histygppnorm

aveall(0,*)=times-int*60/2

endfor

if (weigh eq 0d) then begin
write_gdf,arraymsd(*,*,0),filename+'_TransientMSDDist.gdf'
write_gdf,arraymsd(*,*,1),filename+'_TransientMSDDist_normalized.gdf'
write_gdf,arrayslp(*,*,0),filename+'_TransientSlopeDist.gdf'
write_gdf,arrayslp(*,*,1),filename+'_TransientSlopeDist_normalized.gdf'
write_gdf,arraygs (*,*,0),filename+'_TransientGsDist.gdf'
write_gdf,arraygs (*,*,1),filename+'_TransientGsDist_normalized.gdf'
write_gdf,arraygp (*,*,0),filename+'_TransientGpDist.gdf'
write_gdf,arraygp (*,*,1),filename+'_TransientGpDist_normalized.gdf'
write_gdf,arraygpp(*,*,0),filename+'_TransientGppDist.gdf'
write_gdf,arraygpp(*,*,1),filename+'_TransientGppDist_normalized.gdf'
write_gdf,aveall,filename+'_TransientMSDDist_AveQuantities.gdf'

write_text,arraymsd(*,*,0),filename+'_TransientMSDDist.txt'
write_text,arraymsd(*,*,1),filename+'_TransientMSDDist_normalized.txt'
write_text,arrayslp(*,*,0),filename+'_TransientSlopeDist.txt'

```

```

write_text,arrayslp(*,*,1),filename+'_TransientSlopeDist_normalized.txt'
write_text,arraygs(*,*,0),filename+'_TransientGsDist.txt'
write_text,arraygs(*,*,1),filename+'_TransientGsDist_normalized.txt'
write_text,arraygp(*,*,0),filename+'_TransientGpDist.txt'
write_text,arraygp(*,*,1),filename+'_TransientGpDist_normalized.txt'
write_text,arraygpp(*,*,0),filename+'_TransientGppDist.txt'
write_text,arraygpp(*,*,1),filename+'_TransientGppDist_normalized.txt'
write_text,aveall,filename+'_TransientMSDDist_AveQuantities.txt'
endif else begin
    weighrev=tlen
    print,tlen
    aveall(1:10,*)=aveall(1:10,*)

    write_gdf,arraymsd(*,*,0),filename+'_TransientMSDDist_weighted.gdf'
    write_gdf,arraymsd(*,*,1),filename+'_TransientMSDDist_weighted_normalized.gdf'
    write_gdf,arrayslp(*,*,0),filename+'_TransientSlopeDist_weighted.gdf'
    write_gdf,arrayslp(*,*,1),filename+'_TransientSlopeDist_weighted_normalized.gdf'
    write_gdf,arraygs(*,*,0),filename+'_TransientGsDist_weighted.gdf'
    write_gdf,arraygs(*,*,1),filename+'_TransientGsDist_weighted_normalized.gdf'
    write_gdf,arraygp(*,*,0),filename+'_TransientGpDist_weighted.gdf'
    write_gdf,arraygp(*,*,1),filename+'_TransientGpDist_weighted_normalized.gdf'
    write_gdf,arraygpp(*,*,0),filename+'_TransientGppDist_weighted.gdf'
    write_gdf,arraygpp(*,*,1),filename+'_TransientGppDist_weighted_normalized.gdf'
    write_gdf,aveall,filename+'_TransientMSDDist_weighted_AveQuantities.gdf'

    write_text,arraymsd(*,*,0),filename+'_TransientMSDDist_weighted.txt'
    write_text,arraymsd(*,*,1),filename+'_TransientMSDDist_weighted_normalized.txt'
    write_text,arrayslp(*,*,0),filename+'_TransientSlopeDist_weighted.txt'
    write_text,arrayslp(*,*,1),filename+'_TransientSlopeDist_weighted_normalized.txt'
    write_text,arraygs(*,*,0),filename+'_TransientGsDist_weighted.txt'
    write_text,arraygs(*,*,1),filename+'_TransientGsDist_weighted_normalized.txt'
    write_text,arraygp(*,*,0),filename+'_TransientGpDist_weighted.txt'
    write_text,arraygp(*,*,1),filename+'_TransientGpDist_weighted_normalized.txt'
    write_text,arraygpp(*,*,0),filename+'_TransientGppDist_weighted.txt'
    write_text,arraygpp(*,*,1),filename+'_TransientGppDist_weighted_normalized.txt'
    write_text,aveall,filename+'_TransientMSDDist_weighted_AveQuantities.txt'

endelse
close,1
end

```

REFERENCES

- [1] Larson, R.G., *The structure and rheology of complex fluids*. 1999, New York: Oxford University Press. xxi, 663 p.
- [2] Qiu, Y. and K. Park, Environment-sensitive hydrogels for drug delivery. *Advanced Drug Delivery Reviews*, 2001. **53**(3): p. 321-339.
- [3] Soppimath, K.S., T.M. Aminabhavi, A.M. Dave, S.G. Kumbar, and W.E. Rudzinski, Stimulus-responsive "smart" hydrogels as novel drug delivery systems. *Drug Development and Industrial Pharmacy*, 2002. **28**(8): p. 957-974.
- [4] Jeong, B. and A. Gutowska, Lessons from nature: stimuli-responsive polymers and their biomedical applications (vol 20, pg 305, 2002). *Trends in Biotechnology*, 2002. **20**(8): p. 360-360.
- [5] Gupta, P., K. Vermani, and S. Garg, Hydrogels: from controlled release to pH-responsive drug delivery. *Drug Discovery Today*, 2002. **7**(10): p. 569-579.
- [6] van der Linden, H.J., S. Herber, W. Olthuis, and P. Bergveld, Stimulus-sensitive hydrogels and their applications in chemical (micro)analysis. *Analyst*, 2003. **128**(4): p. 325-331.
- [7] Hoffman, A.S., *Intelligent Polymers in Medicine and Biotechnology*. *Macromolecular Symposia*, 1995. **98**: p. 645-664.
- [8] Rudzinski, W.E., A.M. Dave, U.H. Vaishnav, S.G. Kumbar, A.R. Kulkarni, and T.M. Aminabhavi, Hydrogels as controlled release devices in agriculture. *Designed Monomers and Polymers*, 2002. **5**(1): p. 39-65.
- [9] Peppas, N.A., P. Bures, W. Leobandung, and H. Ichikawa, Hydrogels in pharmaceutical formulations. *European Journal of Pharmaceutics and Biopharmaceutics*, 2000. **50**(1): p. 27-46.

- [10] Peppas, N.A., J.Z. Hilt, A. Khademhosseini, and R. Langer, Hydrogels in biology and medicine: From molecular principles to bionanotechnology. *Advanced Materials*, 2006. **18**(11): p. 1345-1360.
- [11] Beebe, D.J., J.S. Moore, J.M. Bauer, Q. Yu, R.H. Liu, C. Devadoss, and B.H. Jo, Functional hydrogel structures for autonomous flow control inside microfluidic channels. *Nature*, 2000. **404**(6778): p. 588-+.
- [12] Drury, J.L. and D.J. Mooney, Hydrogels for tissue engineering: scaffold design variables and applications. *Biomaterials*, 2003. **24**(24): p. 4337-4351.
- [13] Hoffman, A.S., Hydrogels for biomedical applications. *Advanced Drug Delivery Reviews*, 2002. **54**(1): p. 3-12.
- [14] Macosko, C.W., *Rheology: Principles, Measurements and Applications*. 1994, Poughkeepsie, NY Wiley-VCH.
- [15] Goeden-Wood, N.L., J.D. Keasling, and S.J. Muller, Self-assembly of a designed protein polymer into beta-sheet fibrils and responsive gels. *Macromolecules*, 2003. **36**(8): p. 2932-2938.
- [16] Brannonpeppas, L. and N.A. Peppas, Dynamic and Equilibrium Swelling Behavior of Ph-Sensitive Hydrogels Containing 2-Hydroxyethyl Methacrylate. *Biomaterials*, 1990. **11**(9): p. 635-644.
- [17] Kim, B., K. La Flamme, and N.A. Peppas, Dynamic swelling Behavior of pH-sensitive anionic hydrogels used for protein delivery. *Journal of Applied Polymer Science*, 2003. **89**(6): p. 1606-1613.
- [18] Hassan, C.M., F.J. Doyle, and N.A. Peppas, Dynamic behavior of glucose-responsive poly(methacrylic acid-g-ethylene glycol) hydrogels. *Macromolecules*, 1997. **30**(20): p. 6166-6173.

- [19] Siegel, R.A., I. Johannes, C.A. Hunt, and B.A. Firestone, Buffer Effects on Swelling Kinetics in Polybasic Gels. *Pharmaceutical Research*, 1992. **9**(1): p. 76-81.
- [20] Brannonpeppas, L. and N.A. Peppas, Time-Dependent Response of Ionic Polymer Networks to Ph and Ionic-Strength Changes. *International Journal of Pharmaceutics*, 1991. **70**(1-2): p. 53-57.
- [21] Chen, G.P., Y. Imanishi, and Y. Ito, Photolithographic synthesis of hydrogels. *Macromolecules*, 1998. **31**(13): p. 4379-4381.
- [22] Freyberg, M.A. and P. Friedl, The use of a conventional tissue culture plate as an optically accessible perfusion chamber for in situ assays and for long-term cultivation of mammalian cells. *Cytotechnology*, 1998. **26**(1): p. 49-58.
- [23] Waigh, T.A., Microrheology of complex fluids. *Reports on Progress in Physics*, 2005. **68**(3): p. 685-742.
- [24] Breedveld, V. and D.J. Pine, Microrheology as a tool for high-throughput screening. *Journal of Materials Science*, 2003. **38**(22): p. 4461-4470.
- [25] Mason, T.G., K. Ganesan, J.H. vanZanten, D. Wirtz, and S.C. Kuo, Particle tracking microrheology of complex fluids. *Physical Review Letters*, 1997. **79**(17): p. 3282-3285.
- [26] Mason, T.G. and D.A. Weitz, Optical Measurements of Frequency-Dependent Linear Viscoelastic Moduli of Complex Fluids. *Physical Review Letters*, 1995. **74**(7): p. 1250-1253.
- [27] Lu, Q. and M.J. Solomon, Probe size effects on the microrheology of associating polymer solutions. *Physical Review E*, 2002. **66**(6): p. -.
- [28] Bausch, A.R. and K. Kroy, A bottom-up approach to cell mechanics. *Nature Physics*, 2006. **2**(4): p. 231-238.

- [29] Crocker, J.C., M.T. Valentine, E.R. Weeks, T. Gisler, P.D. Kaplan, A.G. Yodh, and D.A. Weitz, Two-point microrheology of inhomogeneous soft materials. *Physical Review Letters*, 2000. **85**(4): p. 888-891.
- [30] Levine, A.J. and T.C. Lubensky, One- and two-particle microrheology. *Physical Review Letters*, 2000. **85**(8): p. 1774-1777.
- [31] Russel, W.B., D.A. Saville, and W.R. Schowalter, *Colloidal Dispersions*. Cambridge Monographs on Mechanics. 1992: Cambridge University Press.
- [32] Chae, B.S. and E.M. Furst, Probe surface chemistry dependence and local polymer network structure in F-actin microrheology. *Langmuir*, 2005. **21**(7): p. 3084-3089.
- [33] Chen, D.T., E.R. Weeks, J.C. Crocker, M.F. Islam, R. Verma, J. Gruber, A.J. Levine, T.C. Lubensky, and A.G. Yodh, Rheological microscopy: Local mechanical properties from microrheology. *Physical Review Letters*, 2003. **90**(10): p. -.
- [34] Harden, J.L. and V. Viasnoff, Recent advances in DWS-based micro-rheology. *Current Opinion in Colloid & Interface Science*, 2001. **6**(5-6): p. 438-445.
- [35] Romer, S., F. Scheffold, and P. Schurtenberger, Sol-gel transition of concentrated colloidal suspensions. *Physical Review Letters*, 2000. **85**(23): p. 4980-4983.
- [36] Wyss, H.M., S. Romer, F. Scheffold, P. Schurtenberger, and L.J. Gauckler, Diffusing-wave spectroscopy of concentrated alumina suspensions during gelation. *Journal of Colloid and Interface Science*, 2001. **241**(1): p. 89-97.
- [37] Tseng, Y., K.M. An, and D. Wirtz, Microheterogeneity controls the rate of gelation of actin filament networks. *Journal of Biological Chemistry*, 2002. **277**(20): p. 18143-18150.
- [38] Yamada, S., D. Wirtz, and S.C. Kuo, Mechanics of living cells measured by laser tracking microrheology. *Biophysical Journal*, 2000. **78**(4): p. 1736-1747.

- [39] McGrath, J.J., A Microscope Diffusion Chamber for the Determination of the Equilibrium and Non-Equilibrium Osmotic Response of Individual Cells. *Journal of Microscopy-Oxford*, 1985. **139**(Sep): p. 249-263.
- [40] Porsche, A.M., C. Korber, S. Englich, U. Hartmann, and G. Rau, Determination of the Permeability of Human-Lymphocytes with a Microscope Diffusion Chamber. *Cryobiology*, 1986. **23**(4): p. 302-316.
- [41] McGrath, J.J. and S. Krings, Computer-Controlled Concentration Histories in a Microscope Diffusion Chamber. *Cryobiology*, 1986. **23**(6): p. 546-546.
- [42] McGrath, J.J., Quantitative measurement of cell membrane transport: Technology and applications. *Cryobiology*, 1997. **34**(4): p. 315-334.
- [43] Hou, L., K. Lubyphelps, and F. Lanni, Brownian-Motion of Inert Tracer Macromolecules in Polymerized and Spontaneously Bundled Mixtures of Actin and Filamin. *Journal of Cell Biology*, 1990. **110**(5): p. 1645-1654.
- [44] Stone, H.A. and S. Kim, Microfluidics: Basic issues, applications, and challenges. *Aiche Journal*, 2001. **47**(6): p. 1250-1254.
- [45] Gondret, P., N. Rakotomalala, M. Rabaud, D. Salin, and P. Watzky, Viscous parallel flows in finite aspect ratio Hele-Shaw cell: Analytical and numerical results. *Physics of Fluids*, 1997. **9**(6): p. 1841-1843.
- [46] Patankar, S.V., *Numerical Heat Transfer And Fluid Flow*. 1980: Hemisphere Publishing Corporation.
- [47] Lide, D.R., *CRC Handbook of Chemistry and Physics*, ed. D.R. Lide. 2003, Boca Raton, Florida: CRC Press.
- [48] Hines, A.L. and R.N. Maddox, *Mass transfer : fundamentals and applications*. 1984, Englewood Cliffs, N.J.: Prentice-Hall. xiii, 542 p.

- [49] Deen, W.M., Hindered Transport of Large Molecules in Liquid-Filled Pores. *Aiche Journal*, 1987. **33**(9): p. 1409-1425.
- [50] Tanaka, H., M. Matsumura, and I.A. Veliky, Diffusion Characteristics of Substrates in Ca-Alginate Gel Beads. *Biotechnology and Bioengineering*, 1984. **26**(1): p. 53-58.
- [51] Keller, M., J. Schilling, and E. Sackmann, Oscillatory magnetic bead rheometer for complex fluid microrheometry. *Review of Scientific Instruments*, 2001. **72**(9): p. 3626-3634.
- [52] Crocker, J.C. and D.G. Grier, Methods of digital video microscopy for colloidal studies. *Journal of Colloid and Interface Science*, 1996. **179**(1): p. 298-310.
- [53] Mason, T.G., Estimating the viscoelastic moduli of complex fluids using the generalized Stokes-Einstein equation. *Rheologica Acta*, 2000. **39**(4): p. 371-378.
- [54] deBeer, D., P. Stoodley, and Z. Lewandowski, Measurement of local diffusion coefficients in biofilms by microinjection and confocal microscopy. *Biotechnology and Bioengineering*, 1997. **53**(2): p. 151-158.
- [55] Moaddeb, M. and W.J. Koros, Gas transport properties of thin polymeric membranes in the presence of silicon dioxide particles. *Journal of Membrane Science*, 1997. **125**(1): p. 143-163.
- [56] Hernandez, A., F. Martinez, A. Martin, and P. Pradanos, Porous Structure and Surface-Charge Density on the Walls of Microporous Alumina Membranes. *Journal of Colloid and Interface Science*, 1995. **173**(2): p. 284-296.
- [57] Hernandez, A., J.I. Calvo, P. Pradanos, L. Palacio, M.L. Rodriguez, and J.A. de Saja, Surface structure of microporous membranes by computerized SEM image analysis applied to Anopore filters. *Journal of Membrane Science*, 1997. **137**(1-2): p. 89-97.

- [58] Bowen, W.R., N. Hilal, R.W. Lovitt, and P.M. Williams, Atomic force microscope studies of membranes: Surface pore structures of Cyclopore and Anopore membranes. *Journal of Membrane Science*, 1996. **110**(2): p. 233-238.
- [59] Palacio, L., P. Pradanos, J.I. Calvo, and A. Hernandez, Porosity measurements by a gas penetration method and other techniques applied to membrane characterization. *Thin Solid Films*, 1999. **348**(1-2): p. 22-29.
- [60] Montermini, D., C.P. Winlove, and C.C. Michel, Effects of perfusion rate on permeability of frog and rat mesenteric microvessels to sodium fluorescein. *Journal of Physiology-London*, 2002. **543**(3): p. 959-975.
- [61] Wang, Z.Y., Q.Z. Zhang, M. Konno, and S. Saito, Sol-Gel Transition of Alginate Solution by Additions of Various Divalent-Cations - Critical-Behavior of Relative Viscosity. *Chemical Physics Letters*, 1991. **186**(4-5): p. 463-466.
- [62] Wang, Z.Y., Q.Z. Zhang, M. Konno, and S. Saito, Sol-Gel Transition of Alginate Solution by the Addition of Various Divalent-Cations - a Rheological Study. *Biopolymers*, 1994. **34**(6): p. 737-746.
- [63] Grant, G.T., E.R. Morris, D.A. Rees, P.J.C. Smith, and D. Thom, Biological Interactions Between Polysaccharides and Divalent Cations - Egg Box Model. *FEBS Letters*, 1973. **32**(1): p. 195-198.
- [64] Matsumoto, T. and K. Mashiko, Viscoelastic Properties of Alginate Aqueous-Solutions in the Presence of Salts. *Biopolymers*, 1990. **29**(14): p. 1707-1713.
- [65] Smidsrod, O. and G. Skjakbraek, Alginate as Immobilization Matrix for Cells. *Trends in Biotechnology*, 1990. **8**(3): p. 71-78.
- [66] Shirai, Y., K. Hashimoto, H. Yamaji, and M. Tokashiki, Continuous Production of Monoclonal-Antibody with Immobilized Hybridoma Cells in an Expanded Bed Fermenter. *Applied Microbiology and Biotechnology*, 1987. **26**(6): p. 495-499.

- [67] Winter, H.H. and F. Chambon, Analysis of Linear Viscoelasticity of a Cross-Linking Polymer at the Gel Point. *Journal of Rheology*, 1986. **30**(2): p. 367-382.
- [68] Boris, D.C. and R.H. Colby, Rheology of sulfonated polystyrene solutions. *Macromolecules*, 1998. **31**(17): p. 5746-5755.
- [69] Fuoss, R.M. and U.P. Strauss, Electrostatic Interaction of Polyelectrolytes and Simple Electrolytes. *Journal of Polymer Science*, 1948. **3**(4): p. 602-603.
- [70] Kim, A.J., V.N. Manoharan, and J.C. Crocker, Swelling-based method for preparing stable, functionalized polymer colloids. *Journal of the American Chemical Society*, 2005. **127**(6): p. 1592-1593.
- [71] Gisler, T. and D.A. Weitz, Tracer microrheology in complex fluids. *Current Opinion in Colloid & Interface Science*, 1998. **3**(6): p. 586-592.
- [72] MacKintosh, F.C. and C.F. Schmidt, Microrheology. *Current Opinion in Colloid & Interface Science*, 1999. **4**(4): p. 300-307.
- [73] Gittes, F., B. Schnurr, P.D. Olmsted, F.C. MacKintosh, and C.F. Schmidt, Microscopic viscoelasticity: Shear moduli of soft materials determined from thermal fluctuations. *Physical Review Letters*, 1997. **79**(17): p. 3286-3289.
- [74] Schnurr, B., F. Gittes, F.C. MacKintosh, and C.F. Schmidt, Determining microscopic viscoelasticity in flexible and semiflexible polymer networks from thermal fluctuations. *Macromolecules*, 1997. **30**(25): p. 7781-7792.
- [75] Liu, J., M.L. Gardel, K. Kroy, E. Frey, B.D. Hoffman, J.C. Crocker, A.R. Bausch, and D.A. Weitz, Microrheology probes length scale dependent rheology. *Physical Review Letters*, 2006. **96**(11): p. -.
- [76] Tharmann, R., M.M.A.E. Claessens, and A.R. Bausch, Micro- and macrorheological properties of actin networks effectively cross-linked by depletion forces. *Biophysical Journal*, 2006. **90**(7): p. 2622-2627.

- [77] Wong, I.Y., M.L. Gardel, D.R. Reichman, E.R. Weeks, M.T. Valentine, A.R. Bausch, and D.A. Weitz, Anomalous diffusion probes microstructure dynamics of entangled F-actin networks. *Physical Review Letters*, 2004. **92**(17): p. -.
- [78] Valentine, M.T., P.D. Kaplan, D. Thota, J.C. Crocker, T. Gisler, R.K. Prud'homme, M. Beck, and D.A. Weitz, Investigating the microenvironments of inhomogeneous soft materials with multiple particle tracking. *Physical Review E*, 2001. **64**06(6): p. -.
- [79] Gardel, M.L., M.T. Valentine, J.C. Crocker, A.R. Bausch, and D.A. Weitz, Microrheology of entangled F-actin solutions. *Physical Review Letters*, 2003. **91**(15): p. -.
- [80] Tseng, Y., T.P. Kole, S.H.J. Lee, and D. Wirtz, Local dynamics and viscoelastic properties of cell biological systems. *Current Opinion in Colloid & Interface Science*, 2002. **7**(3-4): p. 210-217.
- [81] Shin, J.H., M.L. Gardel, L. Mahadevan, P. Matsudaira, and D.A. Weitz, Relating microstructure to rheology of a bundled and cross-linked F-actin network in vitro. *Proceedings of the National Academy of Sciences of the United States of America*, 2004. **101**(26): p. 9636-9641.
- [82] Panorchan, P., D. Wirtz, and Y. Tseng, Structure-function relationship of biological gels revealed by multiple-particle tracking and differential interference contrast microscopy: The case of human lamin networks. *Physical Review E*, 2004. **70**(4): p. -.
- [83] Hasnain, I.A. and A.M. Donald, Microrheological characterization of anisotropic materials. *Physical Review E*, 2006. **73**(3): p. -.
- [84] Goodman, A., Y. Tseng, and D. Wirtz, Effect of length, topology, and concentration on the microviscosity and microheterogeneity of DNA solutions. *Journal of Molecular Biology*, 2002. **323**(2): p. 199-215.

- [85] Ma, L.L., S. Yamada, D. Wirtz, and P.A. Coulombe, A 'hot-spot' mutation alters the mechanical properties of keratin filament networks. *Nature Cell Biology*, 2001. **3**(5): p. 503-506.
- [86] Oppong, F.K., L. Rubatat, B.J. Frisken, A.E. Bailey, and J.R. de Bruyn, Microrheology and structure of a yield-stress polymer gel. *Physical Review E*, 2006. **73**(4): p. -.
- [87] Narita, T., A. Knaebel, J.P. Munch, and S.J. Candau, Microrheology of poly(vinyl alcohol) aqueous solutions and chemically cross-linked gels. *Macromolecules*, 2001. **34**(23): p. 8224-8231.
- [88] Dasgupta, B.R. and D.A. Weitz, Microrheology of cross-linked polyacrylamide networks. *Physical Review E*, 2005. **71**(2): p. -.
- [89] Tseng, Y., T.P. Kole, and D. Wirtz, Micromechanical mapping of live cells by multiple-particle-tracking microrheology. *Biophysical Journal*, 2002. **83**(6): p. 3162-3176.
- [90] Bursac, P., G. Lenormand, B. Fabry, M. Oliver, D.A. Weitz, V. Viasnoff, J.P. Butler, and J.J. Fredberg, Cytoskeletal remodelling and slow dynamics in the living cell. *Nature Materials*, 2005. **4**(7): p. 557-561.
- [91] Daniels, B.R., B.C. Masi, and D. Wirtz, Probing single-cell micromechanics in vivo: The microrheology of C-elegans developing embryos. *Biophysical Journal*, 2006. **90**(12): p. 4712-4719.
- [92] Dawson, M., D. Wirtz, and J. Hanes, Enhanced viscoelasticity of human cystic fibrotic sputum correlates with increasing microheterogeneity in particle transport. *Journal of Biological Chemistry*, 2003. **278**(50): p. 50393-50401.
- [93] Apgar, J., Y. Tseng, E. Fedorov, M.B. Herwig, S.C. Almo, and D. Wirtz, Multiple-particle tracking measurements of heterogeneities in solutions of actin filaments and actin bundles. *Biophysical Journal*, 2000. **79**(2): p. 1095-1106.

- [94] Tseng, Y. and D. Wirtz, Mechanics and multiple-particle tracking microheterogeneity of alpha-actinin-cross-linked actin filament networks. *Biophysical Journal*, 2001. **81**(3): p. 1643-1656.
- [95] Xu, J.Y., Y. Tseng, C.J. Carriere, and D. Wirtz, Microheterogeneity and microrheology of wheat gliadin suspensions studied by multiple-particle tracking. *Biomacromolecules*, 2002. **3**(1): p. 92-99.
- [96] Romer, S., C. Urban, H. Bissig, A. Stradner, F. Scheffold, and P. Schurtenberger, Dynamics of concentrated colloidal suspensions: diffusion, aggregation and gelation. *Philosophical Transactions of the Royal Society of London Series a-Mathematical Physical and Engineering Sciences*, 2001. **359**(1782): p. 977-984.
- [97] Heinemann, C., F. Cardinaux, F. Scheffold, P. Schurtenberger, F. Escher, and B. Conde-Petit, Tracer microrheology of gamma-dodecalactone induced gelation of aqueous starch dispersions. *Carbohydrate Polymers*, 2004. **55**(2): p. 155-161.
- [98] Sato, J. and V. Breedveld, Transient rheology of solvent-responsive complex fluids by integrating microrheology and microfluidics. *Journal of Rheology*, 2006. **50**(1): p. 1-19.
- [99] Dasgupta, B.R., S.Y. Tee, J.C. Crocker, B.J. Frisken, and D.A. Weitz, Microrheology of polyethylene oxide using diffusing wave spectroscopy and single scattering. *Physical Review E*, 2002. **65**(5): p. -.
- [100] Nowak, A.P., V. Breedveld, L. Pakstis, B. Ozbas, D.J. Pine, D. Pochan, and T.J. Deming, Rapidly recovering hydrogel scaffolds from self-assembling diblock copolypeptide amphiphiles. *Nature*, 2002. **417**(6887): p. 424-428.
- [101] Weeks, E.R., J.C. Crocker, A.C. Levitt, A. Schofield, and D.A. Weitz, Three-dimensional direct imaging of structural relaxation near the colloidal glass transition. *Science*, 2000. **287**(5453): p. 627-631.

- [102] Kegel, W.K. and A. van Blaaderen, Direct observation of dynamical heterogeneities in colloidal hard-sphere suspensions. *Science*, 2000. **287**(5451): p. 290-293.
- [103] Deming, T.J., Polypeptide hydrogels via a unique assembly mechanism. *Soft Matter*, 2005. **1**(1): p. 28-35.
- [104] Deming, T.J., Facile synthesis of block copolypeptides of defined architecture. *Nature*, 1997. **390**(6658): p. 386-389.
- [105] Pakstis, L.M., B. Ozbas, K.D. Hales, A.P. Nowak, T.J. Deming, and D. Pochan, Effect of chemistry and morphology on the biofunctionality of self-assembling diblock copolypeptide hydrogels. *Biomacromolecules*, 2004. **5**(2): p. 312-318.
- [106] Breedveld, V., A.P. Nowak, J. Sato, T.J. Deming, and D.J. Pine, Rheology of block copolypeptide solutions: Hydrogels with tunable properties. *Macromolecules*, 2004. **37**(10): p. 3943-3953.
- [107] Pochan, D.J., L. Pakstis, B. Ozbas, A.P. Nowak, and T.J. Deming, SANS and Cryo-TEM study of self-assembled diblock copolypeptide hydrogels with rich nano- through microscale morphology. *Macromolecules*, 2002. **35**(14): p. 5358-5360.
- [108] Nowak, A.P., J. Sato, V. Breedveld, and T.J. Deming, Hydrogel Formation in Amphiphilic Triblock Copolypeptides. *Supramolecular Chemistry*, 2006.
- [109] Nowak, A.P., V. Breedveld, D.J. Pine, and T.J. Deming, Unusual salt stability in highly charged diblock co-polypeptide hydrogels. *Journal of the American Chemical Society*, 2003. **125**(50): p. 15666-15670.
- [110] Schneider, J.P., D.J. Pochan, B. Ozbas, K. Rajagopal, L. Pakstis, and J. Kretsinger, Responsive hydrogels from the intramolecular folding and self-assembly of a designed peptide. *Journal of the American Chemical Society*, 2002. **124**(50): p. 15030-15037.

- [111] Sato, J. and V. Breedveld, unpublished results.
- [112] Baumberger, T., C. Caroli, and D. Martina, Solvent control of crack dynamics in a reversible hydrogel. *Nature Materials*, 2006. **5**(7): p. 552–555.
- [113] Lin, T.H. and G.D.J. Phillies, Probe Diffusion in Poly(Acrylic Acid) Water - Effect of Probe Size. *Macromolecules*, 1984. **17**(9): p. 1686-1691.
- [114] Tuteja, A., M.E. Mackay, C.J. Hawker, and B. Van Horn, Effect of ideal, organic nanoparticles on the flow properties of linear polymers: Non-Einstein-like behavior. *Macromolecules*, 2005. **38**(19): p. 8000-8011.
- [115] Levine, A.J. and T.C. Lubensky, Response function of a sphere in a viscoelastic two-fluid medium. *Physical Review E*, 2001. **63**04(4): p. -.
- [116] Morse, D.C., Viscoelasticity of concentrated isotropic solutions of semiflexible polymers. 2. Linear response. *Macromolecules*, 1998. **31**(20): p. 7044-7067.
- [117] Langer, R. and N.A. Peppas, Advances in biomaterials, drug delivery, and bionanotechnology. *Aiche Journal*, 2003. **49**(12): p. 2990-3006.
- [118] Lim, F. and A.M. Sun, Microencapsulated Islets as Bioartificial Endocrine Pancreas. *Science*, 1980. **210**(4472): p. 908-910.
- [119] Skjakbraek, G., O. Smidsrod, and B. Larsen, Tailoring of Alginates by Enzymatic Modification In vitro. *International Journal of Biological Macromolecules*, 1986. **8**(6): p. 330-336.
- [120] Skjakbraek, G., H. Grasdalen, and O. Smidsrod, Inhomogeneous Polysaccharide Ionic Gels. *Carbohydrate Polymers*, 1989. **10**(1): p. 31-54.
- [121] Chrastil, J., Gelation of Calcium Alginate - Influence of Rice Starch or Rice Flour on the Gelation Kinetics and on the Final Gel Structure. *Journal of Agricultural and Food Chemistry*, 1991. **39**(5): p. 874-876.

- [122] Blandino, A., M. Macias, and D. Cantero, Formation of calcium alginate gel capsules: Influence of sodium alginate and CaCl₂ concentration on gelation kinetics. *Journal of Bioscience and Bioengineering*, 1999. **88**(6): p. 686-689.
- [123] Khairou, K.S., W.M. Al-Gethami, and R.M. Hassan, Kinetics and mechanism of sol-gel transformation between sodium alginate polyelectrolyte and some heavy divalent metal ions with formation of capillary structure polymembranes ionotropic gels. *Journal of Membrane Science*, 2002. **209**(2): p. 445-456.
- [124] Thu, B., P. Bruheim, T. Espevik, O. Smidsrod, P. SoonShiong, and G. SkjakBraek, Alginate polycation microcapsules .2. Some functional properties. *Biomaterials*, 1996. **17**(11): p. 1069-1079.
- [125] Mansky, P. and D.A. Hajduk, High throughput rheological testing of materials 2003.Symyx Technologies, INC 20030037601
- [126] Carlson, E.D., D.A. Hajduk, L. Matsiev, A. Safir, and P. Mansky, High throughput preparation and analysis of materials 2005.Symyx Technologies, Inc. U.S. Patent 6,881,363
- [127] Hajduk, D. and P. Mansky, High throughput viscometer and method of using same 2002.Symyx Technologies, Inc. U.S. Patent 6,393,898
- [128] Mansky, P. and D.A. Hajduk, High throughput rheological testing of materials 2004.Symyx Technologies, INC U.S. Patent 6,769,292
- [129] Mansky, P. and D.A. Hajduk, High throughput rheological testing of materials 2006.Symyx Technologies, INC 7,051,581
- [130] Mansky, P. and D.A. Hajduk, High throughput rheological testing of materials 2004.Symyx Technologies, INC 20040123650
- [131] Kolosov, O. and L. Matsiev, High throughput rheological testing of materials 2004.Symyx Technologies, Inc. 20040123650

- [132] Mansky, P. and D.A. Hajduk, High throughput rheological testing of materials 2004.Symyx Technologies, INC 20040265914
- [133] Carlson, E.D., D.A. Hajduk, L. Matsiev, A. Safir, and P. Mansky, High throughput preparation and analysis of materials, 2003.Symyx Technologies, Inc. 20030127776
- [134] Hajduk, D. and P. Mansky, High throughput viscometer and method of using game 2004.Symyx Technologies, Inc. 20040211247
- [135] Carlson, E.D. and O. Kolosov, High throughput testing of fluid samples using an electric field 2003.Symyx Technologies, Inc. 20030203500

LIST OF PUBLICATIONS

PEER REVIEWED JOURNAL

Breedveld, V., Nowak, A.P., **Sato, J.**, Deming, T.J. and Pine, D.J. "Rheology of block copolypeptide solutions: hydrogels with tunable properties", *Macromolecules* , **37** (10), 3943-3953 (2004).

Sato, J. and Breedveld, V. "Evaporation Blocker for Cone-Plate Rheometry of Volatile Samples", *Applied Rheology*, **15** (6) 390-397 (2005).

Sato, J. and Breedveld, V. "Transient Rheology of Solvent-Responsive Complex Fluids by Integrating Microrheology and Microfluidics", *Journal of Rheology*, **50** (1), 1-19 (2006), selected for *Virtual Journal of Nanoscale Science & Technology*, **13**(2) (2006).

Nowak, A.P., **Sato, J.**, Breedveld, V., Deming, T.J. "Hydrogel Formation in Amphiphilic Triblock Copolypeptides", *Supramolecular Chemistry*, **18**(5), 423-427 (2006).

Sato, J., Nowak, A.P., Deming, T.J. and Breedveld, V. "Microstructural evolution of self-assembled stimuli-responsive hydrogels", *submitted for publication* (2006).

Sato, J. and Breedveld, V. "Transient particle tracking microrheology of heterogeneous samples", *submitted for publication* (2006).

Sato, J., Nowak, A.P., Deming, T.J. and Breedveld, V. " Morphological and rheological changes of heterogeneous salt responsive block copolypeptide hydrogels", *submitted for publication* (2006).

CONFERENCE PROCEEDINGS

Sato, J. and Breedveld V. "Integrating Microrheology and Microfluidics: Transient Rheology of Salt-responsive Hydrogels" *Proceedings of the 14th International Congress of Rheology* (2004)

Sato, J. and Breedveld, V. "A New Accessory for Cone-Plate Rheometry of High Vapor Pressure Solvent Samples" *Proceedings of the 33rd Annual Conference of the North American Thermal Analysis Society (NATAS)* (2005)

PATENT

Breedveld V. and **Sato, J.** "Device for High-Throughput Characterization of Solvent-Responsive Materials by using Dialysis Diffusion Cell", GTRC proprietary ID#3676 (2005), patent pending

VITA

JUN SATO

Jun Sato was born on November 11, 1973 in Tokyo, Japan. He attended Nishi cosmopolitan high school in Tokyo, Japan. He received his Bachelor of Engineering in Chemical Engineering from the Tokyo Institute of Technology in 1998 and obtained his Masters of Engineering in Chemical Engineering from the same institute in 2001. His Masters thesis research focused on elucidating a relationship between blood flow patterns at a branching blood vessel and the occurrence of pathological diseases and was performed under the guidance of Professor Kohei Ogawa. During his Masters program, he stayed in the Chemical Engineering Department at the University of Wisconsin, Madison, for one year from 1999 to 2000, with a scholarship awarded by the Japanese Ministry of Education, Culture and Science. He performed research on axial dispersion in Taylor-Couette flow under the supervision of Professor Michael D. Graham and Professor Edwin N. Lighfoot. After receiving his Masters of Engineering, he worked for Nikkiso Co., Tokyo, Japan for one year and joined the School of Chemical & Biomolecular Engineering at the Georgia Institute of Technology in 2002 as a Ph.D. student. At Georgia Tech, he worked in the area of microrheology of environmentally responsive hydrogels under the supervision of Professor Victor Breedveld. After graduating with a Ph.D in Chemical Engineering in September 2006, he will work for Symyx Technologies Inc., Santa Clara, CA as a staff scientist.